Optimising Implant Pegs for Primary Fixation

A Finite Element Approach

Submitted in partial fulfilment of the requirements for the degree

Doctor of Philosophy in Musculoskeletal Sciences

David Heath MEng, AMIMechE

St John's College

University of Oxford

Supervisors

Professor David W. Murray and Professor Stephen Mellon

Nuffield Department of Orthopaedics, Rheumatology, and Musculoskeletal Sciences

University of Oxford

Hilary Term 2025

Abstract

Optimising Implant Pegs for Primary Fixation

A Finite Element Approach

David Heath, St John's College **DPhil, Hilary Term 2025**

Cementless orthopaedic implants are commonly held in place in the surrounding bone by an interference fit between fixation geometry and the bone. This fixation geometry often takes the form of a peg. The over-arching aim of this thesis was to use a finite element approach to improve the primary fixation of an orthopaedic peg which would be applied to a Unicompartmental Knee Replacement (UKR) tibial component. The achievement of this aim was broken into three objectives: To generate an optimised finite element model for the prediction of pull-out force of a peg, which is related to primary fixation; To use the model to design an optimal peg for primary fixation; To develop a knee simulator that could be used to assess the primary fixation of implants using various peg designs under physiological loading, through the measurement of micromotion.

A series of material models were compared to determine the most accurate for predicting the pull-out force of a 5.65mm diameter round nose peg in PCF 20 polyurethane foam bone analogue, in the clinically relevant interference range of 0.6mm – 1.2mm. It was found that the most accurate of these were plastic hardening models, specifically the Drucker-Prager and Von-Mises models, with all plastic hardening models tested falling under a ±15% error bound in the interference range 0.6mm – 1.2mm. A further study showed that the Drucker-Prager model, with the addition of accurate material data and element deletion, benefited most from a uniform structured mesh thereby reducing the simulation error by 7.4%. The final error in the interference range 0.6mm – 1.2mm was 5.40% ± 3.15% 95% CI. It was also shown that this model was generalisable to foams of lower densities (PCF 12, 15). With accurate material data, the maximum error of 16.07% ± 2.75% 95% CI was for PCF 12, and the minimum error of 4.10% ± 2.29% 95% CI was for PCF 15.

The developed FEA model was then used to design an optimal peg for primary fixation. This was done by initially considering the pressure distribution on the surface of the peg, which was shown to be highest at midpoint of the peg length for pull-out. A series of nose cone forms were evaluated using the FEA model, with an LV Haack nose form being selected due to its relatively mild response to changing fineness ratio. From experimental validation a 3mm nose length (fineness ratio 1.875) was selected as the optimal nose form for primary fixation. This resulted in an average of ~30% increase in pull-out force in the clinically relevant range compared to a conventional round nose peg, and an average of ~40% increased pull-out force over the whole interference range 0.4mm – 1.6mm. At a lower interference the same primary fixation could be achieved with an estimated ~61% reduction in stress from insertion forces and estimated ~157% factor of safety increase over the current design. The benefit over a round nose peg was an estimated ~18% stress reduction and estimated ~22% factor of safety increase with the new 3mm LV Haack peg.

As this new peg would require evaluation under physiological loading for primary fixation in terms of micromotion, a novel UKR simulator was developed and characterised in relation to a displacement profile input as a first step in addressing this need. The root mean square error (RMS) was calculated between the demand and measured displacement. The machine was shown to have a base (RMS) error under constant vertical load (5N) of 0.48mm ± $4.49*10^{-3}$mm 95% CI in the anterior posterior axis and 5.91deg ± 0.29deg 95% CI in the flexion axis. The error was also characterised under altering vertical loading and lubrication conditions. Lubrication was found to be necessary to run the machine at loads greater than 600N. With further development, the machine is hoped to be used to evaluate primary fixation of novel peg designs under dynamic physiologically relevant loading.

This thesis has achieved each objective that it set out to achieve. Specifically, a finite element model has been developed and optimised. That model was used to design a novel peg, a 3mm LV Haack design which sufficiently improved pull-out force production, by ~30%, compared to a conventional round nose peg at the same interference. Finally, a knee wear simulator was developed and recommendations were made to allow it to be developed to be capable of measuring micromotion.

Future work is needed to validate the peg for clinical applicability. Moreover, the wear simulator should be developed further to allow micromotion studies. It is hoped that the contributions of this thesis will lead to better clinical outcomes for patients.

To my God and Saviour:

For all his constant guidance, and everlasting love.

Without His grace and gifts I would not have had the strength to complete this research.

May it, in some small way, bring Him glory.

Acknowledgements

It is said that no man is an island and this research has been no different. So, I would like to mention a few people who have specifically shaped me on my academic journey. Firstly I would like to thank my doctoral supervisors, Professor David Murray and Professor Stephen Mellon, who both gave me the opportunity to pursue this degree and supported, encouraged, and stretched me to new heights over its course. As well as Mr. Laurence Marks for being an invaluable source of knowledge and a sounding board for all things finite element analysis.

Mrs. Barbara Marks and Mrs. Jo Brown for their tireless work in supporting the research of the Oxford Orthopaedic Engineering Centre (OOEC), and to Mrs. Barbara Marks particularly, for all of her encouragement and support during this journey.

My college supervisor Professor Zoltán Molnár and Dr. Matthew Nicholls were both immensely supportive on the college front, helping me to resolve various issues during my time there. In particular, I would also like to thank Associate Professor Shpend Gerguri for all of his care, advice, and wisdom during my many years of knowing and working with him.

To my colleagues and collaborators at The University of Oxford and Oxford Brookes University, who went out of their way to support my research, specifically: Professor Allan Hutchinson, Professor James Broughton, Associate Professor Olga Barrera, Associate Professor Neil Fellows, Associate Professor Daniel Bell, and Dr. Igor Dyson. I would also like to specifically thank Dr. Karthik Krishna Kumar and Dr. Colin Bell, who both did so much to ignite and encourage my passion for research, ultimately inspiring me to embark on this journey.

I would also like to extend a special thanks to the members of The University of Oxford, Department of Oncology workshop and the members of the Oxford Brookes University workshop, specifically: Mr. Ian Spacksman, Mr. Douglas Daniel, Mr. Andrew Slatter, and Mr. Geoffrey Tombs. Who, through patience and wisdom, have guided me to be both a better designer and engineer. Ultimately, without their exceptional skill, experience, and craftsmanship to reify them, there are many designs, airborne and otherwise, which would have remained on paper.

My colleagues and friends in OOEC, who have inspired, driven, and encouraged me, and with whom it has been an absolute privilege to work over the last four amazing years: Dr. Jack Tu, Dr. Thomas Hamilton, Dr. Azmi Rahman, Dr Xiaoyi Min, Dr. Lauchlan Arthur, Dr. Nisrina Widari, and Dr. Alexander MacAulay.

My friends, companions, and partners in crime at St. Johns College, who each added unique and vibrant texture to each new day. College life simply would not have been the same without them: Dr. Rolf Morel, Mrs. Lei Wang, Mr. Stanislas Lalanne, Mr. Paweł Rzemieniecki, Mr. Adrian Martini, Miss Ana Stoienescu, Mr. Matthew Ford, and Mr. Reinier van Straten.

Further, Mr. Jared Miller who has long been a good friend and has always encouraged me to push harder, faster, and higher. Two friends deserve a special mention, Mr. Richard Thwaites and Miss Melanie Goss for being solid, true, and dear friends though may years and trials, as well as a source of inspiration and strength.

Finally, my parents: The Reverend J.P. and Mrs. Angela Heath, deserve the greatest thanks. Both of whom have given me an unshakable foundation to build on and endowed me with a strong belief in education, self betterment, and resilience that has carried me through many hurdles. They have tirelessly supported and encouraged me all the way along this long journey. I would not be the academic, engineer, or man I am without them.

Covid-19 Statement

The first year of this work, from Michaelmas Term 2020 to the start of Michaelmas Term 2021, was undertaken remotely, under the lockdown conditions that were implemented in the United Kingdom of Great Britain and Northern Ireland during this time period, due to the Covid-19 pandemic.

Abbreviations and symbols

These have been split into sections based on topic.

Organizations

ASTM.....American Society for Testing and Materials

BS ISO.....British Standards and International Standards Organisation

OOEC.....Oxford Orthopaedic Engineering Centre

UKAS.....United Kingdom Accreditation Service

Knee replacements

OUKR.....Oxford unicompartmental knee replacement

TKR.....Total knee replacement

UKR.....Unicompartmental knee replacement

Units of measurement

GPa.....Gigapascals

Hz.....Hertz

kN.....Kilonewtons of force

MPa.....Megapascals

N.....Newtons of force

NR.....Nose

PCF.....Pounds per cubic foot

Statistical measurements

ANOVA.....Analysis of variance

CI.....Confidence interval (usually 95% confidence interval)

RMS.....Root mean square

Materials

PU.....Polyurethane

UHMWPE.....Ultra-high molecular weight polyethylene

Mechanical engineering terms

AOD.....Angle of dilation

AOF.....Angle of friction

ARC.....Aspect ratio compensation

CAD.....Computer aided design

CAM.....Computer aided manufacture

CPU.....Central processing unit

DIC.....Digital image correlation

DP.....Drucker-Prager material model

DV Haack.....Diameter to volume Haack

ED.....Element deletion

FE.....Fracture energy (in the context of material parameters)

FEA.....Finite element analysis

FR.....Fineness ratio (Length to diameter ratio of a nose cone)

FSR.....Flow stress ratio

GPU.....Graphical processing unit

LD Haack.....Length to diameter Haack

LV Haack.....Length to volume Haack

UCS.....Ultimate compressive stress

VM.....Von-Mises material model

VUMAT.....Abaqus user material interface

Biomedical terms

ADL.....Activities of daily living

AP.....Anterior-posterior (in the context of joint motion)

FE.....Flexion-extension (in the context of joint motion)

IE.....Internal-external rotation (in the context of joint motion)

LVDT.....Linear variable differential transformer

RSA.....Radiosterometric analysis

Peg and foam geometrical names

A.....Foam hole radius

B.....Bulk foam around hole radius

C.....Total foam depth

D.....Foam hole depth

L.....Length of peg

NR.....Nose radius

PR.....Peg radius

Mathematical symbols

ρ_r ..... Density ratio of a foam

y ..... Distance from the neutral axis of a shape to the analysis depth

E_{yr} ..... Elastic yield ratio of a foam

PO_e ..... Experimental pull-out force in newtons

ϕ ..... Fraction of solid in the cell edge

E_{s2} ..... Material parameter related to the relaxed solid modulus

C_4 ..... Material specific coefficient of a foam, used in elastic yield ratio

C_1 ..... Material specific coefficient of a foam, used in modulus ratio

C_5 ..... Material specific coefficient of a foam, used in plastic yield ratio

L ..... Maximum length of the nose cone

R ..... Maximum radius of the nose cone

ME ..... Mesh error in percentage

E_s ..... Modulus of the solid the foam is made from

M_r ..... Modulus ratio of a foam

M ..... Moment

P_{yr} ..... Plastic yield ratio of a foam

X ..... Point along the nose cone length used in calculation of radius

r ..... Radius at current point along the length of the nose cone

I ..... Second moment of area of a shape

φ ..... Shape parameter of the Haack nose cone

SR ..... Simulated pull-out force error in percentage

PO_s ..... Simulated pull-out force in newtons

PO_{cm} ..... Simulated pull-out force in newtons for current mesh

PO_{nm} ..... Simulated pull-out force in newtons for next mesh

E_{s1} ..... Solid modulus pre-relaxation

ε ..... Strain

σ ..... Stress

τ ..... Time of relaxation

η_s ..... Viscosity of the solid

σ_{ys} ..... Yield stress of the cell wall of a foam

Table of Contents

Table of Figures

Index of Tables

Chapter 1 Introduction and thesis objectives

1.1 What is primary fixation

This thesis is concerned with primary fixation of a knee replacement. Therefore as a very brief introduction, it will be useful for the reader to understand what the author is indicating when he refers to primary fixation. Primary fixation of a joint replacement is the state that is concerned with the immediate retention of that joint replacement in its designated environment, the bone around the joint, immediately postoperatively and for a short period thereafter, until the replacement joint is secure in the bone and the long term fixation state has become dominant. This changeover usually starts at 6 – 8 weeks postoperatively (Parithimarkalaignan and Padmanabhan, 2013; Kohli *et al.*, 2018; Kohli, Stoddart and Van Arkel, 2021). After this period, the dominant fixation of the implant transitions to secondary fixation, which involves bony ingrowth into the implant and restructuring of the bone around the new loading conditions. This thesis will briefly look at secondary fixation and then only in so far as it is facilitated by primary fixation.

Primary fixation is concerned with effects such as the force that is required to dislodge the implant from the environment, the friction or adhesion that is used to resist that joint removal, and the motion of the implant relative to the bone under loading (micromotion). This section will introduce several of these concepts in more detail as well as some of the considerations that are required to achieve them.

1.2 Overview

Osteoarthritis is currently a prevalent disease of the joints which degrades function, of which the commonest sub-category is knee osteoarthritis (FELSON, 1988; UK and London, 2014; Stoddart *et al.*, 2021). A common treatment for severe osteoarthritis is joint replacement, and total knee replacements (TKR) are predicted to increase in the coming decades (Kurtz *et al.*, 2007; Shichman *et al.*, 2023; Reed *et al.*, 2024). In 2023, 116,845 primary knee replacements were carried out, 98% of which were performed due to osteoarthritis (Reed *et al.*, 2024), and the number of revisions alone is predicted to increase to 268,200 (±94,350 95% CI) per year by 2030 (Kurtz *et al.*, 2007). An alternative form of knee replacement is the unicompartmental knee replacement (UKR), ~ 10% of the 1,666,235 primary knee replacements in the National Joint Registry (NJR) of the United Kingdom, while TKRs make up ~86% of the same registry (Reed *et al.*, 2024). UKRs are in two main variants: the slightly more common mobile variant (~6% of the NJR database) and slightly less common fixed bearing variant (~4% of the NJR database), which are designated based on whether the bearing is able to move in relation to the metallic tibial component (Reed *et al.*, 2024). There is a third variant, the monobloc polyethylene tibia but this is rarely used (~0.4% of NJR database) (Reed *et al.*, 2024).

TKR may dominate in prevalence as they may be seen as a “safer option” than UKR by surgeons as they perform well in patients and UKR’s result in higher revision rates than the NJR average for knees (Reed *et al.*, 2024). Specifically, UKR’s have ~1.9 times higher revision rates at 5 years (4.59% to 2.40%) and ~2.5 times higher at 15 years (13.83% to 5.49%) when calculated from all UKR primary revision data and compared to the NJR average for all knee revisions (Reed *et al.*, 2024), showing that not only is the revision rate of UKR higher than average but the revision rate of UKRs increases at longer joint lifespans.

However, this rate is improved from historical data which showed a 2.4 times higher revision rate for UKR at an earlier 8 years (Liddle *et al.*, 2014; Goodfellow *et al.*, 2015), compared to a similar ~2.5 times higher at 15 years from the latest data NJR report (Reed *et al.*, 2024). It is therefore clear that the revision rate of UKR is improving, though is still substantially higher than that of TKR.

Revision rate has been critiqued as a sole outcome measure for not capturing the function of the joint at revision in favour of a measure that recognises joint function at the time of revision, specifically the Oxford knee score (OKS). Goodfellow *et al.* (2010) uses data from the New Zealand National Joint Registry 10 year report (Rothwell *et al.*, 2009) to explore the use the OKS as a measure. He showed that patients who had an OKS score of less or equal to 20 after a UKR, suggesting a worse score postoperatively than preoperatively, had a revision rate ~5 times greater than the TKR revision rate for patients who had the same OKS. This suggested that the threshold for revision in UKR may be lower than that of TKR which, in turn, may be due to revisions of UKR being easier than those of TKR. This is particularly true as UKR can generally be revised to a primary TKR with better outcomes expected than those of revised TKRs (Rothwell *et al.*, 2009; Goodfellow, O'Connor and Murray, 2010; Goodfellow *et al.*, 2015). Furthermore, the functional outcomes of UKR are often better than those of TKR, as UKR's demonstrate improved joint kinematics due in part to the preservation of the soft tissue around the joint (Laurencin *et al.*, 1991; Rougraff, Heck and Gibson, 1991; Price *et al.*, 2004; Zavatsky, Oppold and Price, 2004; Pandit *et al.*, 2008; Goodfellow *et al.*, 2015; Ma *et al.*, 2015; Pegg *et al.*, 2015).

This benefit is particularly true in the case of mobile-bearing UKRs, though again at potentially higher revision rates due to wear than fixed bearing joints (Reed *et al.*, 2024 Table 3.K10). Moreover, UKRs have lower morbidity, mortality, and faster recovery times than TKRs particularly with a minimally invasive procedure (Pandit *et al.*, 2011; Liddle *et al.*, 2014; Goodfellow *et al.*, 2015).

1.3 Unicompartmental knee replacement risks

While the benefits of UKR's over TKR's are clear, the very high rates of revision should not be ignored and indeed should be a specific area of focus for improvement. From the latest NJR data (Reed *et al.*, 2024 Table 3.K10), the main causes of revision surgery for cemented UKRs are shown in order of prevalence in Table 1.1. The revision rates are shown in number of revisions per 1000 prosthesis years and the proportion of mobile bearings in each set of data is: cemented 41.45% (50778 / 122516) and cementless 97.02% (41876 / 43162). Each is ranked for its commonness in both cemented and cementless UKR's, aside from all reasons (the total of all revisions) and other indication categories (all other reasons for revision that were not explicitly listed in the NJR report).

Table 1.1: Registry data on reasons for revision of cementless and cemented UKR taken from (Reed et al., 2024 Table 3.K10). The rates are shown in revisions in no. revisions per 1000 prosthesis-years.

Reason for revision	Cemented (Lower - Upper 95% CI Range)	Cemented revision rank	Cementless (Lower - Upper 95% CI Range)	Cementless revision rank
All reasons	10.22 (10.01-10.43)	-	7.52 (7.16-7.90)	-
Progressive arthritis	3.52 (3.38-3.66)	1	2.45 (2.25-2.67)	1
Aseptic loosening / lysis	2.82 (2.72-2.94)	2	0.88 (0.76-1.02)	4
Pain	1.65 (1.57-1.74)	3	0.61 (0.51-0.72)	6
Implant wear	1.12 (1.05-1.19)	4	0.94 (0.82-1.08)	3
Instability	0.82 (0.77-0.88)	5	0.67 (0.57-0.79)	5

Reason for revision	Cemented (Lower - Upper 95% CI Range)	Cemented revision rank	Cementless (Lower - Upper 95% CI Range)	Cementless revision rank
Dislocation / Subluxation	0.50 (0.46-0.55)	6	1.23 (1.09-1.39)	2
Malalignment	0.48 (0.43-0.52)	7	0.31 (0.25-0.40)	9
Infection	0.42 (0.38-0.46)	8	0.48 (0.39-0.58)	8
Periprosthetic fracture	0.19 (0.17-0.22)	9	0.54 (0.45-0.64)	7
Other indication	1.23 (1.16-1.30)	-	0.93 (0.81-1.07)	-

Table 1.1 shows that the total revision rate of cemented implants is reduced in cementless implants as well as almost all individual reasons for revision being reduced. The commonest cause of revision in both cemented and cementless UKR's is progressive arthritis, in which cementless UKR has a lower revision rate than cemented (2.45 – 3.52) and may be treated in both cases by revision to TKR. However, particularly notable is the reduction in the second most common reason for revision in cemented joints, Aseptic loosening / lysis, which is ~3 times (2.82 / 0.88) more prevalent in cemented UKR joints than cementless UKR joints.

The notable exceptions to the general reduction in revision rate from cemented UKR to cementless UKR being dislocation, infection, and periprosthetic fracture. It is further notable that the order of the most prevalent cause of revision changed from cemented to cementless, with dislocation and implant wear being the most prevalent in the cementless data, after progressive arthritis. This is likely due to the much higher representation of mobile bearing joints in the cementless data as compared to the cemented data, as bearing dislocation is likely to be more common in mobile bearing joints, and that the replacement of mobile bearings may be a more minor surgery than a fixed bearing.

Furthermore, while the rate of infection is nominally higher in the cementless bearing the 95% confidence intervals overlap to such an extent that it is difficult to make a definitive claim on the nominal difference in these values. However, the periprosthetic fracture caused revision rate stands out, at ~3 times (0.54 / 0.19) more prevalent in cementless than cemented UKR. This is a particularly concerning factor as periprosthetic fracture is a very severe complication (Della Rocca, Leung and Pape, 2011; Burger *et al.*, 2021).

The Oxford Unicompartmental Knee (OUKR), Figure 1.1, is a mobile bearing UKR which was originally a cemented knee replacement which was changed in 2004 with the introduction of the cementless Phase 3 knee (Goodfellow *et al.*, 2015). Recent studies have likewise shown the cementless OUKR has improved outcomes, when compared to the cemented variant, in a range of areas, including: aseptic loosening, and disease progression. However, the same study has shown that the Phase 3 cementless OUKR has an increased periprosthetic fracture rate, in western populations, from 0.1% to 0.2% (Mohammad *et al.*, 2021 Table 5).

Further work has also shown a similar pattern with an increased prevalence of fracture of up to ~8% in Japanese populations (Hiranaka *et al.*, 2020) and ~7% in Chinese populations (涂 *et al.*, 2012; Yudong *et al.*, 2022). Furthermore, a large difference in sex specific risk was shown in both populations: from ~1.5% in Japanese male patients (1/65 participants) to ~11% in Japanese female patients (16/146 participants) (Hiranaka *et al.*, 2020) and ~10% risk in Chinese female patients (12/122 participants) (涂 *et al.*, 2012; Yudong *et al.*, 2022), with no recorded fractures in the male patients. No recorded fractures in the Chinese male population is to be expected due the population size of 45 participants and the low risk of fracture in Japanese patients: 1/65 male participants, from the work done by Hiranaka *et al.* (2020). Both studies had comparable female participant population sizes.

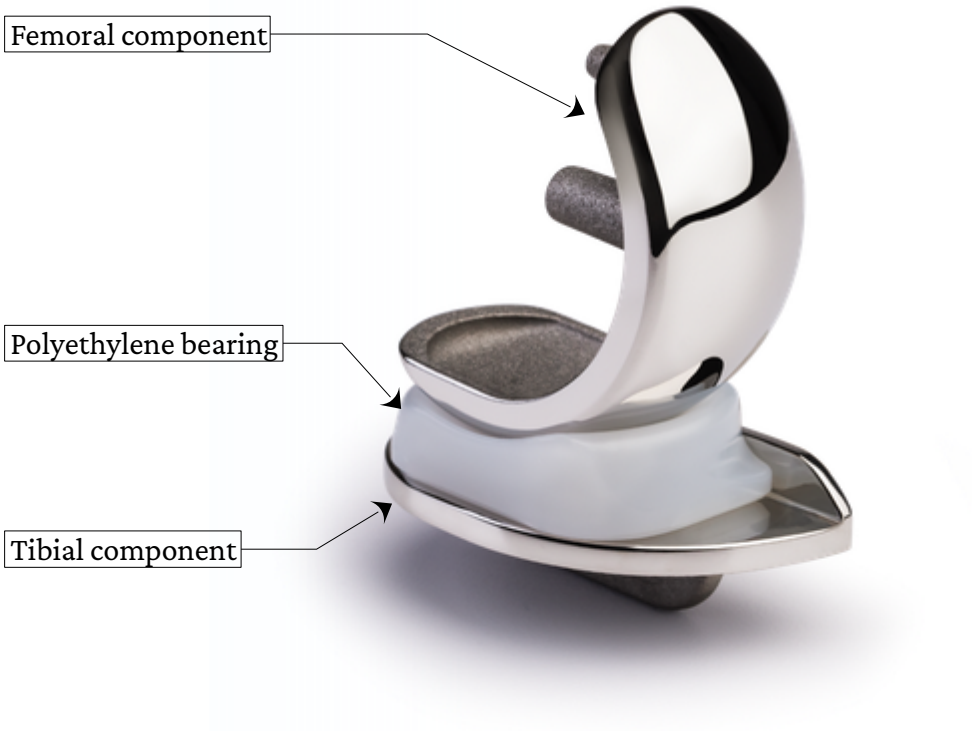

Figure 1.1: The Oxford Unicompartmental Knee (OUKR). Image is adapted from Zimmer Biomet's website on the OUKR (Zimmer Biomet, 2025b).

1.4 An engineering view of periprosthetic fracture risk

The periprosthetic fractures occur in the tibia, seemingly from the interaction between the tibial component and the bone it is seated in. It has been suggested that the crack which leads to fracture may be initiated by the implantation process which requires high initial forces to seat the component (~1400N in PCF 20 polyurethane foam) (Pandit *et al.*, 2007; Mohammad *et al.*, 2018). Furthermore, the increased risk of fracture has been linked to a geometrical constraint of the tibia, specifically a relation described by Yoshikawa *et al.* (2020) as the medial eminence line (MEL). The intercondylar eminence is a bony ridge between the medial and lateral condyles of the proximal tibia, running from the anterior tibia to the posterior tibia (Snell, 2004). This intercondylar eminence forms in two co-running peaks, each peak being either more medially or more laterally located. The MEL is a line drawn from the peak of the medial eminence parallel to the tibial axis (TA). The tibial axis was defined by Yoshikawa *et al.* (2020) as the line drawn between the centre points of two lines each drawn between the outline of the tibial shaft, at distances of 60mm and at 120mm below the knee joint line on an x-ray of the patients knee. This is shown in Figure 1.2, which is adapted from Fig. 2 in Yoshikawa *et al.* (2020).

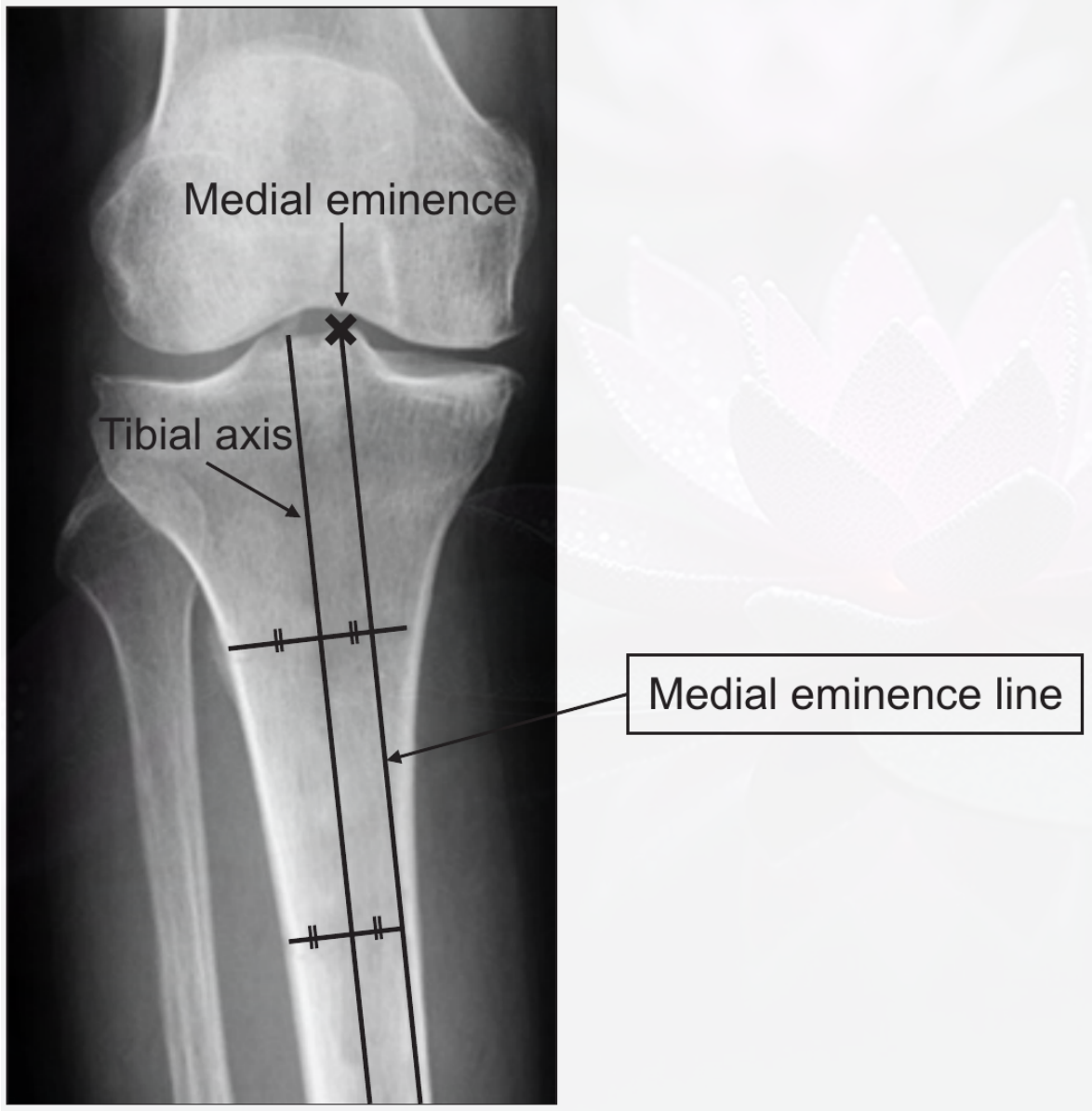

Figure 1.2: The way tibial axis and medial eminence line (MEL) are constructed as described and adapted from Yoshikawa et al. (2020 Fig. 2).

Yoshikawa *et al.* (2020) further split a group of Japanese patients, that included patients that had undergone periprosthetic fracture, into two groups: one where the MEL did not extend beyond the tibial outline and one where the MEL did extend beyond the tibial outline (shown in Figure which was adapted from Yoshikawa *et al.* (2020 Fig. 3)).

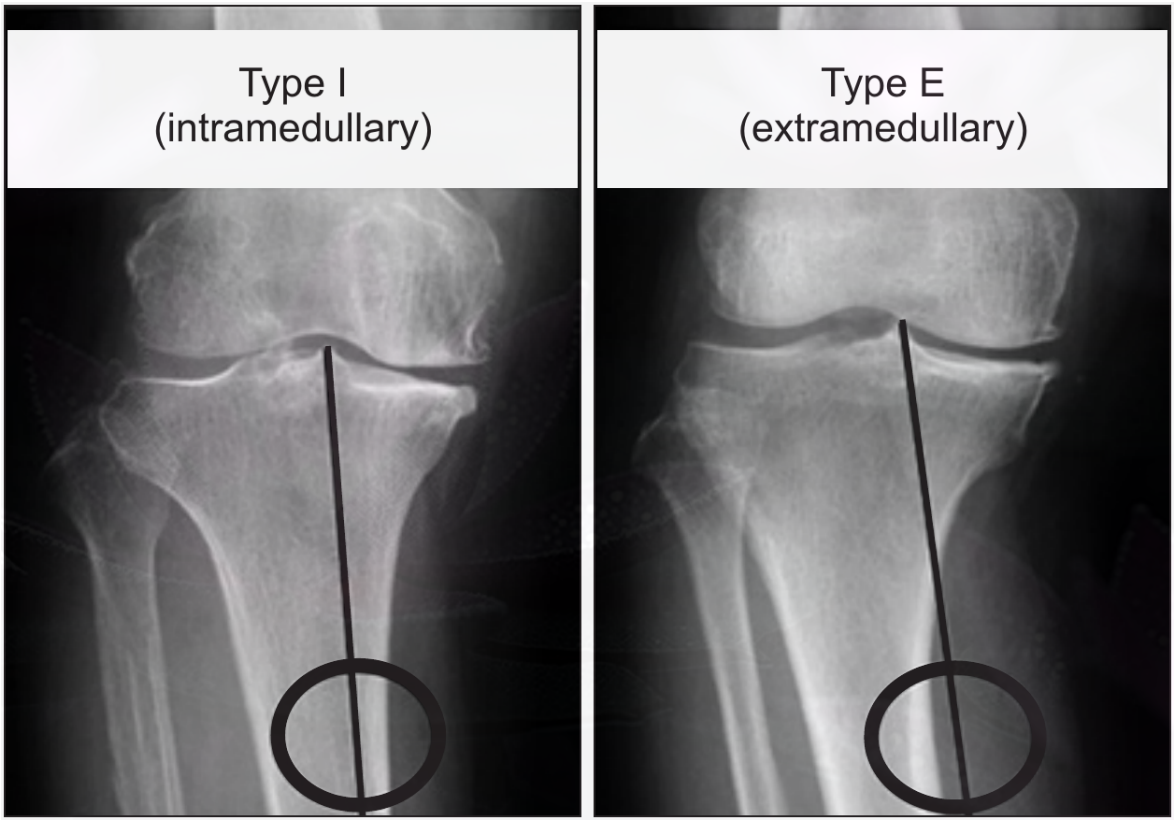

Figure 1.3: The group classification that Yoshikawa et al. (2020) used to show a significant relation between periprosthetic fracture and geometrical relation.

In this study, Yoshikawa *et al.* (2020) showed that in patients who had undergone periprosthetic fracture the condition where the MEL did extend outside of the tibial outline was significantly ($p<0.05$) more common (Yoshikawa *et al.*, 2020). Hiranaka *et al.* (2020) confirmed this result using the same method in a multicentre study. Principally that in patients who had the MEL extending outside the tibial outline, there was a higher rate of fracture 29% (12/41) compared to those that did not 3% (5/171) ($p<0.001$) (Hiranaka *et al.*, 2020).

Hiranaka *et al. (2020)* also found a statistically significant relationship between fracture rate and size of component. Standard components, classified as size B or higher, had a fracture rate of 5% (8/176) and very small components, classified as A or lower, had a fracture rate of 25% (9/36) ($p<0.001$) (Hiranaka *et al.*, 2020). Where a combination of patients classified as "MEL outside" and small and very small components made up the majority of the fracture risk of the group 23% (15/65) compared to ~1% (2/147) ($p<0.001$) for all other patients. Furthermore, the male patients were statistically significantly less likely to have smaller components ($p<0.001$), and the female patients were significantly more likely to be classified as having the MEL extending outside the tibial outline than the male patients ($p=0.003$) (Hiranaka *et al.*, 2020). It should be stated that Yoshikawa *et al.* (2020) found no statistically significant sex specific relation to MEL classification. However, Hiranaka *et al.* (2020), being a multicentre national study, has more weight in this regard and so where the two studies contrast, Hiranaka *et al.* (2020) will be taken to be more representative.

The finding of smaller patients suffering more fractures is important because in the OUKR, traditionally, the fixation geometry has not varied in size with the tibial plateau of the tibial component, meaning that proportionally to the size of the bone, the fixation geometry was larger for smaller patients. The suitability of patient bone size for UKR has been a concern for a number of years with some evidence suggesting that this may negatively effect populations as wide spread as Turkey (Küçükdurmaz *et al.*, 2014; Lu *et al.*, 2020), Korea (Surendran *et al.*, 2007; Lu *et al.*, 2020), and China (Cheng *et al.*, 2010; Lu *et al.*, 2020). Following this idea, it has been suggested by Lu *et al.* (2020; Yudong *et al.*, 2022) that the Oxford phase 3 tibial components may be incompatible with as many as 71.3% of Chinese patients.

This size incompatibility is quite an important finding. However, the effect of tibial fixation geometry, known as the keel (Figure 1.4), size has been studied extensively and a new proposed tibial geometry that maintains the same form factor of the current geometry and similar fixation properties, but with smaller size has been proposed by Rahman (2022) in his Doctoral thesis. This design has not yet entered clinical use and its effects, while promising, cannot be measured as of yet.

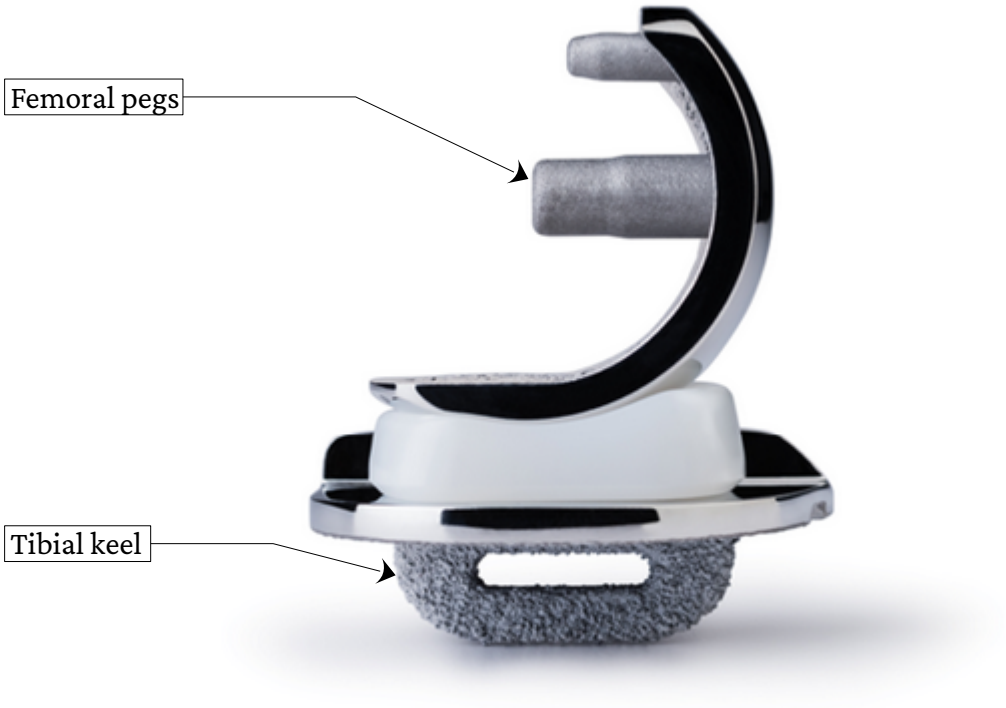

Figure 1.4: A side view of the OUKR, with particular call outs to the femoral and tibial fixation geometry, the femoral pegs. The image is adapted from Zimmer Biomet's website on the cementless OUKR (Zimmer Biomet, 2025a).

The MEL concept is interesting from an engineering perspective, specifically because it lines up with a model of the tibial plateau as a cantilever beam. It is understood that the axial stress generated in a canter lever beam is given by Equation 1.1.

$$\sigma = \frac{My}{I} \qquad \text{(Eq. 1.1)}$$

Where σ is the axial stress at height from the neutral axis of the shape y in the beam. M is the applied moment at the evaluation point along the length of the beam and I is the second moment of area of the beam. The second moment of area of the beam is a geometrical relation of the cross sectional area of the bean perpendicular to the axis of the stress being evaluated and essentially measures how much area is far away from the centroid of the cross section. The structure will be susceptible to failure, yielding or fracture, in the case that the stress applied to the material is greater than the yield strength of that material; or fatigue failure if the stress is cyclic (walking for example) and is over a certain proportion of the yield strength of the material. This proportion is a value which is referred to the fatigue limit of the material. The fatigue limit, if the material has one, is a material specific parameter.

From Equation 1.1 it can be seen that to reduce the stress of the bone at the evaluation point, it is necessary to either reduce the moment (perpendicular force multiplied by distance) or to increase the second moment of area of the cross section. The initial cut location of the knee surgery is constrained by the medial side of the intercondylar eminence (Goodfellow *et al.*, 2015), and so there is limited placement flexibility to move the OUKR into the joint to reduce the moment arm. However, high force of insertion may be a contributing factor to fracture or fracture initiation (Mohammad *et al.*, 2018) and can be addressed.

Studies to reduce the insertion force and to minimise tibial fracture, while retaining fixation, have been conducted experimentally, showing that with proper interference control (from 1.3mm – 0.9mm to closer to an optimal of 0.7mm – 0.5mm) the insertion force for the current tibial design can be reduced from 1411N (±180N SD) to 789N (±131N SD) while maintaining fixation in polyurethane foam (Campi *et al.*, 2018; Mohammad *et al.*, 2018). However, the inherent design of the current fixation geometry, the keel, may be sub-optimal for periprosthetic fracture due to the amount of bone removed to allow for insertion. Larger fixation geometry has been shown to contribute to a greater ease of fracture in polyurethane foam (Rahman, 2022 Fig. 7.3).

This makes intuitive sense as removing material from the bone would reduce the second moment of area of surrounding bone, increasing the stress experienced in bending by the structure, which in turn would lead to higher strains under comparable loading. Schileo, *et al.* (Bayraktar *et al.*, 2004; 2008) have shown a consistent fracture strain for bone, which has been used in recent risk of fracture studies (Pegg *et al.*, 2020). From this it is evident that a higher strain in the structure would lead to an increased likelihood of fracture. Therefore, it stands to reason, that a further reduction in the volume of bone resected, preserving more of the pre-resection second moment of area of the tibial plateau, may reduce the probability of fracture further. An indication that this analysis may be correct is given by the work of Rahman (2022, p. 187 Figure 7.3) where he shows an increase in the force to fracture for a similarly shaped but smaller keel slot compared to the conventional slot, 710N for the conventional slot and 904N from the smaller slot. This result was statistically significant with a p value of 0.0003 (Rahman, 2022, p. 187). However, without specific measurements and calculations for the second moment of area of the tibial plateau section, this relationship is only indicative not definitive.

1.5 Indications for the Oxford Knee

The OUKR is not currently suitable for all patients, specifically that UKR requires the surrounding knee to be intact for a successful outcome, whereas TKR has the benefit of not having this stringent requirement (Goodfellow *et al.*, 2015). For example, in the medial compartment with anteromedial osteoarthritis, indications for the OUKR are taken from Goodfellow *et al.* (2015):

1. Pain that justifies joint replacement
2. An intact anterior cruciate ligament (ACL)
3. Full thickness cartilage loss, with eburnated bone on bone contact, in the medial compartment an Ahlback stage 2, 3, or 4 (Ahlback, 1968; Goodfellow *et al.*, 2015)
4. Full thickness cartilage preserved in the lateral compartment
5. Intact medial articular surface at the back of the tibial plateau and femoral condyle
6. Intra articular varus deformity that is manually correctable in 20 degree flexion by valgus stress.

If these conditions are not met, it is recommended that the another, more suitable, joint is used (Goodfellow *et al.*, 2015), usually a TKR.

1.6 Pseudostatic mechanical considerations of bone

Bone is a ceramic biological fibre composite which has different micro, meso, and macro properties, each of which varies on location and loading. The macro level of the bone can be separated into cortical and trabecular, also called cancellous, bone (Gibson and Ashby, 1997). The cortical bone is the solid outer layer of the bone, that can be thick in the middle of the bone length, or comparatively thin on the proximal or distal ends. The meso scale the structure of the bone can be called Haversian where "pillars" of concentric bone are formed around Haversian canals that run axially along the bone with Volkmann canals running transverse to the bone axis (Gustafsson, 2019). It has been suggested that aspects of the cortical bone may be sex specific (Abdullah, Mohd Nor and Abdul Jamil, 2016), and that under tension mammalian bone may form non-Haversian structures better suited to the experienced loading conditions, which has been demonstrated in bovine samples (Mayya, Banerjee and Rajesh, 2016). On the micro level, there are collagen fibres and individual cells that resorb old or damaged bone, osteoclasts, and lay down new bone, osteoblasts.

These structures all contribute to the mechanical properties of bone and, importantly, the bones of a living human are living tissue, constantly adapting to the loads they are put under and in particular adapting to the principle stress directions they exist under (WOLFF, 1869; Thompson, 1961; Currey, 1984; Gibson and Ashby, 1997). How the bone, the cells, and structures are able to adapt and grow in this way is not fully understood, but it has been suggested that the piezoelectric nature of bone under load may have a role in this remodelling behaviour (Thompson, 1961; Currey, 1984; Gibson and Ashby, 1997).

The mechanical properties of bone are variable and anisotropic which is due to patient variability and biological processes such as remodelling. Trabecular bone is a foam of a similar material to solid bone and some have treated it as the same material (McElhaney *et al.*, 1970; Townsend *et al.*, 1975; Townsend, Rose and Radin, 1975; Carter and Hayes, 1977; Gibson, 1985; Gibson and Ashby, 1997). Foams have an apparent modulus, which is dependant on the apparent density of the foam, that is a ratio of the modulus of the solid material (Gibson and Ashby, 1997). For tibial trabecular bone of density 0.3 gcm^{-3} the apparent modulus has been suggested to be in the range 14MPa – 345MPa (Hvid *et al.*, 1983; Linde, Hvid and Pongsoipetch, 1989; Mohammad *et al.*, 2018) and for density of 0.6 gcm^{-3} a range of 800MPa – 2700MPa is suggested (Carter and Hayes, 1977; Carter, Schwab and Spengler, 1980; Bensusan *et al.*, 1983; Hvid *et al.*, 1989; Linde *et al.*, 1991; Gibson and Ashby, 1997 Fig. 11.7). Establishing the modulus of the solid has posed more of a challenge with a larger range 1.3GPa – 13.0GPa (Williams and Lewis, 1982; Ashman and Jae Young Rho, 1988; Gibson and Ashby, 1997) and in more recent work 1.3GPa – 22.3GPa (Smith, Schirer and Fazzalari, 2010; Milovanovic *et al.*, 2012; Wu *et al.*, 2018). However, cortical bone has been suggested to have a modulus of 16GPa – 17GPa (Currey, 1984; Choi *et al.*, 1990; Gibson and Ashby, 1997) so the upper and lower bounds of the ranges for trabecular bone seems excessive. This may be due to the difficulty of obtaining accurate data for the modulus of the solid from the foam itself, due to anisotropy and density variations in specimens, as well as the state of the bone. Some of the data was produced from dry bone which may have different properties to living wet bone. A range of 8.7GPa – 11.4GPa for wet bone has been suggested to be a reasonable estimate for the solid modulus of trabecular bone (Runkle and Pugh, 1975; Townsend, Rose and Radin, 1975; Gibson and Ashby, 1997).

However, as the large ranges demonstrates, there is much work to be done in this area, narrowing down the values of the solid of trabecular bone, and, in particular the variables that may influence the properties of that material, such as age, the make up and fibre content of the composite (Fish, 2010; Prada *et al.*, 2022) as well as sex, diet, etc.

Trabecular bone fails in a predictable way as many foams do, that is with a linear elastic rise, a yielding phase, a pseudo-plastic phase, and a consolidation phase where the foam begins to stiffen, eventually achieving properties that are comparable to the solid material. The relative proportions of these phases and the strain ranges over which they take place are dependant on apparent density of the trabecular bone which is demonstrated graphically by Figure 1.5.

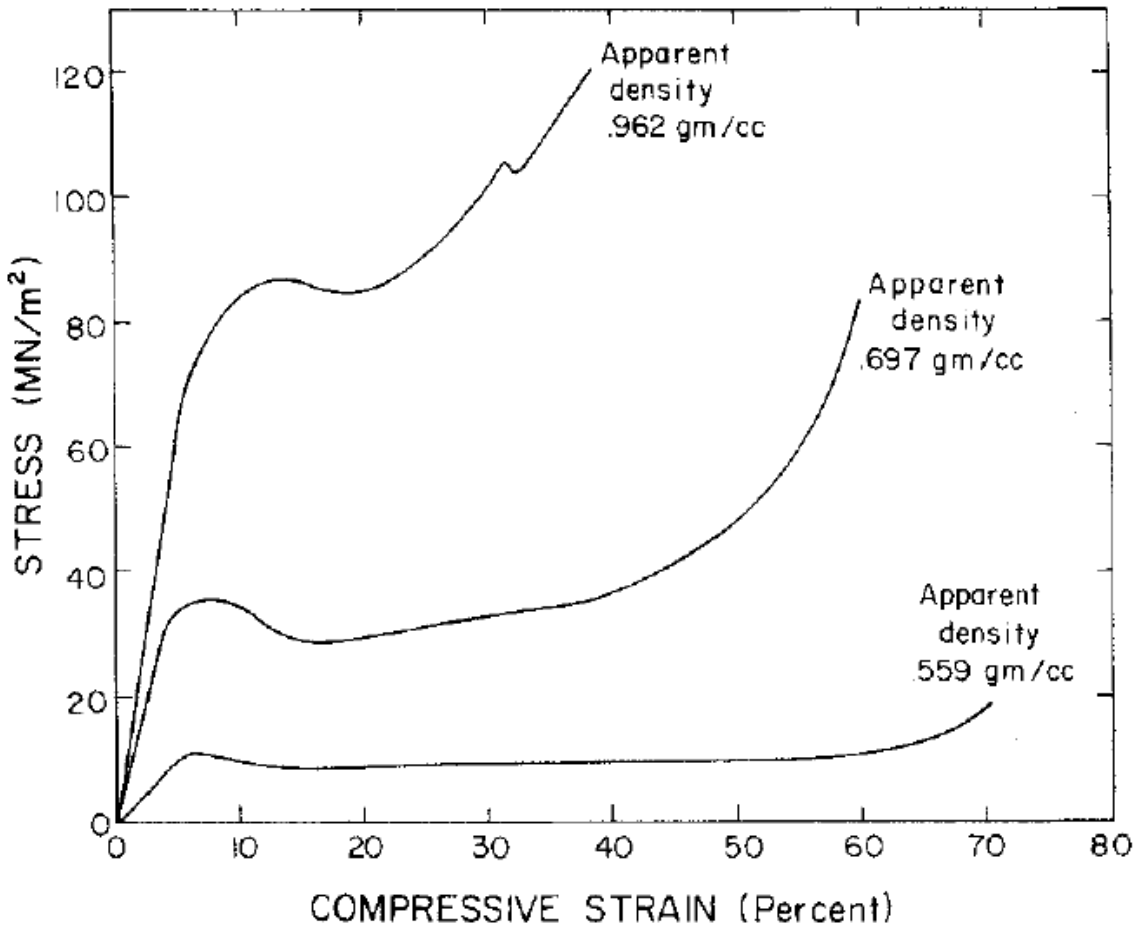

Figure 1.5: Compressive stress behaviour under strain for various densities of bone, adapted from Hayes and Carter (Perkins, Jorgensen and Sommer, 1958; 1976 Fig. 1a).

1.7 Stress relaxation of bone

As well as pseudostatic mechanical properties bones, and in specific, trabecular bones show viscoelastic properties, one of which is stress relaxation. Berahmani *et al.* (2015) found a 33% reduction in pull-out force after letting the inserted implant rest in the femoral trabecular bone for 30 minutes, which may raise the question that if stress, and therefore holding force, reduces over time postoperatively, then is it possible that any fixation is reduced to zero over time. Therefore negating any benefits from efforts to optimise implants for primary fixation.

Stress relaxation in foams has been studied extensively, with Gibson *et al.* (1997) providing an equation (Equation 1.2) that had been developed to model the steady state stress state of a foam placed under constant strain. Equation 1.2 can be used to model the constant strain that an implant inserted in interference fit may impose own the foam.

$$\sigma = C_1 \rho_r^2 E_{s1} \varepsilon \{1 - \frac{E_{s1}}{E_{s1}+E_{s2}} \left(1 - e^{\frac{E_{s1}+E_{s2}}{\eta_s}\tau}\right)\}$$ (Eq. 1.2, (Gibson and Ashby, 1997 Eq. 6.4))

Where σ is the stead state stress, C_1 is a material specific coefficient, ρ_r is the ratio of the apparent density of the foam to the solid density, E_{s1} is the solid modulus, E_{s2} is related to the solid relaxed modulus (specifically the solid relaxed modulus is $\frac{E_{s1}E_{s2}}{(E_{s1}+E_{s2})}$ (Gibson and Ashby, 1997)), η_s is the viscosity of the solid, τ is the time. From Equation 1.2 it can be seen that as time increases to infinity the stress will tend towards Equation 1.3.

$$\sigma \approx C_1 \rho_r^2 E_{s1} \varepsilon \left(1 - \frac{E_{s1}}{E_{s1} + E_{s2}}\right) \quad \text{(Eq. 1.3)}$$

From which it can be seen that as long as $E_{s2} > 0$ then $\sigma > 0$ where the steady state stress will depend on the strain and the post relaxation solid modulus. In a interference fit, the initial normal force will depend on the interference and for pegs in Berahmani *et al.* (2015) it was observed that in smooth implants an average 33% reduction in pull-out force was seen over 30min, and 13% over the same time for rough implants, though this was increased in a high interference group to 38% and 29% in the low interference group.

Gersie *et al.* (2025) saw a similar drop for TKR femoral implants over a 24h time period. Pull-out force reduced by 17% – 37% based on specimen. However, this varied substantially based on location, a 49% pull-out force reduction for one of the specimens in the posterior lateral condyle. The similarity of these results suggests that at between 30 minutes and 24 hours a steady state stress has been achieved in the Cadaveric bone giving a suggestion that the asymptote of the relaxation curve is non-zero. Moreover, this result is a non-zero stress state and as is shown by Berahmani *et al.* (2015) the residual stress left shows a non-zero differential between the low interference and the high interference, even in the high interference group, where bone abrasion was more prevalent for the same interference. Which comports with cementless UKR implants having a competitively rare failure rate due to aseptic loosing, 0.88 (0.76-1.02 95% CI) (Reed *et al.*, 2024), a figure which would likely be higher if all primary fixation generated by the interference fit was lost due to stress relaxation. Therefore, if an improved implant targets the same interference for a higher fixation force or a lower interference but the same fixation force there is likely to be a remaining improvement after the stress relaxation has occurred.

Indeed if a lower interference and therefore lower averaged stress is introduced, assuming the initial hole in the bone is expanded uniformly, it is possible that the post relaxation performance benefits of such an optimised geometry may be greater than those measured immediately postoperatively.

1.8 Bone marrow's impact on the coefficient of friction of bone

Bones contain more than just the cortical and trabecular material, and are more than just load bearing structures; they are systems that have many crucial functions within the body. In central cavity of the long bones is the marrow, which contains the pluripotent stem cells that replace elements of the blood (Cabrita *et al.*, 2003; Gurkan and Akkus, 2008). Moreover, and importantly for the consideration of primary fixation, bone marrow is also present in the porous trabecular bone structure.

This means that when the bone is resected to insert the implant, there will be fluid interacting with the surface of the implant and that has the possibility to act as a lubricant and reduce the coefficient of friction between the bone and implant, which may degrade primary fixation. However, the current implant is successful under these same conditions and therefore maintaining the current implants surface roughness, also necessary for the development of secondary fixation, will be an important element of a final design that is ready to move on to clinical testing.

1.9 Finite element analysis

Due to the previously mentioned second moment of area considerations, a possible remedy for the stress induced by implant insertion is the use of pegs to replace the keel as the geometry for primary fixation on the underside of the tibial component. Primary fixation holds the implant from immediately postoperatively to when secondary fixation is achieved. This process begins at 6-8 weeks postoperatively (Parithimarkalaignan and Padmanabhan, 2013; Kohli *et al.*, 2018; Kohli, Stoddart and Van Arkel, 2021). Two round nose pegs have previously been shown to be at least as good for primary fixation as the current design keel as well as reducing the risk of fracture in PCF 20 polyurethane foam (Rahman, 2022). The design and analysis of these pegs, as well as analysis of other possible designs, is not yet fully optimised and therefore, it will be a goal of this thesis to optimise a peg for primary fixation.

Smaller experimental studies have been done on cadaveric and polyurethane foam studies (Berahmani *et al.*, 2015; Campi *et al.*, 2018; Mohammad *et al.*, 2018). However, running through the full gamut of possible design iterations with physical prototypes is very costly, time consuming, and generally less practical than using computational methods for initial testing of designs. As such, a method to evaluate pegs cheaply and quickly would therefore allow more rapid design iteration and convergence on an optimal cementless design, which can then progress to more in depth experimental and clinical evaluation.

Finite element analysis (FEA), a method by which a surface or solid is divided into a "mesh" of small discrete units, or finite elements, and displacements acting on the elements are solved iteratively, is well used in the engineering world for analysis of new or existing designs (Liu, Li and Park, 2022).

Using this method it is possible to "simulate" a physical interaction between two objects, calculating displacements and the resulting forces. FEA had its foundling birth in the early 1940's (Hrennikoff, 1941; Liu, Li and Park, 2022) and was widely adopted in from the 1960's onwards (Clough, 1960, 1990; Liu, Li and Park, 2022); being extensively applied to the problem of simulating the insertion of orthopaedic implants (Ovesy, Aeschlimann and Zysset, 2020).

Cementless implants rely on the on the pseudo-plastic response of the bone for primary fixation and so require a material model that is capable of capturing the complexity of this behaviour to model the peg-foam interaction properly. There are two design critical forces: the force required to insert the component, the push-in force, and the force required to extract the component, the pull-out force. This work will focus on the simulation of the latter, as pull-out force may be used as an analogue of primary fixation.

1.10 Material models

A crucial part of the behaviour of the simulated interaction is the material model which is used. Success in modelling the mechanical behaviour of bone has predominately been tackled in two ways: micro-level simulation (Gustafsson, Wallin and Isaksson, 2019; Werner, Ovesy and Zysset, 2019), and macro-level simulation (Schwiedrzik, Wolfram and Zysset, 2013; Ovesy, Aeschlimann and Zysset, 2020). This work will focus on a macro-level approach as the micro-FE approach requires huge computational resources to model more than a small section of material, much more still for a whole region of a limb; a requirement which may become necessary for the future development of implants. Macro-level material models can largely be split into two broad categories: elastic, and plastic models. Elastic models assume no mechanical damage and so the material will return to its prestressed strain when the load is removed. Plastic models allow mechanical damage and therefore allow residual strain to remain after the load is removed. Plastic models can be further categorised by their failure surface and the way that plasticity is modelled.

Both types of models have been used in simulation of stress response of bone, with differing goals. A linear elastic material model was used by Pegg, *et al.* (2020) and Gray, *et al.* (2010) to model periprosthetic strains in the proximal tibia under loading. Pegg, *et al.* (2020) showed that under normal physiological loading the linear elastic model predicted strains reaching many times the defined fracture strain (Schileo *et al.*, 2008) of the material. More recent work by Macaulay, *et al.* (2024) used a linear elastic model to simulate the insertion of a cementless implant, where the interference was changed to achieve pull-out force matching with those of higher experimental interferences. Both of these studies imply non-linear material behaviour, yielding, in the areas of highest stress.

Previous work with ABAQUS (Dassault Systemes, 2020) user material interface (VUMAT) models has proven enormously successful in modelling cementless insertions (Ovesy, Indermaur and Zysset, 2019; Ovesy, Aeschlimann and Zysset, 2020). VUMAT's can capture detailed material behaviour, yielding or otherwise. However, VUMATS are complex to implement and therefore are only needed when standard models do not sufficiently capture the complexity of the material behaviour.

Two common yield criteria are Von-Mises and Drucker-Prager. The von-Mises criterion is an idealised yield criterion that is suitable for predicting isotropic ductile material failure (Mises, 1913, 1928). The Drucker-Prager model a development of the von-Mises criterion, to account for behaviour in soils where the compressive failure point of the soil increases as the soil is hydrostatically compressed. As bone exhibits pseudo-ductile yield and compression hardening behaviour, some success has been had using a Drucker-Prager criterion to model compression failure in nano indentation studies (Adam and Swain, 2011; Toal. V., 2013). The parameters of this model were taken from the work done by (Mullins, Bruzzi and McHugh, 2009), and (Carnelli *et al.*, 2011). Both von-Mises and Drucker-Prager criteria can be used with either perfectly plastic or plastic hardening post-yield models. In a perfectly plastic model the post-yield stress remains constant whereas in a plastic hardening model, the material stress is altered following a lookup table of plastic strain and the corresponding stress.

A further plasticity model known as a crushable foam model has been used to model bone compression (Kelly, Harrison, *et al.*, 2013); primary fixation in hip joints; and total knee replacements (Kelly, Cawley, *et al.*, 2013; Jakobi *et al.*, 2021). However, the model specific parameters, k and kt, require extensive characterisation to relate directly to material data and therefore will not be used in this study.

1.11 Material characterisation of polyurethane foam

Polyurethane (PU) foam has a long history of being used as a trabecular bone analogue (Szivek, Thomas and Benjamin, 1993; Kelly and McGarry, 2012; Campi *et al.*, 2018), during which time much work has been done on attaining the basic mechanical properties of the polyurethane foams notably by Szivek, *et al.* (1993), Szivek, *et al.* (1995), Thompson, *et al.* (2003), Calvert, *et al.* (2010), and Kelly, *et al.* (2012). The ASTM standard (American Society for Testing and Materials, 2008) for ridged polyurethane foam was introduced to provide a standard set of physical and mechanical properties of PU foams for testing orthopaedic devices and instruments, discretised by apparent density. Much of the current use of PU foams has relied on PCF 20 grade (Sawbones, 2022). However, other densities of PU foam are available from Sawbones. The density of a foam has an impact on the expressed mechanical behaviour of the foam and thus would be expected to also have an impact on how orthopaedic devices behave both during and after insert into that foam. Therefore mechanical characterisation of these PU foams is enormously important for future development of orthopaedic devices as design attitudes move towards a more subject specific approach.

Characteristic compression behaviour is shown by both polyurethane and trabecular bone, starting linearly, and then progressing to pseudo-plastic and consolidation regions post-yield. A typical bone compressive material curve under different densities is demonstrated in the work of Hayes and Carter (1976), Figure 1.5.

Rigid PU open cell foams are expected to behave approximately in accordance with three equations laid out in "Cellular Solids" by Gibson and Ashby (1997) that link mechanical properties of the foam with the properties of the solid through the ratio of a foams apparent density to the density of the solid (density ratio). These equations are:

$$M_r = C_1 \rho_r^2 \qquad \text{(Eq. 1.4, (Gibson and Ashby, 1997 Eq. 5.3))}$$

Where M_r is the ratio of foam modulus to the to the solid modulus (modulus ratio), C_1 is a material specific coefficient, and ρ_r is the density ratio.

$$E_{yr} = C_4 \rho_r^2 \qquad \text{(Eq. 1.5, (Gibson and Ashby, 1997 Eq. 5.16))}$$

Where E_{yr} is the ratio of elastic yield stress (elastic collapse stress) of the foam to the modulus of the solid (elastic yield ratio), and C_4 is a material specific coefficient.

$$P_{yr} = C_5 \rho_r^{\frac{3}{2}} \qquad \text{(Eq. 1.6, (Gibson and Ashby, 1997 Eq. 5.24))}$$

Where P_{yr} is the ratio of plastic yield stress in the foam to the modulus of the solid (plastic yield ratio), and C_5 is a material specific constant.

Previous work on the mechanical properties of altering densities of PU foams has generally taken two forms, either a description of the mechanical properties of the foams (Szivek, Thomas and Benjamin, 1993; Szivek, Thompson and Benjamin, 1995; Kelly and McGarry, 2012), or the description of material data and subsequently fitting of equations of best fit to this data (Thompson *et al.*, 2003; Calvert *et al.*, 2010).

Thompson, *et al.* (2003) used the open cell equation forms and allowed both coefficient and the power to alter in the fitting process and Calvert, *et al.* (2010) used the closed cell version of the equations previously presented. The equations for open cell foams are less complex to use and rely on fewer material parameters, specifically the fraction of solid in the edges of the cells or ϕ, and so may be beneficial if they can be used with sufficient predictive accuracy in the case of a closed cell foam.

Both the elastic yield stress and plastic yield stress are taken as the foam yield stress. However, the accuracy of prediction of each equation is again expected to vary based on the dominant failure mechanism in the foam which in turn depends on both the foam density and the foam cell morphology, between thin and slender struts and thick struts. The two different failure mechanisms present in the foam cause a variation in the respective mechanical properties; requiring prediction by different equations. The elastic yield ratio, where the struts of the foam fail via buckling and the failure mechanism predominant in relative low-density foams, is predicted using the elastic equation (Equation 1.5). Where the struts fail plastically, the failure mechanism dominant in relatively high-density foams, the yield ratio is predicted using the plastic equation (Equation 1.6).

An indication of which mechanism is likely to be dominant is given by the following equation:

$$\rho_r > 36 \left(\frac{\sigma_{ys}}{E_s} \right)^2$$ (Eq. 1.7, (Gibson and Ashby, 1997, p. 205 Eq. 5.26))

Where σ_{ys} is the yield stress of the cell wall material i.e. the yield of the solid, and E_s is the modulus of the solid.

1.12 Orthopaedic design for primary fixation

Orthopaedic fixation devices form the primary interface with the bone in a replacement joint, and as such have been researched extensively with varying fixation geometries put forward for achieving sufficient performance, predominately: screws (Ovesy *et al.*, 2022), pegs (Bahraminasab *et al.*, 2014), keels (Campi *et al.*, 2018), or a variation on these basic features (Jyoti and Ghosh, 2023b), sometimes being blended together as is shown on the Persona The Personalized Knee from Zimmer Biomet (Figure 1.6).

Figure 1.6: Zimmer Biomet's Persona Knee showing a blended peg and keel fixation geometry on the tibial component (Zimmer Biomet, 2025c).

This implants tibial component has a peg form fixation geometry with a keel like structure towards the tibial plate which may be to increase the rotational stability of the implant. Each of the geometries, peg, keel, etc. have advantages and drawbacks. A single peg alone has little rotational stability unless grooves or other features, such as the blended keel in Figure 1.6, are introduced to mechanically resist rotation. Keels on the other hand may be good for rotational stability but have been shown to require higher forces for insertion than pegs that provide equivalent primary fixation as well as reducing the fracture force of a PU tibia than those pegs, in the case the OUKR (Rahman, 2022). This may be due to the amount and shape of the material removed for the keel, reducing the second moment of area of the tibial plateau more than the same for the pegs, which are drilled holes. In turn, this suggest that in the case of a UKR like the OUKR, a keel for tibial fixation my be less effective than a peg, both from a primary fixation and risk of fracture stand point.

Screws are similar to pegs and also give very good fixation in relation to their insertion force. However, screws are difficult to incorporate into multi-fixation point designs (van Arkel *et al.*, 2018). Whereas, pegs are a versatile and widely used form of fixation geometry, having been used on both femoral components (Bahraminasab *et al.*, 2014; Sun *et al.*, 2024) and other implants (Geraldes, Hansen and Amis, 2017). Furthermore, pegs may have an advantage over keels that provide similar primary fixation in a reduction of periprosthetic fracture risk, in some tibial components (Rahman, 2022).

The fixation geometry of an orthopaedic insert must achieve two main goals: primary fixation and secondary fixation. Primary fixation is the immediate post-operative mechanical fixation of the implant in the bone, and must resist the forces applied to the component while the secondary fixation, bone ingrowth or osseointegration, develops.

Sufficient primary fixation increases the likelihood for sufficient secondary fixation to develop. This is caused by limiting micro-motions between the bone and implant which, if excessive, can prevent osseointegration (Kohli, Stoddart and Van Arkel, 2021). Further, development of good secondary fixation requires a somewhat porous surface which can be rough and may lead to a reduction in pull-out force by abrasion of the hole (Rahman, 2022). As there are two competing objectives with difference physical conditions, primary and secondary fixation, it would be possible to use a method known as multidisciplinary or multi-physics optimisation in the solution of this design problem.

Multidisciplinary optimisation is a process where different physical conditions that the design must satisfy are varied together in a simulation, thereby searching the whole design space (Martins and Lambe, 2013). Due to this search of the design space, many more simulations are required when using a multidisciplinary approach, and thus incurs a very heavy computational overhead. Therefore, this study will focus on the optimisation of maximum primary fixation and leave the optimisation of secondary fixation as a goal for future studies.

Primary fixation is generated in two main ways: direct mechanical interaction i.e. barbs that dig in to the bone (van Arkel *et al.*, 2018); and frictional interaction i.e. two surfaces that are held in close contact generating a normal force on the implant geometry which resits movement of the implant. There is another approach which should be mentioned for completeness, but is beyond the scope of this study: adhesion, or bonding the two materials together with chemical bonds i.e. gluing the implant into the bone socket. Moreover, primary fixation may be evaluated by a push-in and pull-out test where the implant is pushed into the surrounding material, simulating surgical implantation, and then pulled out again, allowing the maximum retraction force to be measured.

This retraction force is the minimum force the implant would have to overcome to retract from the surrounding material and so is analogous to the primary fixation, and is a commonly used comparative metric (Campi *et al.*, 2018; Mohammad *et al.*, 2018; van Arkel *et al.*, 2018; Ovesy *et al.*, 2022).

The mechanical interaction method of achieving primary fixation has been used to achieve very good pull-out force values in a barbed peg (van Arkel *et al.*, 2018). However, good fixation may lead come at the cost of extensive bone damage if the implant must be retracted due to surgical error, taking bone mass with it as is the case in other implants (Matsen *et al.*, 2008; Geraldes, Hansen and Amis, 2017) and so achieving adequate fixation after reinsertion may prove difficult. Reinsertion is an uncommon but possible outcome during surgery (Rahman, 2022). Whereas conventional frictional forces, generated by an interference fit, may cause damage to the surrounding material during insertion and retraction but this is limited to compressive and abrasive effects.

A further effect that should be considered is that the response of the implant under loading. More specifically, the motion of the implant in relation to the surrounding bone caused by loading, called micromotion (Haïat, Wang and Brunski, 2014; Han *et al.*, 2021; Kohli, Stoddart and Van Arkel, 2021). The magnitude of micromotion can depend on a multitude of factors surrounding the implantation surgery: the quality of the bone mass the implant is inserted into, and the design of the implant itself (Trisi *et al.*, 2009, 2015; Winter, Klein and Karl, 2013; Haïat, Wang and Brunski, 2014; Ellenrieder *et al.*, 2020; Han *et al.*, 2021; Kohli, Stoddart and Van Arkel, 2021).

However, the key element for this thesis is that the magnitude of micromotion an implant experiences can impact the ability of the implant to generate successful secondary fixation, the process of which begins at 6 – 8 weeks postoperatively and for which a general limit of 112μm has been suggested but in some cases a lack of osseointegration has been shown at lower micromotion magnitudes (Jasty *et al.*, 1997; Vandamme *et al.*, 2007; Parithimarkalaignan and Padmanabhan, 2013; Kohli *et al.*, 2018; Kohli, Stoddart and Van Arkel, 2021). Therefore, while design for secondary fixation is beyond the scope of this thesis, the work done herein should not inhibit the future work needed to integrate this design element. Moreover, micromotion is a part of primary fixation and a key link between primary and secondary fixation. It would therefore be useful to evaluate the performance of any implant designed through this work under such conditions, which would in turn require a test rig that was capable of simulating representative loading conditions of a knee. Test machines of this kind exist commercially but are expensive to buy and to customise.

1.13 Simulating knee motion

In addition to micromotion performance of a UKR, bearing dislocation and wear are a concern. Table 1.1 shows aggregated patient data from he United Kingdom registry Reed *et al.* (2024 Table 3.K10), listing the second and third most common reasons for revision surgery of cementless UKRs in this population as bearing dislocation, and bearing wear, after progressive arthritis which is common to both cemented and cementless UKR. Both bearing dislocation and bearing wear are influenced by the loading conditions of the knee, which is also of prime importance in the evaluation of micromotion performance of the joint. Importantly, the OUKR's the bearing is mobile meaning that the position of the load can vary though the range of motion of the knee. However, irrespective of design, polyethylene bearing wear is unavoidable and it can ultimately result in bearing fracture (Pegg *et al.*, 2011), or longer term fixation failure through the initiation of a process called osteolysis (Amstutz *et al.*, 1992). Osteolysis is triggered in response to the accumulation of wear debris and causes resorption of the bone surrounding the metallic components, reducing component fixation.

Fracture of a bearing can be corrected comparatively easily, whereas, a loosened implant requires more extensive revision surgery. The outcome of revision surgery is usually poorer than the primary operation. With a current total knee prosthesis survival of 90% at 10–15 years (Weir, Moran and Pinder, 1996; Font-Rodriguez, Scuderi and Insall, 1997; Sharkey *et al.*, 2002), the number of revision surgeries is projected to increase from 38,300 in 2005 to 268,200 by the year 2030 (Kurtz *et al.*, 2007).

As the most common reasons, after progressive arthritis, for cementless UKR revisions are bearing dislocation and wear (Reed *et al.*, 2024 Table 3.K10), these must be key areas of future research to reduce the anticipated revisions. Therefore, raising implant longevity to prime importance in western populations (Ngai and Wimmer, 2009).

Normal knee function involves both translations and rotations between the femur and tibia (Andriacchi, Stanwyck and Galante, 1986; Lafortune *et al.*, 1992; Walker and Sathasivam, 2000). The predominant motion of the knee is flexion–extension (FE) rotation, with secondary motions defined as anterior–posterior (AP) translation and internal–external (IE) rotation (Dyrby and Andriacchi, 2004). Wear testing can be conducted using displacement-controlled simulators, which aim to mimic these kinematic conditions, under a standardized protocol *BS ISO 14243-3 Implants for surgery – Wear of total knee-joint prostheses – Part 3: Loading and displacement parameters for wear-testing machines with displacement control and corresponding environmental conditions for test (British Standards Institution, 2014)*, developed by the International Organization for Standardization (shortened to *BS ISO 14243-3* in the rest of this thesis). This standard defines the FE, AP, IE and axial (compressive) force patterns during an entire gait cycle as input. Simulators, like the ADL made by AMTI, are capable of operating for millions of cycles, with multiple stations at high speeds (Affatato, 2016). *In vitro* testing allows superior control of loading, while inter-specimen variations that are inherent in cadaveric and *in vivo* testing, are significantly reduced (Werner, Foster and Murray, 1978; Thatcher, Zhou and Walker, 1987; DesJardins *et al.*, 2000). Furthermore, the worn bearing and the wear particulate can be recovered which means in addition to penetration, total volumetric wear can be assessed.

Netter *et al.* (2015) tested wear characteristics of the OUKR UHMWPE bearing according to the *BS ISO 14243-3* (British Standards Institution, 2014) standard in an AMTI knee simulator using both experimental and computational methods, finding both a penetrative wear rate of 0.03mm/year and that tibial component contact surface was responsible for 46% of the total wear.

The *in vivo* wear rate of the mobile bearing in replacement (OUKR) can be found by using radiosterometric analysis (RSA) to measure the gap between the femoral and tibial components. Studies using this approach have shown average penetration rates for the OUKR bearings of 0.022mm/year and 0.070mm/year (Price *et al.*, 2005; Kendrick *et al.*, 2011). Moreover, Horsager *et al.* (2019) used an RSA study to show a relationship between bearing wear rate and overhang; for every millimetre the bearing overhangs the medial margin of the tibial component the wear rate was increased by 0.0147mm/year. Therefore, there is clearly a pressing need to study the bearing wear characteristics of the OUKR, as well as the contribution of displacement effects such as overhang to that wear.

In the study of micromotion accurate loading conditions are critical. Incorrect loading conditions may cause inaccurate interfacial stress-strain states between the implant and bone, the accurate representation of which has been emphasised by Kohli *et al.* (2021) in a recent systematic review. This is because the conclusions of such micromotion studies may be misleading, such as the over production of fibrous tissue in *in vivo* studies (Simmons, Meguid and Pilliar, 2001b, 2001a; Wazen *et al.*, 2013; Kohli, Stoddart and Van Arkel, 2021; Raffa *et al.*, 2021). Therefore it is critical that any machine designed to measure micromotion must be capable of replicating physiologically representative loading for the OUKR such as those in the *BS ISO 14243-3 (British Standards Institution, 2014)* standard.

Moreover, the bearing and its position in loading are critical to how this load is transmitted to the tibial component from the femoral component or *vice versa* and therefore, any machine must simulate the OUKR as a whole joint. Furthermore, any machine with this capability will inherently be capable of subjecting the bearing within that joint to the same loading conditions. If that machine is capable of operating for long periods, then it will necessarily be capable of subjecting that bearing to conditions where it will experience wear. Therefore, it is pragmatic to include both micromotion and wear goals in any design.

Furthermore, during the construction of such a micromotion measuring machine the state of the machine will pass through the state of a wear machine. It is the first step of such a design to first confirm that the machine can accurately follow the motion of a commanded loading profile, with the chosen method of micromotion measurement added after this stage. Therefore, it is again pragmatic to first design a wear simulator capable of applying physiologically relevant loads to OUKR and once that motion system is validated, the add on systems to measure micromotion can be designed, while the machine can then be used to study a clinically relevant problem, bearing wear and dislocation.

Following these points, while this thesis will not directly measure micromotion in the OUKR, it will take as a goal the initial design and validation of a cost effective wear simulator. This wear simulator should be capable of applying physiologically relevant loading conditions, specifically those present in the *BS ISO 14243-3 (British Standards Institution, 2014)* standard, to the OUKR. A design for this wear machine has been started by a group of colleagues but is incomplete and non-functional. This thesis will finish the design and validate the performance of this wear machine. The contributions the author made to this work are discussed in the introduction to Chapter 6. This wear simulator will then be the first stage to a later goal of the design and integration of micromotion measuring equipment that will be left for future studies to undertake.

1.14 Thesis goals

From the literature review in this section, two avenues have established themselves to address elevated revision rates in the cementless OUKR: primarily that there is a need to redesign the fixation geometry of the OUKR tibial component, optimising for primary fixation while retaining the current performance of the keel. This optimisation can be done most efficiently with the development of a suitable computational model; and secondarily that there is a need to complete and validate the design of a cost effective machine to simulate knee motion, so wear may be studied while retaining the possibility of modification for future studies in micromotion. Such a machine has been partially designed but the design needs to be completed and validated in relation to *BS ISO 14243* (British Standards Institution, 2014).

1.15 Thesis objectives

1. To generate a computational model for the insertion of a conventional round nose peg into polyurethane bone analogue foam that is accurate to ±15% across clinically relevant interferences in the prediction of pull-out force. This requires three sub-objectives.

    1.1. To select the optimal material model to simulate primary fixation in polyurethane foam in clinically relevant interferences.

    1.2. To obtain accurate and representative mechanical characterisation data from the polyurethane foam analogue.

    1.3. To use the material characterisation data to optimise the computational model for clinically relevant interferences.

2. To use the generated computational model to produce an optimised peg design for primary fixation.

3. To enable the evaluation of wear of the current OUKR and future primary fixation of novel OUKR designs through the completion of the development of a novel knee wear simulator.

1.16 Thesis scope

The scope of this thesis is split into three sections:

The first, is the development of a finite element model for the prediction of the pull-out force of a peg, which is an analogue of primary fixation. This includes the development of a material model and therefore material characterisation of the polyurethane bone analogue, but is limited to that polyurethane bone analogue and the material properties required to model the plasticity behaviour of that model.

The second, is the development of a new peg design, optimised for primary fixation. This design will attempt to increase the pull-out force of the peg by 10% over a regular round nose peg. This would allow either the same fixation at a lower interference, or greater fixation at the same interference.

Third, the development of a wear machine that could later be developed to allow the limit of secondary fixation, micromotion, to be evaluated. As such the machine will be required to simulation the conventional British standard loading profile (British Standards Institution, 2014) under physiologically relevant conditions.

1.17 Thesis structure

This thesis will answer each of the objectives in a series of chapters, each has been split to focus on one aspect. Those aspects are:

- Chapter 2. Selection of a base material model for the basis of the computational simulation
- Chapter 3. Material characterisation of the polyurethane foams used in this thesis as bone analogue
- Chapter 4. Further development and optimisation of the computational model
- Chapter 5. Will address the design of the fixation geometry using the optimised FEA simulation.
- Chapter 6. Complete the development of a novel knee simulator that would allow a physical simulation of the OUKR under the British Standard knee motion (British Standards Institution, 2014).
- Chapter 7. Will summarise the conclusions of each of the preceding chapters, and highlight the main contributions of this work, as well as some future directions that may prove fruitful if investigated.

Chapter 2 Initial selection of material models

2.1 Introduction

This chapter deals with Objective 1.1, defined in Chapter 1, which states "To select the optimal material model to simulate primary fixation in polyurethane foam in clinically relevant interferences." Therefore this Chapter will evaluate a number of material models mentioned in Chapter 1 with the goal of finding the one or group of models that accurately (<= 15% error) model primary fixation.

Primary fixation of a knee prosthesis is a critical component in allowing long term successful outcomes of a cementless knee replacement. The ability to predict primary fixation *in silico* would greatly aid in the design and evaluation of new cementless components and therefore has been a key area of research in recent decades. A crucial part of the behaviour of the simulated interaction is the material model which is used. In Section 1.10, it was mentioned that there are two predominant ways of approaching the material model in ABAQUS: using a custom user material (VUMAT) as in the work of Ovesy, *et al.* (2020); or using a pre-installed model as in the work of Toal (2013). If possible, it is desirable to use a material model that is already implemented in ABAQUS, as VUMATS are complex to implement and to validate and so should only be used when the standard models are insufficient to capture the material behaviour with sufficient accuracy. Therefore, the objective of this study is to investigate whether material models currently in ABAQUS's library are sufficient to accurately predict the pull-out force of a peg implanted into a polyurethane foam bone analogue.

2.2 Methodology

2.2.1 Mechanical characterisation of the experimental foam

Characterisation of the PCF 20 polyurethane foam (Sawbones, 2022) was conducted at the same strain rate as the insertion test, 10mm/min, to avoid viscoelastic effects impacting the results. To conserve material, small specimens were used, 10mm X 10mm x 10mm the dimensions of each specimen were measured using a vernier calliper (±0.04). The specimen measured area was used in the force to stress conversion.

The compression test was conducted on a Dartek universal mechanical testing machine with a calibrated 2.5kN(±0.025kN) load cell, with data recorded at 250 Hz. The specimens were compressed while vertical force and cross-head displacement data were recorded. Force and displacement data were transformed into engineering stress and strain. From this data, the method used by Szivek, *et al.* (1995) was used to determine the compressive modulus and yield, specifically that the point at which the elastic section of the stress strain curve deviated from linearity was defined as the yield point. This point was determined by aligning a straight edge over the linear elastic section of the curve. ABAQUS (Dassault Systemes, 2020) required both the true stress and true strain, which was gained from the engineering stress and strain data using the conventional logarithmic conversion method.

The ultimate compressive stress was determined from each curve independently, as was the modulus. However, the final curve for the data points put into ABAQUS was generated by averaging the curves from all specimens. This curve is what the reported yield value was derived from as well as the maximum strain, which meant that neither of these values were reported with 95% confidence intervals.

The material modulus was a directly input into the linear elastic, Von-Mises, and Drucker-Prager models; and post-yield behaviour was input into the three plastic hardening models.

2.2.2 Experimental insertion studies

The model was validated against the pull-out forces as this is the minimum force required for extraction of the implant to occur and therefore is the critical design force for primary fixation.

Insertion experiments were performed using additively manufactured titanium pegs, of diameter 5.65mm, on a Dartek universal mechanical testing machine with a calibrated 2.5kN(±0.025kN) load cell.

Previous experiments have shown optimal interference ranges of 0.5mm – 0.7mm (Campi *et al.*, 2018) and 1.3mm – 1.6mm (Berahmani *et al.*, 2015) for cementless primary fixation. Based on these ranges, in this study a target test range of diametrical interferences of 0.4mm – 1.6mm was used, incremented in 0.2mm steps. Each hole was drilled using a precision drill bit and tower drill. Separately, each hole was measured three times for concentricity, using a bore gauge and a calibrated micrometre (±0.004mm).

Each interference was tested three times. The experimental method followed for push-in pull-out tests inserted a 9mm peg at a rate of 10mm/min. This method was modified from previous insertion studies to add dwell time and a slow retract phase in between the insertion and retraction phases (Campi *et al.*, 2018; Mohammad *et al.*, 2018).

2.2.3 Computational model

All material models were applied to a 2D axisymmetric model, built using ABAQUS (Dassault Systemes, 2020) and a custom Python program with the Python API. The peg shown in (Figure 2.1) was an idealization of the peg used in the experiment.

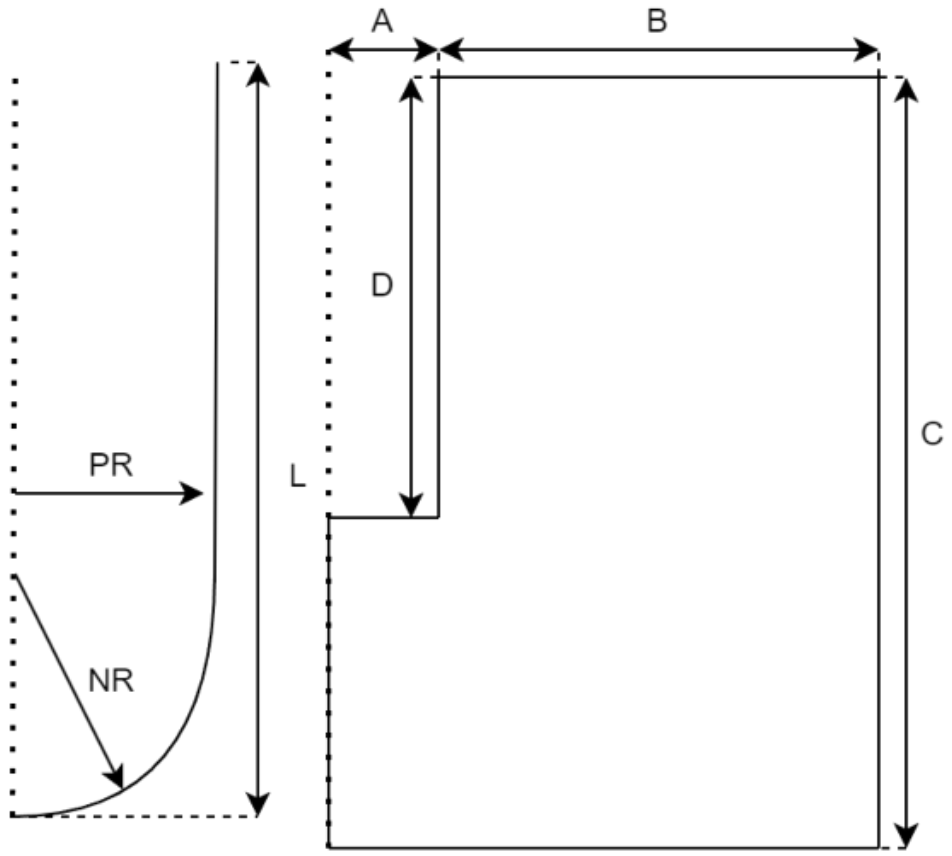

Figure 2.1: (Left): Peg model dimensions, not to scale. PR) Peg radius 2.83mm. NR) Nose radius 2.83. L) Peg length 9.00mm; (Right): Foam model dimensions, not to scale. A) The hole radius, dependent on interference. B) Bulk foam around the hole, 20.00mm. C) The total foam depth, 35.00mm. D) Hole depth, 15.00mm.

From a rest position, on the surface of the foam, the peg was inserted 9mm into the foam model in a smooth step, lasting 0.1s. An explicit formulation was used, including non-linear geometry in the solver.

These simulation parameters were selected to reduce the time taken to solve the model compared with modelling the experiment in real time. As no viscoelastic properties were used, this simplification is unlikely to affect the results.

The hole depth was set at 15mm in both the simulation and experiment, to negate the effect of the stress concentration around the sharp corner on the pull-out force as much as possible. The foam was modelled as a deformable solid with density 320.4kg/m^3 (Sawbones, 2022). A poisons ratio of 0.3 was selected as this is common in similar simulated work (Zivkovic, 2006; Kelly, Harrison, *et al.*, 2013). The diameter of each simulated hole was taken from the average diameter of the holes experimentally tested at each interference.

The peg / foam interaction was defined using penalty friction (Adam and Swain, 2011) using a maximum elastic slip value of 0.005 and the coefficient of friction was taken to be 0.2 (Cordey *et al.*, 1979; Adam and Swain, 2011). Pressure overclosure was defined as hard, and separation was allowed. Boundary conditions were applied to the base of the foam and the central axis where movement was defined as zero in the vertical and radial directions respectively.

The foam model was meshed using CAX4R elements. A mesh convergence study was undertaken. The mesh was defined as converged when: the simulated pull-out force did not vary by more than 5% for the next two element size iterations, similar to the convergence method used by Peg, *et al.* (2013). This resulted in an optimised element size of 1.0mm for all models.

2.2.3.1 Elastic material models

This paper will consider a linear elastic model, and a custom Neo-Hookean hyperelastic model developed using the inbuilt ABAQUS tool (Dassault Systemes, 2020). The parameters for both were taken from the polyurethane mechanical characterisation.

2.2.3.2 Plastic material models

In plastic models the material models considered were: a von-Mises model; and two Drucker-Prager models. All three models were tested under both perfectly plastic and plastic hardening post-yield behaviour. Two sets of Drucker-Prager parameters are presented here; those of Carnelli, *et al.* (2011) and Mullins, *et al.* (2009).

Polyurethane foams are known to have viscoelastic properties. However, this was not considered in this study as the mechanical characterisation was done at the same strain rate as the peg insertion and therefore would likely have little effect on the predicted force.

2.2.3.3 Model specific data

The custom Neo-Hookean model derived from the Sawbones mechanical characterisation is shown in Table 2.1.

Table 2.1: ABAQUS input values for Neo-Hookean Hyperelastic model based on the experimental test data.

Parameter Name	Input
Material Type	Isotropic
Strain energy potential	Neo-Hookean
Input Source	Test Data (true stress / true strain)
Moduli time scale	Long-term
Poisson's ratio	0.5
Strain energy potential order	1

The Drucker-Prager model parameters developed by Mullins, *et al.* (2009) (set 1) and Carnelli, *et al.* (2011), set 1 and 2 respectively, and used by Toal (2013) are shown in Table 2.2.

Table 2.2: Drucker-Prager yield parameters (Mullins, Bruzzi and McHugh, 2009; Carnelli et al., 2011; Toal. V., 2013)

Set	Angle of friction	Flow Stress ratio	Angle of dilation
1	46	1	0
2	25	1	10

A plasticity hardening model was used with data gathered directly from the mechanical characterisation of the polyurethane foam. 100 data points were selected at regular intervals from the post-yield plastic hardening curve and were input into the hardening models.

2.2.3.4 Mesh optimisation

The simulation mesh error was defined as:

$$ME = \left| \left(\left(\frac{PO_{nm}}{PO_{cm}} \right) - 1 \right) * 100 \right| \qquad \text{(Eq. 2.1)}$$

Where ME is the mesh error in percent, PO_{nm} is the simulated pull-out force in newtons of the next smaller mesh to be tested, and PO_{cm} is the simulated pull-out force in newtons of the current test mesh.

2.2.3.5 Definition of the critical zone

As mentioned in Section 2.2.2, Campi, *et al.* (2018) and Berahmani *et al.* (2015) have shown optimal inference ranges for interference fit fixation geometries. However, to find the clinically relevant region, within which the simulation accuracy is most critical, an analysis of the ratio of feature size to interference must be done. The maximum strain experience by hole, caused by the interference fit with the peg, is directly related to the initial and final size of the hole. For Campi *et al.* (2018) an optimal interference range was 0.5mm – 0.7mm for a 3.8mm feature size, a ratio range of 0.132 – 0.184; and for Berahmani *et al.* (2015) an optimal diametral interference range of 1.3mm – 1.6mm for 7.3mm and 7.6mm feature size was shown respectively, a ratio range of 0.178 – 0.211. In the context of a 5.65mm peg, the minimum to maximum range of the ratios (0.132 – 0.211) results in an interference range of 0.7mm – 1.2mm. Allowing for a 0.2mm step, and capturing the lower and upper values, a range of 0.6mm to 1.2mm was selected as the clinically relevant region. This is range where the simulation accuracy is most critical, and will be referred to henceforth as the "critical zone".

2.2.4 Simulation evaluation

The experimental pull-out force was compared with the results from the simulations with model error defined as below:

$$SR = \left(\left(\frac{PO_s}{PO_e}\right) - 1\right) * 100 \qquad \text{(Eq. 2.2)}$$

Where SR is the error of the simulation predicted pull-out force as a percentage, PO_s is the simulated pull-out force in newtons at the current test interference, and PO_e is the corresponding experimental pull-out force in newtons at the current test interference.

The maximum allowable simulation error for the study, and for the critical zone in particular, was set at ±15%. Simulation prediction error upper and lower 95% confidence intervals were calculated from experimental pull-out force confidence interval values.

2.2.5 Statistical evaluation

While no specific statistical significance will be claimed in this Chapter, 95% confidence intervals will be provided, where appropriate, on data values to allow an accurate view of the spread of the data and a loose idea of statistical significance if the two confidence ranges overlap on two different data points. This will also be the case for Chapter 3, Chapter 4, and Chapter 5.

In the comparison of some models an r^2 value is used to evaluate the fit between experimental force values and simulation predicted force values for the peg pull-out, which was produced using the line of best fit function on a graph in Microsoft Excel (Microsoft Corporation, 2021).

2.3 Results

2.3.1 Mechanical characterisation data

All specimens failed in shear (Figure 2.2), the results of the compressive characterisation of the PCF 20 polyurethane foam are shown in Table 2.3.

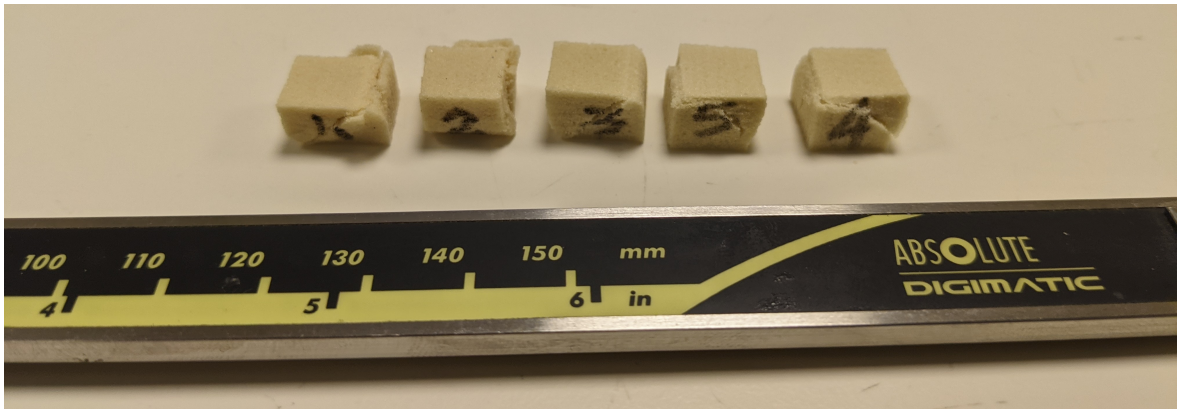

Figure 2.2: An example of five 10 x 10 specimens that failed in shear. Each specimen in this photo was loaded up to 1kN. All specimens failed in the same mode.

Table 2.3: Mechanical properties of Sawbones PCF 20.

Property	Value (±95% CI)
Modulus (MPa)	110.7 (±13.7)
Compressive yield (MPa)	7.4
Ultimate compressive stress (MPa)	9.5 (±0.15)
Maximum strain in test	0.376

The modulus was used in the linear elastic, von-Mises, and Drucker-Prager models. Whereas yield was applied to the plastic models. The ultimate compressive stress was used in the plastic hardening models.

2.3.2 Experimental pull-out force against hole interference

In Figure 2.3 the pull-out force increases to a local maximum of 206.94N at 0.92mm and then decreases again. This patten of behaviour is similar to that seen in previous studies (Campi *et al.*, 2018).

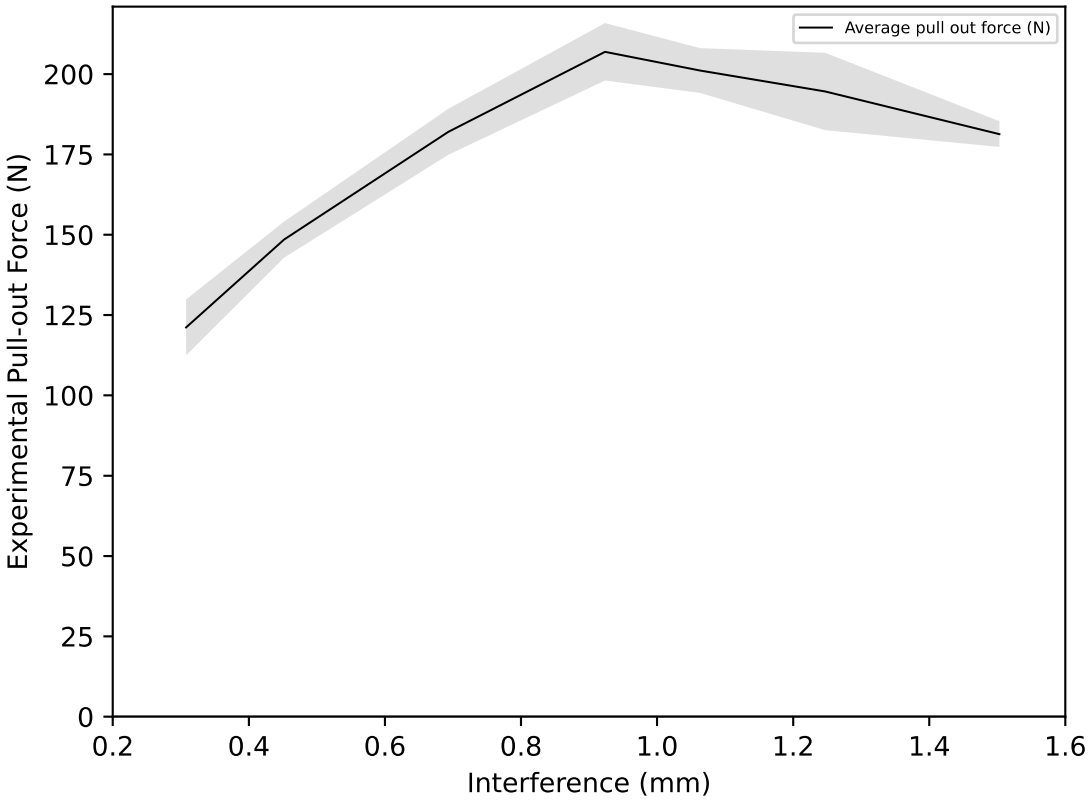

Figure 2.3: Experimental interference against pull-out force.

2.3.3 Elastic models

The elastic models (Figure 2.4) were within the ± 15% of the experimental pull-out forces limit either at the very upper and lower bounds of the interference range tested.

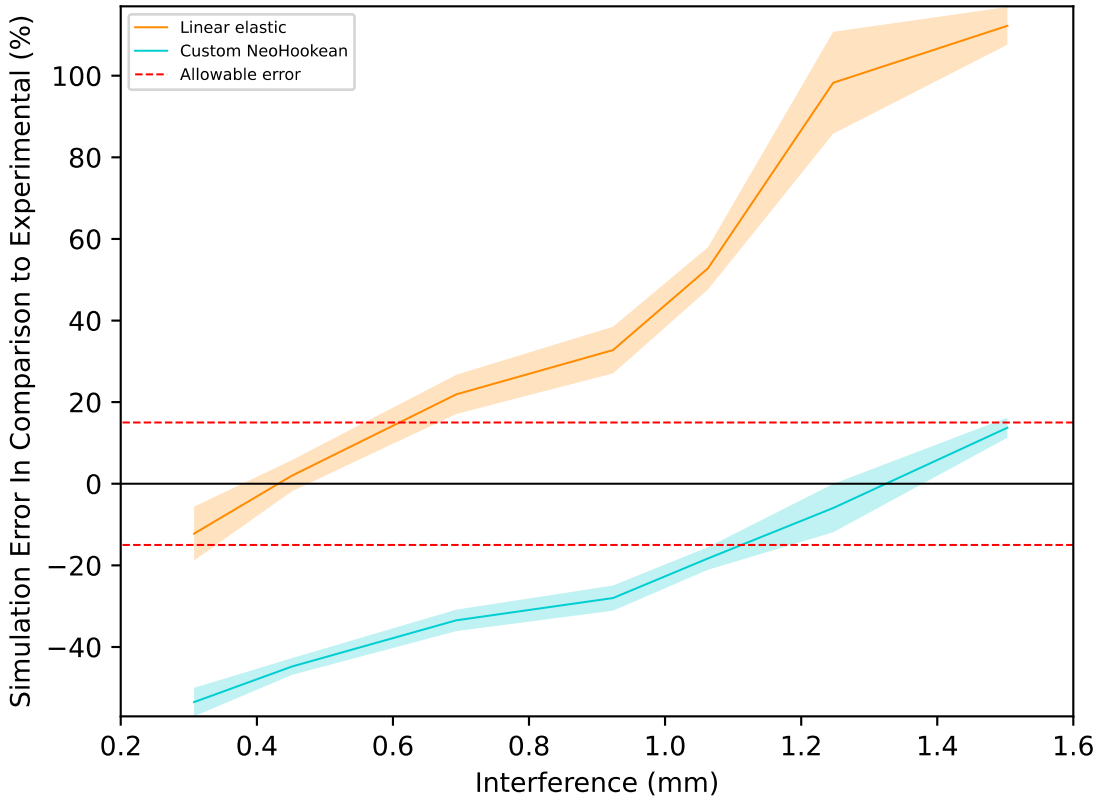

Figure 2.4: Elastic models simulation error plotted against interference. Allowable error bounds are shown in red.

The linear elastic was only able accurately simulate the pull-out force for interferences up to 0.45mm, crossing the allowable error cut off at ~0.6mm interference, the very lower bound of the critical zone. For interference values in the critical zone, the linear elastic model had an error that varied from 21.92% at 0.69mm to 52.79% at 1.06mm, with an average error of 35.82%.

The custom Neo-Hookean model had a similar absolute average error in the critical zone to the linear elastic model at -26.59%, under-predicting the forces in the critical zone of -33.47% at 0.69mm to -21.10% at 1.06mm. The Neo-Hookean model predicted the pull-out force accurately from interferences of 1.25mm upwards.

2.3.4 Perfectly plastic models

Generally, the perfectly plastic models were able to achieve better accuracy than the elastic models in the critical zone (Figure 2.5).

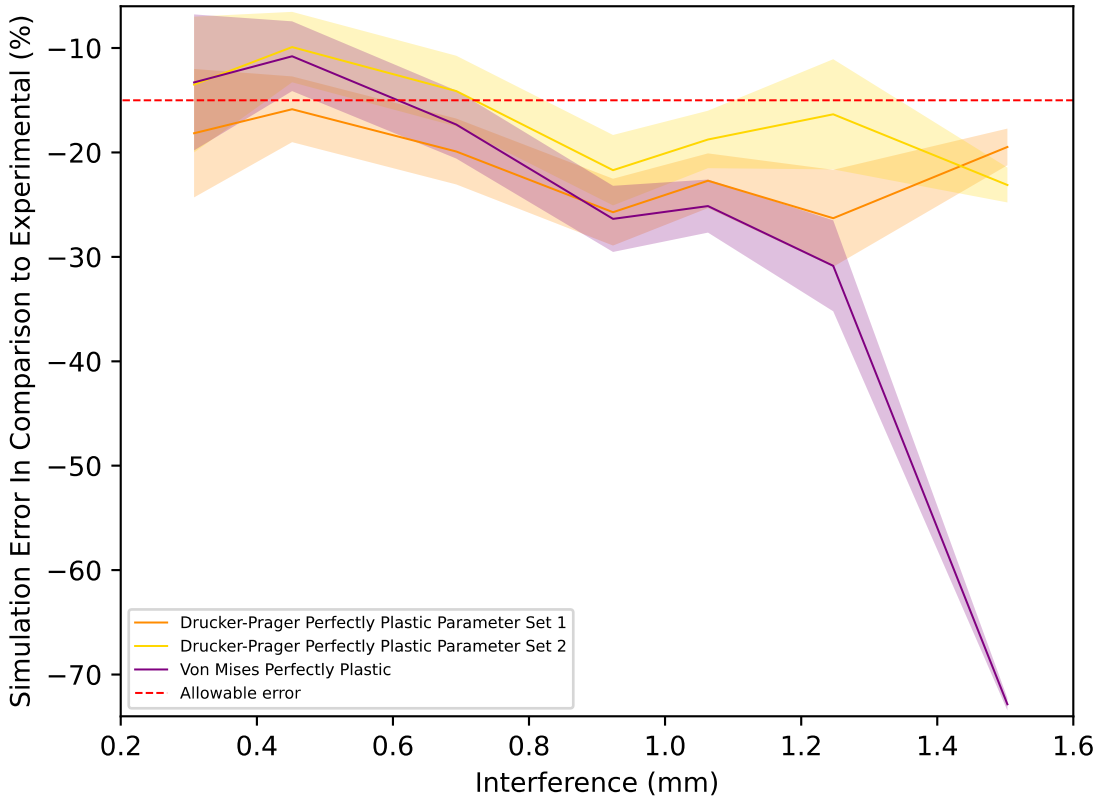

Figure 2.5: Perfectly plastic model simulation errors plotted against interference. Allowable error bounds are also shown.

Both the von-Mises and Drucker-Prager 2 were within the allowable error in the lower band of interferences, up to 0.45mm. The Drucker-Prager 2 model was within the allowable error cut off at 0.69 interference.

The von-Mises perfectly plastic had an error range in the critical zone from -17.33% at 0.69mm to -25.14% at 1.06mm, with an average error of -22.94%. The von-Mises model showed a susceptibility to elements becoming highly deformed (hourglassed) in these simulations. The Drucker-Prager parameter sets 1 and 2 had errors of -23.13 and -10.82% at 0.69mm, -28.90% and -18.28% at 0.92mm, and -25.37% and -15.92% at 1.06mm, respectively. These error values result in average errors in the critical zone of -22.78% and -18.19% for Drucker-Prager parameter sets 1 and 2 respectively. The Von-Mises and Drucker-Prager parameter set 1 behave very similarly with heavy overlap in their 95% confidence intervals.

2.3.5 Plastic hardening models

The plastic hardening models extended the yield behaviour of the perfectly plastic models, allowing an increase of force as the material increased in plastic strain, correspondingly increasing the pull-out force prediction accuracy (Figure 2.6). All three of the models, with the possible exception of Drucker-Prager 1, were within the accuracy cut off in the critical zone. With the von-Mises, Drucker-Prager 1, and Drucker-Prager 2 respectively having an error range in the critical zone from -5.63%, -11.72%, and -4.48% at 0.69mm to -2.44%, -9.91%, and -3.77% at 1.06mm, with an average error of -5.80%, -12.29%, and -5.35%, respectively. Notably the von-Mises and Drucker-Prager 2 hardening models behaved very similarly with substantial overlap in their respective error and 95% confidence interval regions. This was not the case in their perfectly plastic counterparts.

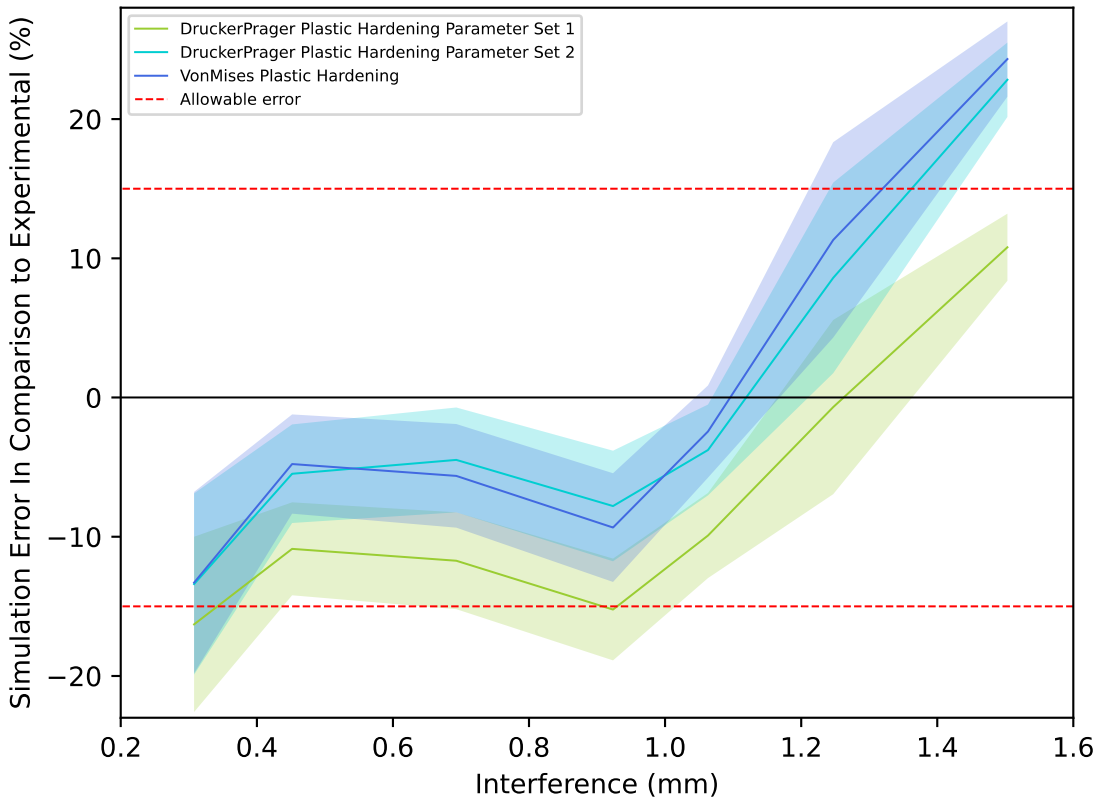

Figure 2.6: Plastic hardening model simulation errors plotted against interference. Allowable error bounds are also shown.

As these models were the most accurate in this study, the predicted pull-out force values were plotted with experimental force for all interferences. This resulted in a line of best fit data as follows: gradient of 1.163, 1.01, and 1.158 and an r^2 value of 0.716, 0.773, and 0.750 for the von-Mises, Drucker-Prager hardening 1 and 2 models, respectively.

2.4 Discussion

The experimental study (Figure 2.3) shows a maximum pull-out force at 0.92mm of interference. As mentioned in Section 2.2.2 and Section 2.2.3.4, other studies have shown an optimum interference at 0.7mm to 0.5mm (Campi *et al.*, 2018) and from 1.6mm to 1.3mm (Berahmani *et al.*, 2015). As each of these studies had different sizes of insertion geometry, a comparison can only be made if the insertion geometry size is taken into account. The ranges then become 0.132 (0.5mm/3.8mm, nominal interference/ nominal keel width) to 0.184 (0.7mm/3.8mm) (Campi *et al.*, 2018), 0.178 (1.3mm/7.3mm, nominal interference/nominal peg diameter) to 0.211 (1.6mm/7.6mm) (Berahmani *et al.*, 2015), from which it can be seen that the ranges of optimal interference overlap. Moreover, the optimal interference from the current study 0.163 (0.92mm/5.65mm, nominal interference/nominal peg diameter) lies within that of Campi *et al.* (2018) and just below the lower range of Berahmani *et al. (2015)*. The difference between the two ranges may be due to the materials present in the studies, Berahmani *et al.*'s (2015) study was conducted in the distal femur and Campi *et al.*'s *(2018)* study was conducted in PCF 20 polyurethane foam. The closeness of the optimal interferences of these two studies is interesting as Campi *et al.* (2018) used a keel design rather than a peg, as was used in Berhamini *et al.*'s (2015) study. It is clear then that at this level of interference, the plastic hardening models were most successful at predicting pull-out forces, meaning that a study of cementless interferences in this range would be required to use a plastic hardening model to achieve acceptable primary fixation prediction accuracy.

The low error of the linear elastic model in the range 0.31mm to 0.45mm (~-13% and ~2% error respectively) suggests that the majority of the material surrounding the hole is in the linear elastic region of the material curve. Whereas, from the next interference value, 0.69mm interference and onwards, the linear elastic model predicted pull-out force increasingly deviates from the experimental pull-out forces. This suggests that plastic material effects begin to dominate between ~0.5mm and ~0.7mm interference, or as a ratio of insertion geometry ~0.088 to ~0.124. This is a higher interference than previous work from Zivkovic, *et al. (2006)*, who stated that 2.0mm interference (0.033 – 0.04 as a ratio) in his model was at the limit of the linear elastic zone, and models with 2.2mm (0.044 – 0.037 as a ratio) interference and higher had elements that exceeded the yield stress of the surrounding bone. It is possible that plasticity only began to dominate in this study not only as a result of the differing materials used but also as a result of the comparatively large elements (1.0mm) arrived at in the mesh convergence. Very high stresses are expected at the surface of an interference fit which drop off rapidly into the body of the material; the current mesh size may not have been able to simulate this rapid stress change.

Elastic model performance indicates that accurate characterisation of both the linear response and plastic response of the material is required in order to obtain accurate pull-out force prediction. Therefore, neither elastic model (linear or Neo-Hookean) is suitable for use in accurate pull-out force prediction of a 5.65mm peg, while simulating interferences in the critical zone of 0.6mm – 1.2mm.

The plastic hardening models improve the accuracy of the simulation of the material behaviour in the post-yield region. Real material does not experience a clean "break point" yield as in the perfectly plastic model. Instead, material failure begins in a small region and propagates through the whole material as loading continues. This behaviour gives rise to a yield region on the material curve, rising from initial yield to the ultimate compressive stress. Necessarily then, a perfectly plastic model will under-predict the forces exerted by the material on the peg while the material is in the plastic region, causing all three perfectly plastic models to decrease in pull-out force prediction accuracy after the onset of plastic behaviour in Figure 2.5.

With the addition of plastic hardening to the three plastic models, an improvement in simulation accuracy was observed. The von-Mises and Drucker-Prager parameter sets 1 and 2, remained within the ±15% cut off window up to and including ~1.2mm interference, therefore, throughout the critical zone. These results indicate that all three models simulated the behaviour of the foam under compression to a far greater degree than their perfectly plastic counterparts. Moreover, all plastic hardening models were comparable to similar insertion studies done by Ovesy, *et al.* (2020) (Fig. 5) using a custom VUMAT model. Ovesy, *et al.* (2020) achieved a similar a similar gradient of 1.063 (1.163 for von-Mises, 1.01 Drucker-Prager parameter set 1, and 1.158 Drucker-Prager parameter set 2) when comparing simulated insertion force results to experimental. However, each model in this study had a wider spread of predicted data when compared to Ovesy, *et el.* (2020) with an r^2 value of 0.95 compared to a range of 0.716 – 0.773 in this study. This comparison demonstrates that when supplied with mechanical data, the pre-installed models in ABAQUS (Dassault Systemes, 2020) are capable of predicting pull-out force with comparable accuracy to models in current literature, albeit with a wider scatter.

Moreover, the 'outlier' results were those that had the largest errors, those above the critical region. Therefore, it is recommended that future studies use the pre-installed plasticity hardening for interferences in the critical region as a starting point as they provide good performance with competitively little development time.

2.4.1 Limitations

The most prevalent limitation was that the mechanical characterisation specimens failed in shear, possibly due to an insufficient specimen aspect ratio. This possibly lead to an under-prediction of both the material yield point and the plastic region used in this study. Future work on mechanical characterisation should follow a standardised compressive testing protocol and should result in more accurate data. Additionally, the logarithmic conversion from engineering stress and strain to true stress and strain is perhaps not suitable for this material due to the volumetric change of a foam during compression. Accurate measurement of this volumetric change during future characterisation studies would help to address this potential source of error.

Additionally simulation time was highly variable across the set tested in this Chapter. There were two main contributions to simulation time, mesh size and post yield behaviour. The elastic models universally ran faster than plastic models equivalents, some 1.0mm meshes completed in under 10 minutes on a AMD 5950X central processing unit (CPU), whilst the plastic models could take roughly 30 minutes on the same settings. At smaller mesh sizes (0.05mm), the plastic hardening models could take upwards of two weeks of computational time on the same CPU.

Furthermore, the maximum increment size in the simulation was 10^{-8} which may have contributed to the longer simulation times as well.

Generally, it seems that the addition of plastic behaviour and plastic hardening behaviour in particular impacts computational time substantially. Furthermore, as of this writing ABAQUS (Dassault Systemes, 2020) explicit 2D axisymmetric simulations do not support graphical processing unit (GPU) acceleration, a common method of speeding up large parallelisable computations, requiring the simulation to be run on the CPU. Therefore, while the simulations in this Chapter arrived at a convergence of 1.0mm, which ran relatively quickly, convergence still took a number of weeks to achieve. Moreover, this effect would pose a large hindrance to obtaining convergence for, and then running a study on, a model which may require a finer mesh to reach convergence.

2.5 Conclusion

All three plastic hardening models tested remained within the allowable limit over the clinically relevant interferences in the critical zone, fulfilling the requirements of the Objective 1.1, and so are recommended as the preferred models for modelling interference fit pegs in future FEA studies. The linear elastic model was capable of accurately simulating the interaction between peg and hole from ~0.3mm to ~0.5mm interference indicating that plastic effects become dominant between ~0.5mm to ~0.7mm interference for a 5.65mm peg. Therefore, the plastic hardening models should be used in future simulation studies, especially in the critical or clinically relevant zone from 0.6mm to 1.2mm interference.

Chapter 3 Mechanical Characterisation of Polyurethane Bone Analogue

3.1 Introduction

This Chapter will deal with Objective 1.2 defined in Chapter 1, which is stated as "To obtain accurate and representative mechanical characterisation data from the polyurethane foam analogue." This Chapter will focus on the accurate characterisation of the polyurethane foam bone analogues that are used in this thesis to evaluate the relative primary fixation of the 5.7mm diameter pegs.

Polyurethane (PU) foam has a long history of being used as a trabecular bone analogue (Szivek, Thomas and Benjamin, 1993; Kelly and McGarry, 2012; Campi *et al.*, 2018), during which time much work has been done on attaining the basic mechanical properties of the polyurethane foams notably by Szivek, *et al.* (1993), Szivek, *et al.* (1995), Thompson, *et al.* (2003), Calvert, *et al.* (2010), and Kelly, *et al.* (2012). The ASTM standard (American Society for Testing and Materials, 2008) for ridged polyurethane foam was introduced to provide a standard set of physical and mechanical properties of PU foams for testing orthopaedic devices and instruments, discretised by apparent density. Much of the current use of PU foams has relied on PCF 20 grade (Sawbones, 2022). However, other densities of PU foam are available from Sawbones. The density of a foam has an impact on the expressed mechanical behaviour of the foam and thus would be expected to also have an impact on how orthopaedic devices behave both during and after insert into that foam. Therefore, mechanical characterisation of these PU foams is very important for future development of orthopaedic devices as design attitudes move towards a more subject specific approach.

In Section 1.11 a number of equations were presented for the behaviour of foams under altering density radios (Equations 1.4, 1.5, and 1.6) these equations are all for open cell foams. The closed cell foam equations have the added complexity of taking into account fraction of solid in the cell edge (ϕ), which correspondingly also introduces a material specific parameter which requires further study to characterise.

If it is possible to model these foams as open cell foams, it would be beneficial to do so to reduce the amount of characterisation needed to accurately predict material properties at altering density ratios. In previous work, Thompson, *et al.* (2003) used the open cell equation forms and allowed both coefficient and the power to alter in the fitting process and Calvert, *et al.* (2010) used the closed cell version of the equations previously presented. This study will take an slightly different tack. The equations will be fitted in their current form with only the coefficient allowed to vary as a material parameter. The equations used are for open cell foams which might present a challenge to accuracy. The manufacture mentions these are closed cell foams (Sawbones, 2022), but the equation for open cell foams contains fewer material unknowns, specifically the fraction of solid in the edges of the cells or ϕ.

Each of these material specific coefficients are useful in predicting the mechanical response of foams via their apparent density and therefore, this chapter will determine these material coefficients for ridged polyurethane by characterizing the mechanical compressive behaviour of these of varying densities for use with orthopaedic implants.

3.2 Methodology

The specimens were prepared and were tested in accordance with *BS ISO 844:2021* (British Standards Institution, 2021). The data was processed following the algorithm recommended in the standard. The engineering strain was converted into true strain using the conventional logarithmic method.

3.2.1 Material tests

Material characterisation was conducted using method A from *BS ISO 844:2021* (British Standards Institution, 2021). The compression tests were carried out using a 50kN(±0.5kN) INSTRON universal materials testing machine. Each density, PCF 12, 15, 20, and 25 was compressed at 10mm/min to characterise the material response. Six specimens each of dimensions 50mm x 50mm x 20mm were created for each foam. Each specimen was compressed and the force recorded and each specimen was measured along each axis at two different locations with a precision UKAS calibrated vernier calliper (±0.012mm). Each specimen was smeared on both top and bottom faces with petroleum jelly to reduce the interfacial friction that can lead to specimen barrelling. Due to the lack of accurate digital image correlation (DIC) equipment, limited space between the compression plates, and the high degree of final compression, ~70%, cross-head displacement was used rather than an extensometer to measure strain. The experimental setup is shown in Figure 3.1.

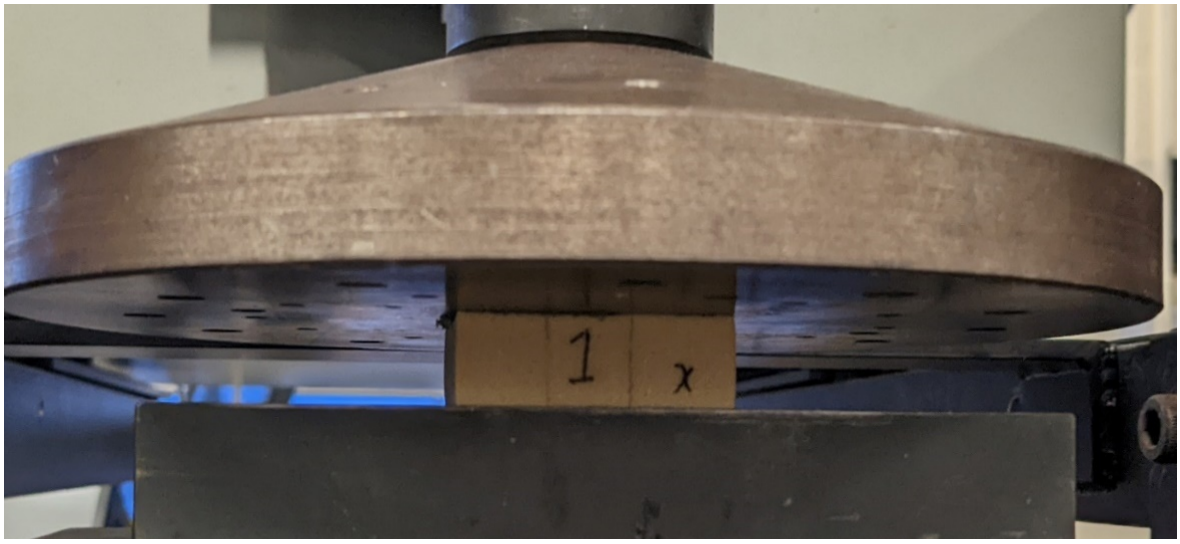

Figure 3.1: Material in between the two compression plates before compression.

The PCF 20 data was done in a single experiment soon after cutting as were two from each of the other foams (PCF 12, 15, and 25). However, the remaining specimens of PCF 12, 15, and 25 were not able to be tested in that sitting due to a limitation on the availability on the test technician. The next available slot was on a the same make of machine, calibrated to the same quality and error, at a separate testing facility many months later. This gave the foam specimens the time to age which can cause the mechanical properties to alter outside of their usual values (Yarahmadi, Vega and Jakubowicz, 2017; Da Silva *et al.*, 2023). This meant that when the results were calculated following the second round of tests the two groups of results were clumped at different locations. Moreover, the second round of results shifted the average so much that it was outside the 95% CI calculated from the first tests. The peg experiments of Chapter 4 were conducted on fresh foam specimens for the PCF 12, 15, and 25 data and the first round of experiments represented this condition of foam better. Therefore, the second round of tests was removed from the data set presented here and used in the subsequent Chapters.

Due to this, only two specimens were included in the data sets for the PCF 12, 15, and 15 foams which poses a problem for the meaning of the 95% CI presented with these foams. Following conventional understanding a minimum number of three specimens is needed for this value to be meaningful. The 95% CI value is included with averages of PCF 12, 15, and 25 for completeness but this limitation should be born in mind when interpreting the results of this study.

3.2.2 Material data processing

The raw data text files were read into a custom MATLAB program (MathWorks, 2020). The specimen dimensions were used to calculate the engineering stress and strain of the specimen. The ultimate compressive stress (UCS) defined as the next inflection point reached after the inflection point caused by compressive yield. The UCS was used to find the material modulus as described in Annex A – A.5 *BS ISO 844:2021* (British Standards Institution, 2021). A representation of the process is shown in Figure 3.2 where the UCS is shown as a red line.

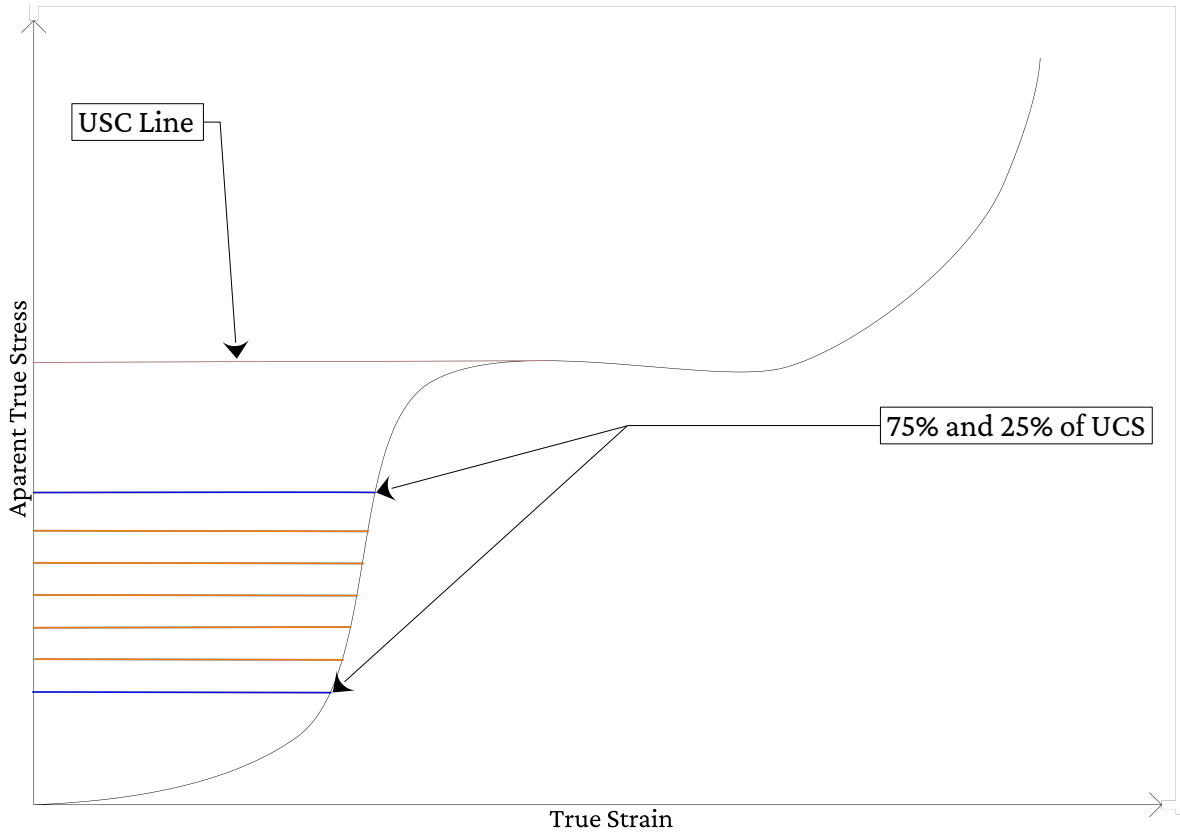

Figure 3.2: A representation of a foam material curve, with the designations shown for the UCS, 75% and 25% of the UCS, and the six sections in-between.

Two lines were drawn at 75% and 25% of the UCS, shown as blue lines in Figure 3.2. The difference between those two values was split into six equal parts. The divisions are shown as orange lines in Figure 3.2. For each of the six sections a line of best fit was created for the stress and strain values and the gradient of that line evaluated, shown as pink lines in Figure 3.3.

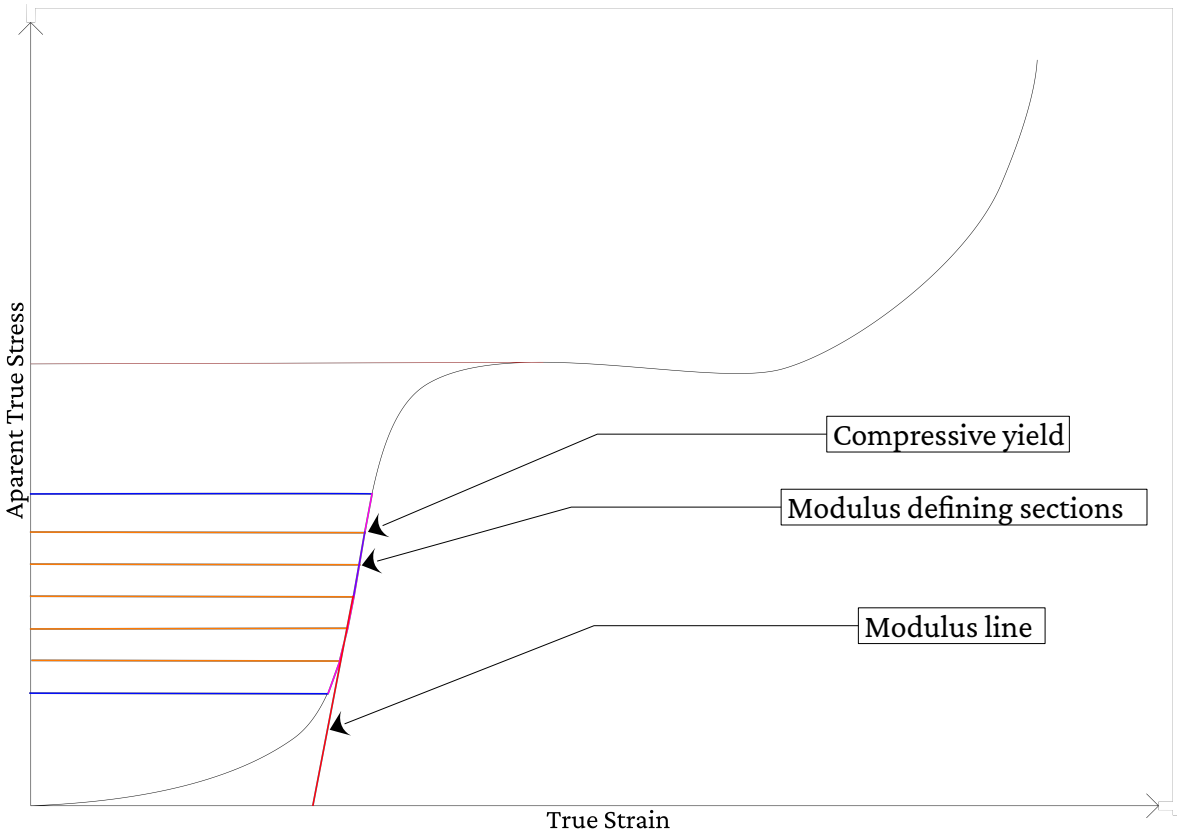

Figure 3.3: A representation of a foam material curve, with the lines of best fit in each of the six sections, and the defined modulus taken back to the strain axis.

Gradients were averaged in two section pairs, 1+2, 2+3, etc. These averaged gradients were compared, and the highest two section average gradient was defined as the youngs modulus of that foam, shown as a deep purple line between the upper sections in Figure 3.3. The compressive yield stress was defined as the immediate next point on the material curve after the steepest linear section used in the modulus calculation, similarly to Szivek, *et al.* (1995) and Thompson, *et al. (2003)*.

Once the material modulus and compressive yield point were determined, a straight line was drawn from the yield to the zero-stress using the specimen modulus, shown as a red line in Figure 3.3; the resulting strain offset being used to correct the curve so the material curve originated from the origin (Figure 3.5) as in *BS ISO 844:2021* (British Standards Institution, 2021). From these corrected curves an average more generally representative material curve was obtained.

3.2.3 Calculation of material coefficients

The calculation of the material coefficients (C_1, C_4, and C_5) required the solid density to be known, which was taken as 1.20g/cm^3 (Roff and Scott, 1971; Gibson and Ashby, 1997) which correlated well with other literature values of 1.25g/cm^3 (Biedermann *et al.*, 2001) and 1.19g/cm^3 (Gong, Kyriakides and Jang, 2005).

Further, the solid Young's Modulus was required which was taken as 1.60GPa (Finnie and Patel, 1970; Gibson and Ashby, 1997). The apparent density was taken from the grade of foam, i.e. 12PCF = 0.192g/cm^3, 15PCF = 0.240g/cm^3, 20PCF = 0.320g/cm^3, and 25PCF = 0.400g/cm^3 (American Society for Testing and Materials, 2008).

From these values each data point was calculated from the foam compressive properties described earlier. The expected coefficient values were calculated from each data point which in turn were averaged and used to calculate and upper and lower 95% confidence interval for each coefficient value. As the true coefficient values are expected to lie within this region, the most predictive value was sought using a custom Python script. This script was used to test values from the lower 95% confidence interval to the upper 95% confidence interval. Each value was then used to predict the corresponding ratio (M_r, E_{yr}, P_{yr}, etc) at each density point and then this predicted data set was tested against the experimental data set to measure the r^2 value. The coefficient in this range with the best r^2 value, having the best fit, was selected as the value to be reported.

3.2.4 Statistical evaluation

Unlike Chapter 2, where r^2 values were used in this Chapter, they were calculated using the custom Python script with the Scikit-Learn module (*scikit-learn*, 2025).

3.3 Results

Following the material data methodology, each specimen was tested and the results recorded in force time data. This raw data is shown in Figure 3.4.

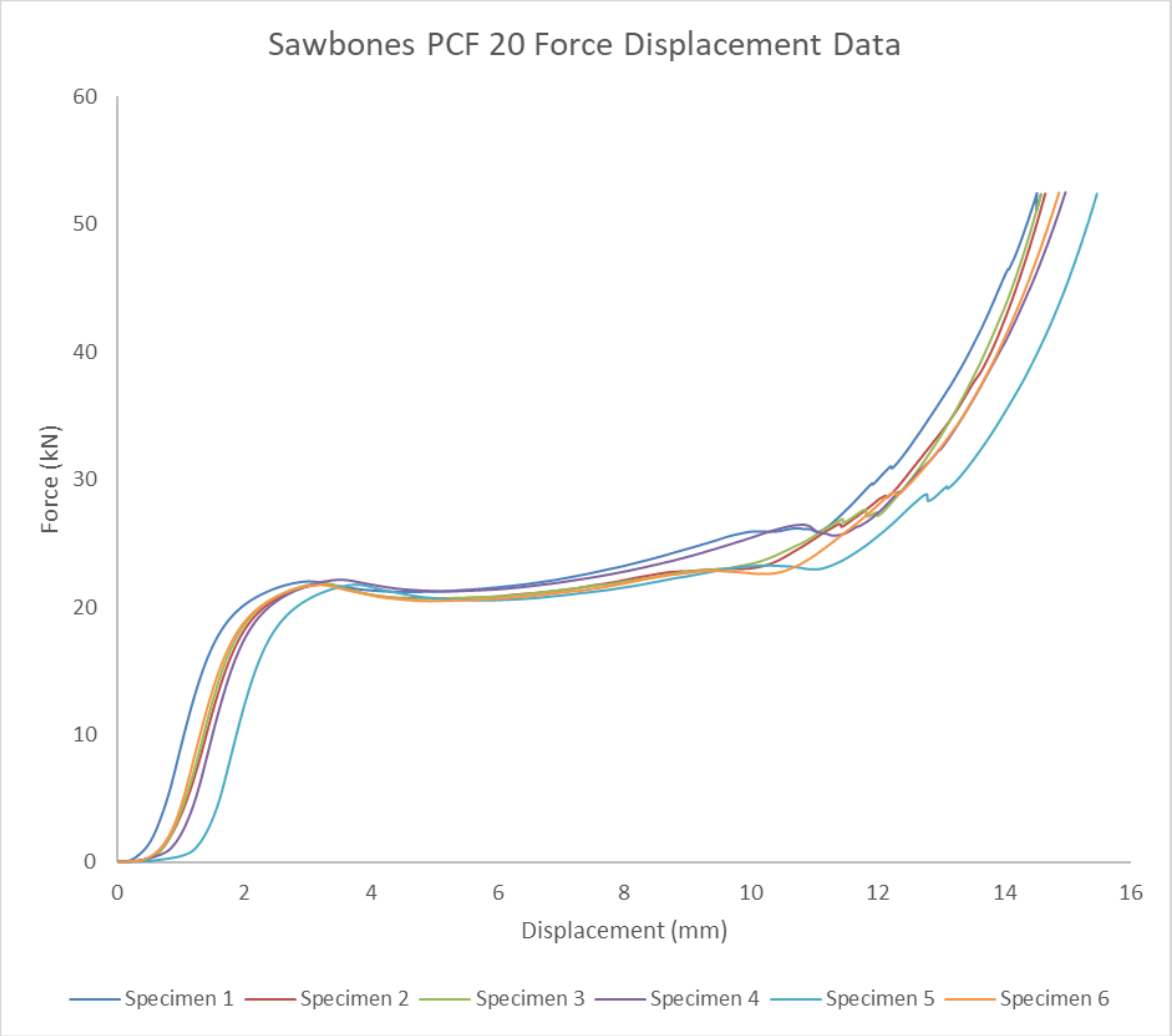

Figure 3.4: Sawbones PCF 20 displacement force raw data.

There is, however, variability in the displacement of each specimen which is due to a ramp up feature at the origin of each curve.

This ramp up feature obscures the initial part of the linear elastic zone which is shown more clearly in Figure 3.5, after the data has been processed. The data was processed using a custom MATLAB (MathWorks, 2020) program which used a custom implementation of the algorithm described in Annex A – A.5 *BS ISO 844:2021* (British Standards Institution, 2021) and the logarithmic engineering stress to true stress conversion, to obtain an apparent true stress curve. During this process, the ramp up feature was removed and the individual curves were averaged, allowing one curve per density to be produced. This average curve was turned into a true stress strain curves shown in Figure 3.5.

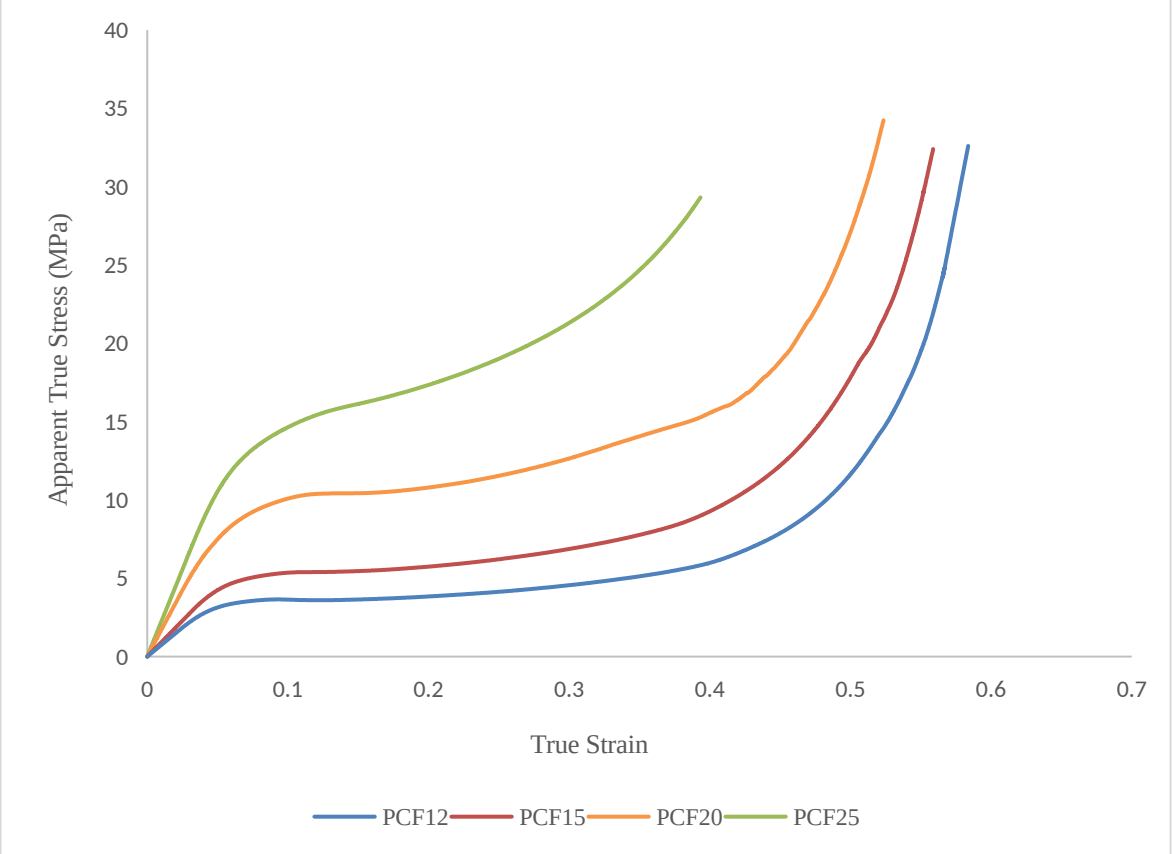

Figure 3.5: Apparent true stress strain curves for PCF 12, PCF 15, PCF 20, and PCF 25 foams.

In broad overview, the modulus, compressive yield stress, and ultimate compressive stress all increase with increasing density. Whereas the plastic strain before consolidation decreases with increasing density. The values of which are shown in Table 3.1.

Table 3.1: Mechanical properties of the foams in relation to density.

ASTM Classification	Density ratio (ρ_r)	Modulus (±95%CI) (MPa)	Compressive Yield Stress (±95%CI) (MPa)	Ultimate Compressive Stress (±95%CI) (MPa)
PCF 12	0.160	73.8 (±2.5)	1.9 (±0.2)	3.6 (±0.02)
PCF 15	0.200	91.4 (±1.7)	3.2 (±0.04)	5.4 (±0.04)
PCF 20	0.267	169.4 (±4.8)	4.1 (±0.3)	10.4 (±0.1)
PCF 25	0.334	222.2 (±1.1)	7.2 (±0.4)	16.5 (±0.5)

The pattern pointed to in Figure 3.6 is more apparent with the numerical values in Table 3.1. All three properties increase with density. This relationship is more easily understandable when presented as a ratio in Equations 1.4, 1.5, and 1.6 which has been plotted for each property in Figure's 3.6, 3.7, and 3.8 respectively.

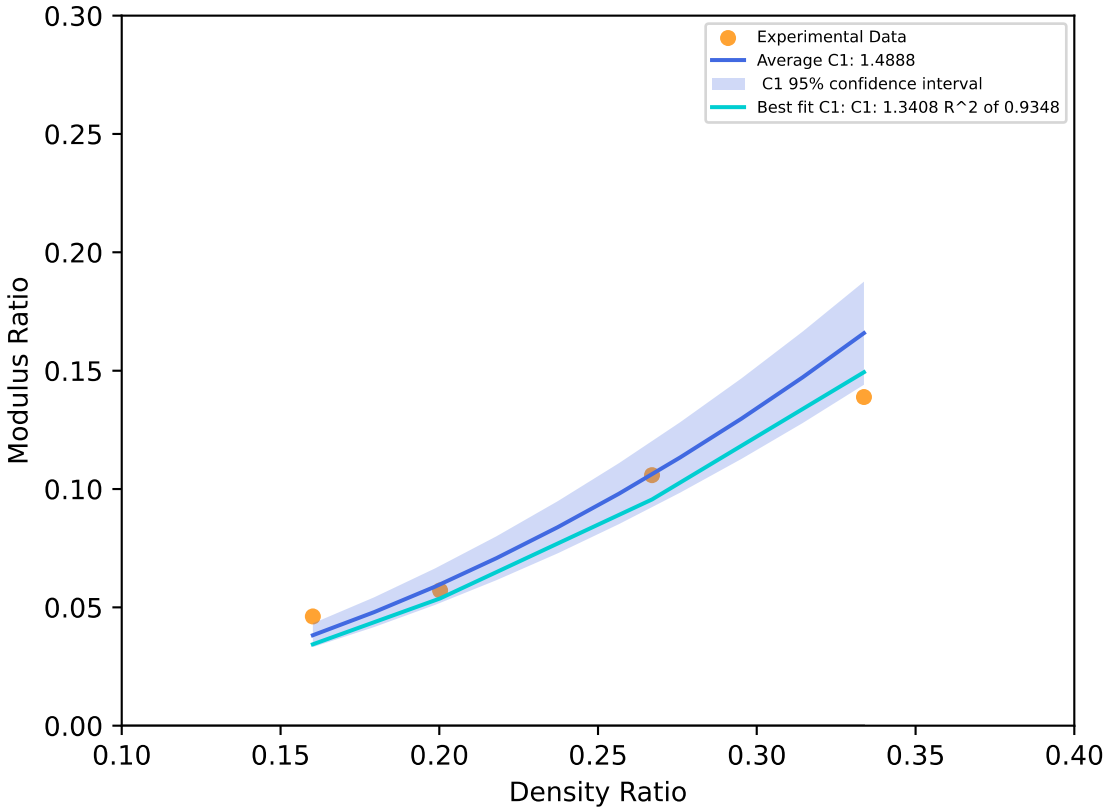

Figure 3.6: Foam density ratio against modulus ratio, plotted with a $C_1 X^2$ line of best fit.

The modulus ratio is plotted against foam density ratio, with a C_1 coefficient of 1.341, and a value of 0.935 for a parabolic line of best fit corresponding to Equation 1.4. The average calculated from the raw data, 1.489, is greater than the C_1 that gives the best value.

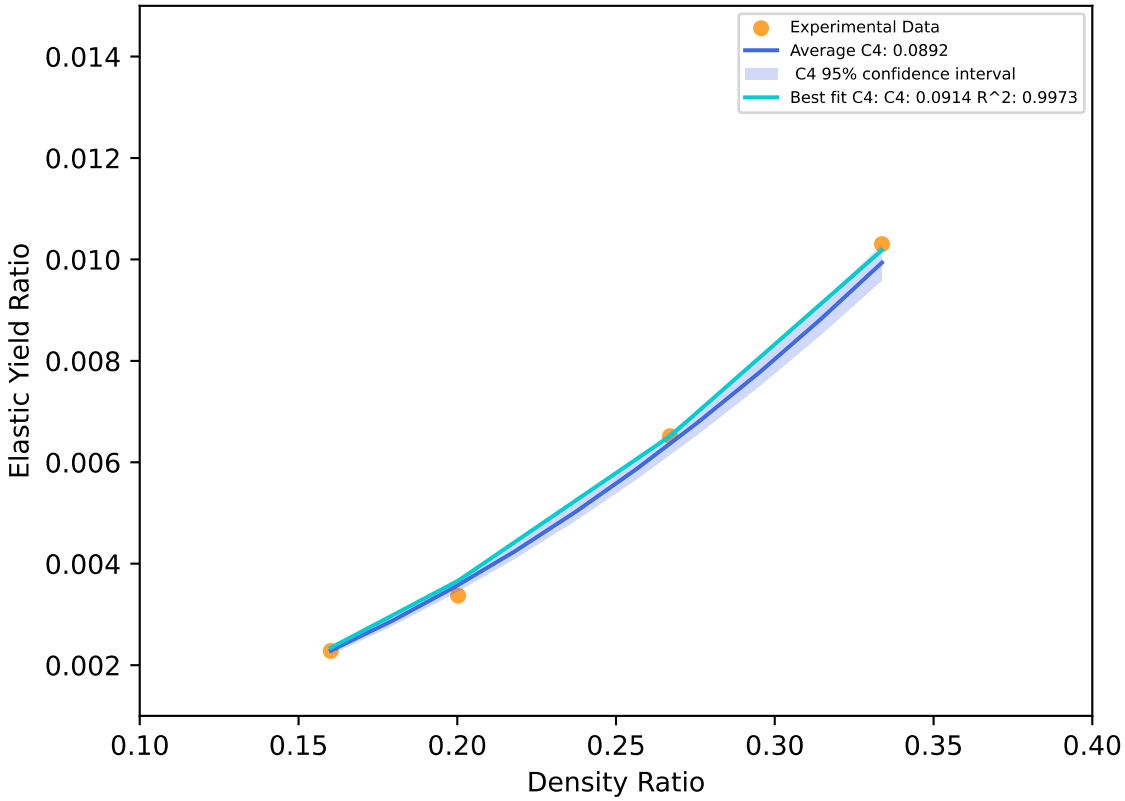

Figure 3.7: Density ratio against elastic yield ratio, plotted with a C_4X^2 line of best fit.

Elastic yield ratio is plotted against the density ratio. The value of C_4 from the parabolic line of best fit, Equation 1.5, is 0.091 with a value of 0.997. The average C_4 is 0.089 which is closer to the upper 95% confidence interval of the experimentally calculated C_4 range.

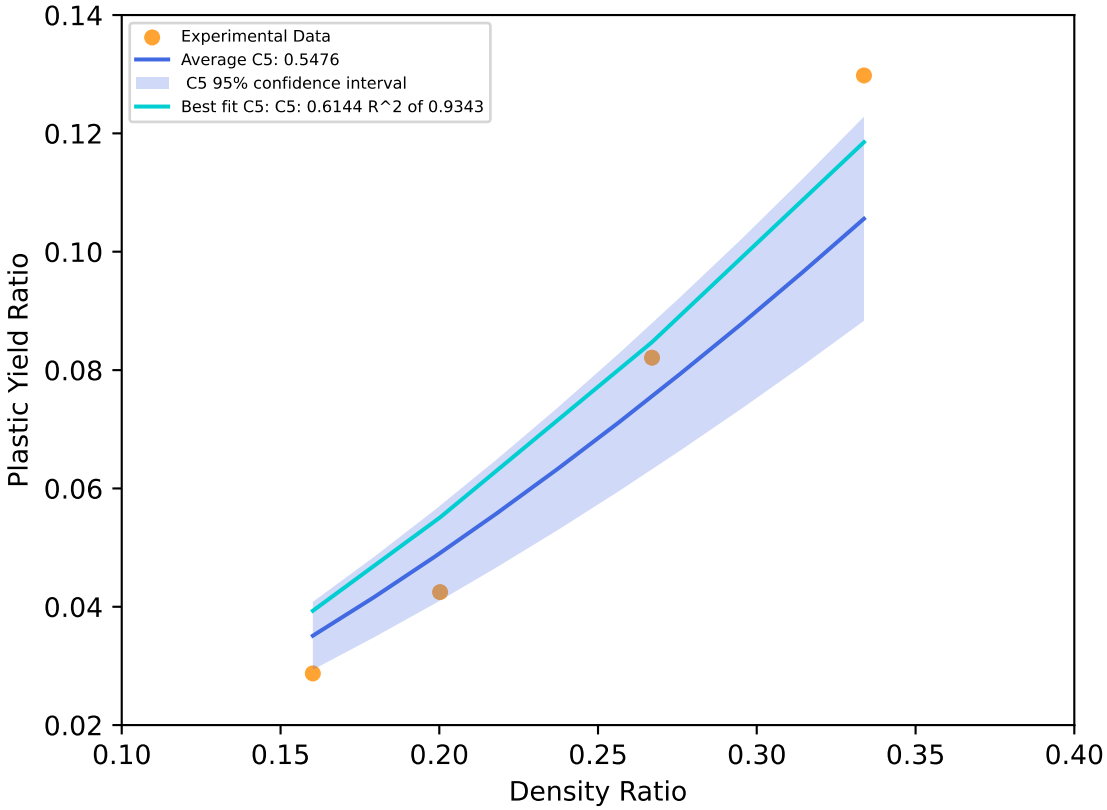

Figure 3.8: Density ratio against plastic yield ratio, plotted with a $C_5 X^{\frac{3}{2}}$ line of best fit.

Plastic yield ratio is plotted against the density ratio. The value of C_5 from the power line of best fit, Equation 1.6, is 0.614 with an r^2 value of 0.934. The average C_5 is 0.548 which is closer to the upper 95% confidence interval of the experimentally calculated C_5 range.

Table 3.2: Specimen density and elastic-plastic criterion.

ASTM Classification	Density ratio (ρ_r)	Elastic-Plastic Crossover Value (Eq. 1.7)	Elastic (True) Plastic (False)
PCF12	0.160	0.227	True
PCF15	0.200		True
PCF20	0.267		False
PCF25	0.334		False

Half of the specimens in Table 3.2 are on each side of the elastic-plastic criterion in Equation 1.7. The lower density foams are considered dominated by elastic bending, and the higher density foams are considered dominated by plastic yielding.

3.4 Discussion

Elastic-plastic foams compress in three distinctive macro stages: Linear elastic; Plateau; and Densification as described by Gibson and Ashby (1997, p. 177 Fig 5.1 (b)) and visible in Figure 3.4. However, there are a couple of extra features in the graph which had an impact on the processing of the data, notably the initial ramp up to the linear section.

The ramp feature is likely produced by manufacturing inaccuracies which result in each specimen having a slightly trapezoidal shape, causing the lowering platen to impinge on a small area first, slowly bringing the total specimen surface area into contact with the platen. The force then increases as the cell walls continue to strain going into the linear elastic phase of the curve, leading into the plateau phase, which is characterised by pseudo-plastic yielding. The mechanism of failure is dependent on foam morphology; thin strut like morphologies fail in buckling while more structurally stable morphologies fail by crushing (Gibson and Ashby, 1997).

At the point of cell wall failure, the increase in force begins to deviate from linear. However, this is a gradual process; an ever-greater proportion of the foam under load transitions to failure, resulting in the force increasing with displacement with ever diminishing gradient. The maximal point is the materials' ultimate compressive stress, and the beginning of the plateau phase. In the plateau phase most of the material has entered failure, the material being compressed further causing an approximately "perfectly plastic" region as the cell volume is compressed. This region continues until the cells start to become completely compressed and begin to consolidate, resulting in a rapidly increasing force resisting compression as the material increasingly behaves as a solid.

The behaviour of the foam in the plateau phase makes calculation of the true stress curve without some areal compensation method, such as DIC, very challenging. As such a method was not available to this study; an "apparent" true stress curve is presented in place of a measured true stress curve. It is important to note at this point that the location of deviation between the apparent and actual true stress curves will begin at material yield and the error will increase as strain increases. However, an estimate of the true stress can be provided by bounding of the actual curve using the engineering stress and apparent true stress curves, as the actual true stress curve will lie in-between the apparent true stress curve and the engineering stress curve. It is for this reason that no data beyond the ultimate compressive stress is presented herein. This difficulty is further raised by the reality that in the finite element literature on the simulation of polyurethane foam compression, material behaviour is simulated using either the engineering stress (Kelly, Harrison, *et al.*, 2013) or is similarly calculated using the logarithmic conversion (Schulze *et al.*, 2019).

Therefore, while in a theoretical framework this inaccuracy presents challenges, in practical terms, mitigation has been demonstrated as these models still achieve good accuracy with relation to their experimental comparisons.

In comparison to other work PCF 20 in Table 3.1 is shown to have a modulus of 169.4MPa ± 4.8MPa 95% CI comparable to the 164MPa ± 27.8MPa grade 320 (Thompson *et al.*, 2003), 195MPa ± 32MPa and 216MPa ± 17MPa for 3720 grade and 195MPa ± 53MPa and 206MPa ± 12MPa for 6720 grade (the two results for each foam type come from difference machines) (Calvert *et al.*, 2010), and 141.3MPa ± 40.9MPa for grade 20 Sawbones (Kelly and McGarry, 2012). These data show both that the modulus presented in this work for PCF 20 is within the range of values of previous literature and that the material properties of PU can be very variable notably falling outside the range presented in the ASTM standard of 167.5MPa – 257.5MPa (American Society for Testing and Materials, 2008), which may point to a difficulty in grouping these foams solely by apparent density as the current standard does. This pattern is further confirmed by PCF 15 from Table 3.1 having a modulus of 91.4MPa ± 1.7MPa 95%CI compared to 115MPa ± 17MPa and 134MPa ± 9MPa for 3715 grade (Calvert *et al.*, 2010) and PCF 12 with a modulus of 73.8MPa ± 2.5MPa 95% CI compared to 79MPa ± 7.5MPa for grade 200 (Thompson *et al.*, 2003).

However, this pattern of data falling outside the standard range is again repeated with the ultimate compressive stress presented for PCF 20 4.1MPa ± 0.3MPa for this paper and 5.14MPa ± 0.15MPa for grade 320 (Thompson *et al.*, 2003), 8.4MPa ± 0.1MPa and 8.5MPa ± 0.3MPa for grade 3720 (Calvert *et al.*, 2010), and 3.8MPa ± 0.7MPa for PCF 20 Sawbones (Kelly, Harrison, *et al.*, 2013). Additionally, the standard deviations are notably tighter for these values, meaning that the values in this paper and others do not overlap in range. However, for foams other than PCF 20, this should not be taken as indicating significance due to the lack of specimens in these foam data sets.

What these two points mean in the context of testing orthopaedic implants is twofold: firstly, it is highly advisable for a user to test the properties of the batch of PU foam before testing the implants in it; and secondly, that comparing absolute values of insertion forces across different batches of foam could present a challenge in meaningful interpretation of the data. This leads to the conclusion that the implants being compared should likely be tested in the same batch of PU foam so a meaningful relation between the experimental data produced by each implant can be established. Further to this, as PU foams and their additives are further studies it may become beneficial to establish further criteria for the disambiguation of foam grades in the standard specification.

In Figures 3.6, 3.7, and 3.8 the coefficients for C_1, C_4, and C_5 are given respectively. The values expected from "Cellular Solids" (Gibson and Ashby, 1997) for these are $C_1 \approx 1.000$, $C_4 \approx 0.050$, and $C_5 \approx 0.300$. In the case of C_1 Gibson and Ashby (1997) provide an explanation for foams that have a value greater than 1.000, primarily that the value "includes all of the geometric constants of proportionality" (Gibson and Ashby, 1997, p. 186), as is true for C_4 and C_5, therefore, being correlated to the bending resistance of the internal structure of the foam.

Following from this, a value greater than that expected represents a structure that is more resistant to bending than the assumed open foam structure in equation. The larger value may in part be due to the elastic plastic condition, shown in Table 3.2, straddling the midpoint of the specimens, which would may intern lead to the conclusion that the lower densities, and hence the "more elastic" specimens, should be associated with C_1 values closer to the expected value of 1.000. However, the inverse is the case, larger C_1 values are associated with the most elastic specimens. The results presented suggest that these foams may require the added complexities of the closed cell foam equations at densities greater than PCF 15.

The argument for this is that the elastic failure limit is earlier than the plastic failure limit, and as such is more susceptible to the additional rigidity that the closed pocket of gas affords, MPa compared to kPa. While the plastic failure of the cell wall is a process that happens at a much higher pressure than that typically seen in contained volumes and as such, the foam returning to more conventional C_1 values is expected.

The behaviour of C_4 and C_5 do not follow an expected pattern; the trend is inverse to that of C_1, both increasing in error of prediction as the density increases. It would be expected that the elastic yield (Equation 1.5) would predict the densities below the elastic-plastic criterion cut-off value (Equation 1.7) better than the plastic yield (Equation 1.6). Correspondingly, it would also be expected that the plastic yield would predict the yield ratio more accurately at higher densities creating a crossover halfway through the dataset. This is also not the case. The relative error on the prediction from the line of best fit is larger for the plastic yield (~205% from 0.300 to 0.614) than the elastic yield (~183% from 0.050 to 0.091) throughout.

It should be stated that both of these values are already large. However, there is a ~20% reduction in the elastic yield coefficient in relation to the plastic coefficient. As might be expected, the foams in this study behave as closed cell foams, but the reduced error of the elastic prediction suggests that there might be insufficient material density to contribute meaningfully to the plastic failure mechanisms and, as such maybe more predictable by the elastic yield (Equation 1.5). This is interesting as it further suggests that there is a region at the boarder of the elastic plastic criterion that behaves in a more complex way, analogous to the advanced buckling region between the compressive yield and Euler buckling region of the buckling curve and, therefore may be a path open to further research.

While these foams can be modelled by using the simplified open-cell foam versions of the equations in the range PCF 12 – PCF 25 using the coefficients that have been established, the variation of these coefficients suggests that it may beneficial to use the full closed-cell foam equations for more accuracy, and a more detailed understanding of the foams behaviour with relation to density variation. It was not possible for the author to establish the value of ϕ in this study, but if this value can be reliably established for the foams in this study (Sawbones PCF 12 – PCF 25) then the coefficients C_1, C_4, and C_5 could be established for the closed-cell equations. As the ratio of material in the cell walls to cell faces, ϕ, is defined as the concentration of cell material away from the surfaces of the cell faces towards the "corners" of the cell, assuming predominantly circular cells, a study of ϕ may be made using micrographs of a polished specimen and a program such as ImageJ2 (Rueden *et al.*, 2017), where a threshold could be set turning the micrograph into a black and white image allowing the cells and walls to be seen easily.

A measurement of the black cell walls as an areal fraction of the image should be taken, then each cell could be selected and a circle drawn from the centre of each cell to the outer minimum outer diameter of the cell wall for its minimum thickness. Then a boolean subtraction of that circle away from the black image could be done. When that has been done for each cell, the remaining black image could be measured again as an areal density ratio. The before and after areal density ratios could then be divided against each other to give the ratio of cell material concentrated in the cell edges. A similar process could be followed for faceted cells where parallel lines are drawn to the flat inner cell wall and touching the minimum face thickness. Both of these suggested methods are very time intensive, but may be a way forward in determining this crucial value, ϕ.

Clinical applicability is a key component of this study, and so while most studies have used PCF20 for the analogue material due to its similarity to tibial bone (Hvid *et al.*, 1983; Linde, Hvid and Pongsoipetch, 1989; Szivek, Thompson and Benjamin, 1995; Mohammad *et al.*, 2018), there has long been an understanding that the wide variability of bone properties in patients requires some consideration in polyurethane foam studies (Szivek, Thompson and Benjamin, 1995). The range of properties from PCF12 (73.8MPa (±2.5) modulus) to PCF25 (222.2MPa (±1.1) modulus) cover a wide range of the established values of tibial bone moduli (14MPa – 345MPa) (Hvid *et al.*, 1983; Linde, Hvid and Pongsoipetch, 1989; Szivek, Thompson and Benjamin, 1995; Mohammad *et al.*, 2018). Therefore, allowing experimental modeling of a wide range of patients and conditions may lead to a greater understanding of the mechanics of failure in patients.

3.5 Limitations

A major limitation of this study is the use of two specimens for the foam densities PCF 12, 15, and 25, which raises a question about the true spread of the data as conventionally a minimum of three specimens is used for the calculation of the 95% CI. Future studies on this should rectify this limitation, potentially by doing the compression study on more samples of fresh foam for the PCF 12, 15, and 25 data sets to be statistically meaningful.

The model of cellular foam used to characterise coefficients in this study was the open-cell equation. These foams are closed-cell and therefore potential inaccuracies may follow, especially at higher densities. An experiment has been proposed to find the necessary value of ϕ and this should be addressed in future work on this topic and the results compared to highlight the nature and magnitude of the errors introduced by this simplification.

3.6 Conclusion

This study has demonstrated that the mechanical properties of the sawbones rigid polyurethane foam are dependent on density, largely in accordance with the equations put forward in "Cellular Solids" (Gibson and Ashby, 1997). The coefficients presented ($C_1 = 1.341$, and $C_5 = 0.614$) fall outside the expected values ($C_1 \approx 1.000, C_4 \approx 0.050$, and $C_5 \approx 0.300$) which might indicate that these foams might be more accurately be captured by the closed cell foam equations, which would correspondingly require the measurement of further material data (ϕ). While the C_4 value being closer to expected values than the C_5 values may further suggest that the foams retain a dominant elastic failure mechanism; this is despite half of the samples being considered in the plastic region by the elastic-plastic criterion in Equation 1.7. While in the limited case of rigid polyurethane foams, it is felt that these results provide predictive capability for mechanical properties in relation to density in this region. The behaviour of the foams seen is not expected and as such, is a meaningful area for further work exploring the mechanical characteristics of foams in this intermediate density region.

Moreover, with the limitation of specimen numbers considered, accurate and representative material data for the stress and strain data for the foams tested in this thesis have been obtained fulfilling Objective 1.2 laid out in Chapter 1.

Chapter 4 Optimisation of the explicit FE model

4.1 Introduction

In silico studies of high interference orthopaedic implants have been a subject of much research in recent years (Ovesy, Aeschlimann and Zysset, 2020; Pegg *et al.*, 2020; MacAulay *et al.*, 2024). This Chapter will deal with Objective 1.3 from Chapter 1 which states "To use the material characterisation data to optimise the computational model for clinically relevant interferences." This means that this Chapter will optimise the simulation developed in Chapter 2. In Chapter 2 a series of material models, specifically plastic hardening models, were selected as the most optimal for simulating primary fixation in polyurethane foam. Specifically, those of the Drucker-Prager model, a model in which the yield criterion is dependent on the hydrostatic stress state of the material, put forward by Mullins, *et al.* (2009; Toal. V., 2013) and Carnelli, *et al.* (2011; Toal. V., 2013), and the common Von-Mises model (Mises, 1913). All three models will have post-yield plastic hardening behaviour.

This Chapter will include the material data from the polyurethane foam in Chapter 3 in those material models and then select from those three which is the most accurate. This Chapter aims to build on this previous work, and further optimise the selected model for greater model pull-out force prediction accuracy in clinically relevant interferences.

4.2 Methods

Peg insertion was conducted on a 5.65mm additively manufactured round nose peg, as in Chapter 2. The same interference range from very low (0.4mm) to very high (1.6mm), with a 0.2mm step was also used. Furthermore, following Chapter 2 a range of 0.6mm – 1.2mm was taken as the "critical zone" where the simulation was most needed. The diameter of each hole was measured with a plug gauge and calibrated micrometer (±0.004mm) at three locations to account for hole eccentricity, as in Chapter 2.

Material properties for each foam simulated were taken from the results for four densities of polyurethane foam: PCF 12, PCF 15, PCF 20, and PCF 25. The strain rate was kept at 10mm/min to remain in accordance with the test speed of the experimental peg insertion and to avoid inaccuracies generated by the materials viscoelastic properties.

4.2.1 Computational model

The computational model was, as in Chapter 2, a 2D axisymmetric model where the peg was drawn as a round nose peg with length 9mm and diameter 5.65mm, the same as that of the experiment. The foam was initially represented with a refined region, structured mesh, around the hole, and an unrefined, unstructured mesh with larger elements than the refined region, around the outside of the refined region. This was done to reduce model size and decrease the solution time. However, later models (simulation number 2.2, 3.1, and 4.2 from Table 4.1) had the whole foam region meshed as a structured mesh with uniform element size to investigate mesh effects on simulation accuracy. An intermediary step was explored in simulation number 4.1 where the mesh was unstructured around the refined region but of uniform element size.

Table 4.1: Simulation numbers and parameters

Simulation number	Altered parameters
1.0	Drucker-Prager plastic hardening: angle of friction 46, flow stress ratio 1, angle of dilation 0. (Mullins, Bruzzi and McHugh, 2009; Toal. V., 2013). (DP1)
1.1	Drucker-Prager plastic hardening: angle of friction 25, flow stress ratio 1, angle of dilation 10. (Carnelli *et al.*, 2011; Toal. V., 2013). (DP2)
1.2	Von-Mises hardening (VM)
2.0	DP1, Element deletion turned on, fracture energy. (FE)
2.1	DP1, Element deletion turned on, fracture displacement. (FD)
2.2	DP1, FE. Structured global mesh.
3.0	DP1, FE, Aspect ratio compensation 10 (ARC)
3.1	DP1, FE, ARC 10, Structured global mesh.
4.0	DP1, FE, ARC 5
4.1	DP1, FE, ARC 5. Uniform mesh size, structured and unstructured.
4.2	DP1, FE, ARC 5. Uniform structured mesh.

The model was built using ABAQUS (Dassault Systemes, 2020) Explicit FEA with material mechanical data, model geometry, boundary condition, and mesh generation all performed by a Python script. Before each simulated test, a mesh optimisation was run on that model. The mesh was varied from 1.0mm down to 0.05mm and a convergence criterion of ±5% error with relation to the next two smallest meshes was used, as in Chapter 2. If no convergence was found in this region, the simulation was said to have not converged and the model was taken no further.

Three material models previously shown to accurately simulate pull-out force were tested initially, two different Drucker-Prager hardening models and one von-Mises hardening model, simulation number 1.0, 1.1, and 1.2 from Table 4.1 respectively. Parameters for the Druker-Prager models: angle of friction (AOF); flow stress ratio (FSR); and angle of dilation (AOD); were taken from two previous studies on modelling micro-indentation in bone and had the parameter sets (AOF = 46, FSR = 1, AOD = 0, (Mullins, Bruzzi and McHugh, 2009)) and (AOF = 25, FSR = 1, AOD = 10, (Carnelli *et al.*, 2011)).

In all model cases, the yield stress was taken from material test data. This allowed best material model for modelling the extraction force of the peg from synthetic polyurethane foam to be determined. Following the selection of the most accurate base model, the simulation was further optimised using element deletion, which was implemented and and later optimised using a compensation factor.

It has been shown through previous work that element deletion (ED) can closely simulate the damage seen in an interference fit peg in simulated bone (Ovesy, Aeschlimann and Zysset, 2020). Therefore, ED was included in the material model to simulate the damage of the foam caused by the peg more accurately. There are two main methods of determining when an element has reached the damage criterion for damage initiation in ABAQUS: the use of fracture energy and the use of fracture displacement. These two main models were used to trigger the damage initiation in ductile materials based on the corresponding material parameter, plastic displacement (FD) and fracture energy (FE). Both are scaled in relation to the critical element size, and both properties are calculable from each other (*Damage evolution and element removal for ductile metals*, 2024).

Damage evolution is controllable through different models: linear, exponential, and tabular. Element deletion can be triggered immediately on reaching the defined limit, either FD or FE, by setting the damage evolution value to 0 at the maximum plastic strain.

The fracture energy and fracture strain were taken from the maximum compression achieved during compression and it is, therefore, possible that the when the property is reached it will cause early failure. To counter this possibility, a novel technique was investigated where the maximum strain usually allowable in the model was taken as unit one and, based on this unit, the maximum extension allowed in the model was adjusted based on a multiplier. The two maximum extension multipliers, 10 and 5, that were applied were taken from the best practice of keeping the maximum aspect ratio of the mesh below 10, with a lower number being greatly preferred (Felippa, 2012; Burkhart, Andrews and Dunning, 2013).

The optimised simulation was then evaluated as to its accuracy of predicting the pull-out force of a peg from an array of foams. This allowed the generalizability of the model to be assessed. This study aims to reduce the error of the model to a minimum, but will allow a maximum error in the critical zone of up to ±15%. The simulation error was defined as in Equation 2.2.

Errors were calculated as averages of the experimental force against the simulated force. Where the 95% confidence interval (CI) upper and lower bounds are presented for a specific interference, they are calculated from the upper and lower 95% CI of the experimental pull-out force. Where the average of a range of interferences is presented, the 95% CI upper and lower bounds are calculated from the average errors at the individual interferences in that range.

All other parameters of the simulation remained constant. The friction coefficient was taken as 0.2 (Cordey *et al.*, 1979; Adam and Swain, 2011), and applied through penalty friction with an elastic slip value of 0.005 (Adam and Swain, 2011).

4.3 Results

From simulation number 1 to simulation number 4 (Figure 4.1) there was a general decrease in average simulation pull-out force error of both the whole range and the critical zone.

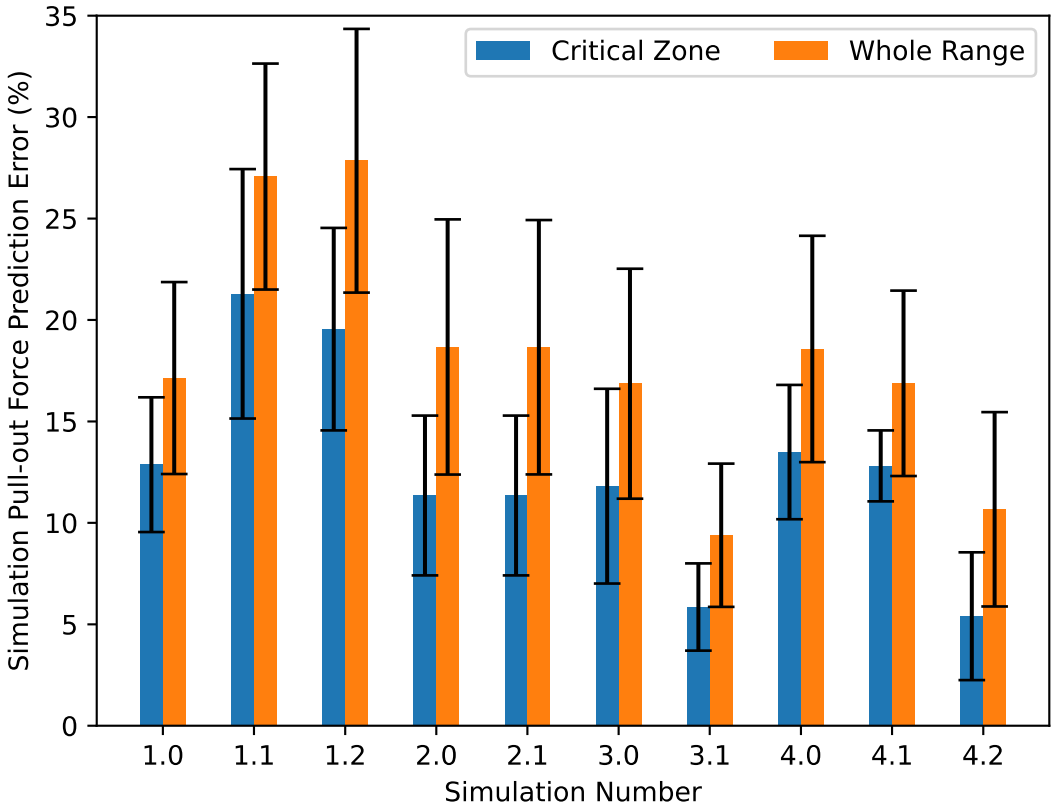

Figure 4.1: Plot of the error of each simulation number and the average error of both the whole range and the critical zone. The 95% confidence intervals of the data used for the averages are also plotted on each bar. Foam mechanical data was that of PCF 20.

In each cast the predicted pull-out force average over the whole range was a higher error than that of the critical zone. Of particular note was that simulation number 1.0 had the lowest error in the critical zone out of all the initial starting simulation numbers (12.873% ± 3.322% 95% CI).

Simulation numbers 2.0 and 2.1 both had lower errors that simulation number 1 and had identical errors to each other in the critical zone (11.349% ± 3.944% 95% CI). The lowest error models were 3.1 and 4.2 with errors in the critical zone (5.847% ± 2.147% 95% CI and 5.399% ± 3.153% 95% CI).

Broadly each of the foams at densities below the PCF 20 (Figure 4.2) are within or close to the cut off limit of ±15% in the critical zone, with average errors of 16.073%, 4.102%, and 5.833% for PCF 12, 15, and 20 respectively.

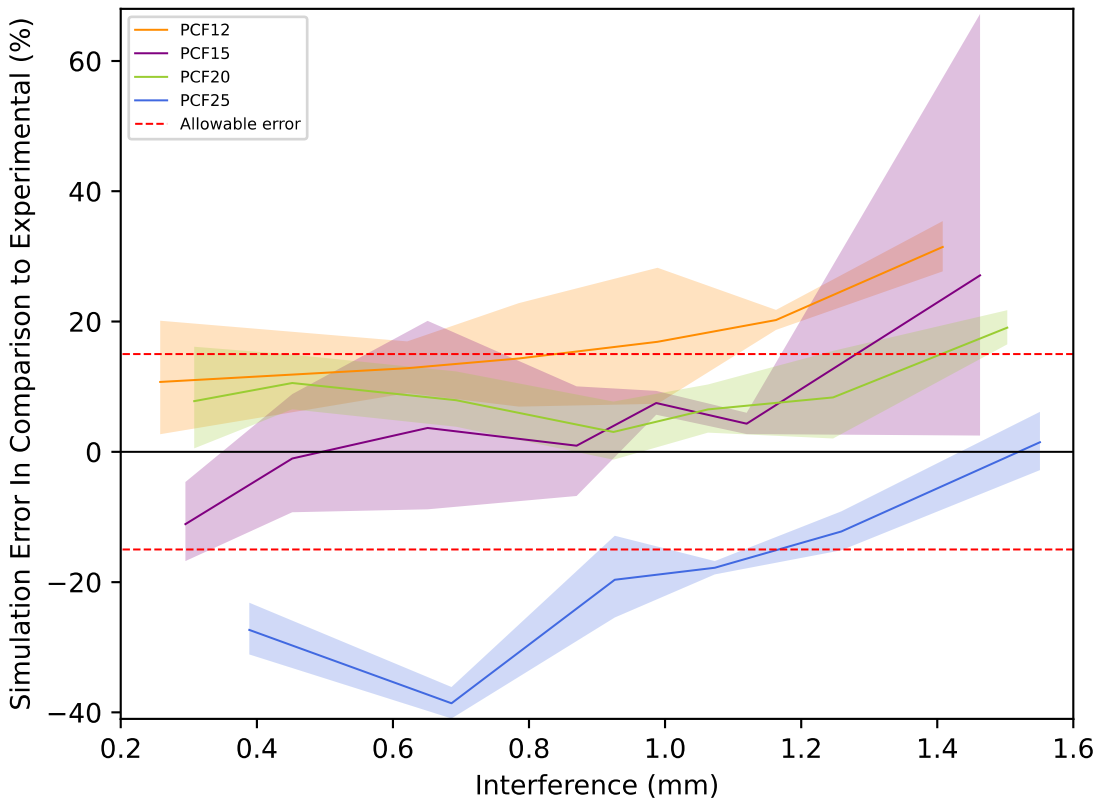

Figure 4.2: Simulation of pull-out force for foams PCF 12, 15, 20, 25. All other simulation parameters those of simulation number 4.2.

PFC 25 has a competitively very different error in the critical zone of -25.356%. The errors of each foam becomes more positive from low to high interference values.

4.4 Discussion

4.4.1 Selection of a base model

Of the three initial models, DP1 was the only one with an average accuracy within the cut off limit of ±15% of the experimental force, with an average accuracy in the critical zone of 12.873% ± 3.322% 95% CI. The other two initial models, DP2 and Von Mises hardening, both behaved similarly to each other, with results average errors in the critical zone of 21.287% ± 6.147% 95% CI and 19.546% ± 4.994% 95% CI respectively. Therefore, the Drucker-Prager model with the parameter set in Mullins, *et al.* (2009; Toal. V., 2013) is the clear leader to base further development on. Consequently, all further models used the DP1 model as their basis.

4.4.2 Introduction of element deletion

Recent work by Ovesy, *et al.* (2019), in the simulation of orthopaedic screws and Ovesy, *et al.* (2020) in the simulation of orthopaedic pegs, has shown great capability in the simulation of damage to the surrounding material using element deletion methods. Simulation number 2 tested the two different methods of including element deletion in ABAQUS, fracture energy and fracture displacement. Following the documentation these two methods should produce the same effect, as each can be calculated from the other, which were verified by the two having identical errors in the critical zone 11.349% ± 3.944% 95% CI. There was, however, a very small difference in the overall average error (18.668% ± 6.287% 95% CI to 18.655% ± 6.269% 95% CI). Due to this small difference, in further developments only the fracture energy ED model was used.

Further, there was only a small accuracy benefit from the introduction of element deletion, ~1.5% difference from 12.873% with no ED to 11.349% with ED. This difference is small and may not be worth the reduced simulation stability, induced by the elements rapidly popping out of existence during deletion. On closer examination of the simulation under conditions where an element was deleted, it was observed that the process was rapid and induced dynamical behaviour in the surrounding mesh. Thus a manner of "softening" this behaviour was sought. This was achieved through the use of a compensation factor which was loosely analogised to the maximum extension of the element allowed in terms of an equivalent "aspect ratio" and functioned by multiplying the element deletion criterion, in this case the fracture energy, by the compensation factor. Factors of 10 and 5 were used in simulation number 3 and 4 respectively. The compensation factors did achieve a "softening" effect where element deletions were not as frequent, and so fewer dynamical effects were seen. However, both lead to successively increased average errors in the critical zone of 11.807% ± 4.798% CI and 13.491% ± 3.310% 95% CI for simulation number 3.0 and 4.0 respectively.

4.4.3 Investigation of mesh effects

The results achieved at this point in the simulation run were good average errors in the critical zone, but some of the individual interferences either at the higher end or lower end of the range were outside the ±15% error cut off. Simulation number 3.0 had 17.00% error at 0.693mm interference and simulation number 4.0 had 17.17% error at 1.063mm interference. This may suggest different dominance of material effects at higher and lower interferences, as the difference between these two scenarios was the fracture energy and possibly some mesh interaction.

Previous work on the development of meshing techniques has made a suggestion that the method of meshing can alter the results of the simulation, in particular that a structured mesh may provide more accuracy in results (Baker, 2005). To investigate this possibility, simulation number 4.1 and 4.2 were run with a corresponding average error in each step of 12.82% ± 1.75% 95% CI and 5.40% ± 3.15% 95% CI, with all critical zone errors in the sub ±15% region. The difference between simulation numbers 4.0 and 4.1 (~0.7%) is very small and the only effect seems to be reducing the larger error at the 1.063mm interference. This small difference is not surprising as the mesh was still unstructured on the unrefined region, with main change that the elements size was made uniform across the foam section. 4.2. However, shows a comparatively large decrease in error from 4.1 (~7.4%) and the results were repeated in simulation number 3.1 (5.847% ± 2.174% 95% CI) with a decrease in average error in the critical zone from simulation number 3.0 of 5.690%. It is possible that simulation number 2.2, the structured mesh approach applied to the base ED FE simulation with no compensation factor, would have produced even more accurate results. However, the simulation did not converge due to widely varying results from one simulation to the next, and so could not be tested under this condition. The accuracy improvements from the structured mesh methodology very clearly demonstrate that the structured mesh method is (in this application) the best meshing method, despite a larger files size and slightly increased computational time. More over as 3.1 and 4.2 both produced very comparable results, simulation 4.2 was taken forward as the best solution from this study because 4.2 was very slightly more accurate on average than 3.1, and the compensation factor of 5 distorts the base material properties less than the 10 value in simulation number 3. However, no specific recommendations between the two models are made.

4.4.4 The generalizability of the model to other foams

In the development of a model, it is important to test if that model has discovered or represented some truth of the system, as opposed to being a curve fit to one specific set of conditions. In this study a comparison was made with the material characteristics from four different foam densities, PCF 12, 15, 20, and 25. PCF 20, the foam the model was developed for, perhaps surprisingly, had the second lowest error in the critical zone (5.833% ± 2.316% 95% CI), and only drifted outside of the ±15% error cut off at the very highest interference of ~1.5mm. PCF 15 (4.102% ± 2.287% 95% CI) had similar average error results and was the most accurate simulation in this regard, though this result should be taken in context with the greater variation in the experimental data, particularly at 0.651mm interference, leading to larger 95% CI plot in Figure 4.2. This greater variation leads to a greater degree of uncertainty in the exact placement of the results for PCF 15, thought the upper 95% CI overlaps with the ranges of both the PCF 20 and PCF 12 results in the same interference region. So it can be said that the results are within comparable range of those of the PCF 20 and 12 results.

The PCF 12 error results are less accurate than the PCF 15 or 20 results throughout the interference range, though are on average within the cut off region at lower interferences, below ~0.8mm. The averages in the critical zone follow the same profile (16.073% ± 2.748% CI), being ~1% over the cut off. This data indicates that PCF 15 and 20 are certainly clinically useful in application, and PCF 12 is very close to being useful, depending on context. All error values in the critical region for these foams were positive; meaning, from Equation 1.4, that the simulation over-predicted the pull-out force present after insertion.

This may be taken to mean that perhaps the yield stress's dependency on hydrostatic stress state, behaviour exhibited by the Drucker-Prager model, which is primarily why the Drucker-Prager model is used to represent foams, is somewhat under-zealous in its effect in this instance. This may be as a result of the angle of friction in reality being larger than the value (46°) used in this study from Mullins, *et al.* (2009; Toal. V., 2013). This statement may itself be supported by the fact that the DP2 model, which had a lower value of the AOF of 25°, itself provided a larger over prediction than the current model. However, a full hydrostatic mechanical characterisation of the foam would need to be undertaken to validate this claim. The author was not able to undertake this experiment due to the equipment not being available. However, this experiment would be valuable to do in future if the equipment becomes available, and a reliable value of the AOF would be expected to increase model accuracy in relation to the experimental results. Moreover, a minor error in the flow angle value used in this study is to be expected as it was produced in a study concerned with the behaviour of bone, and not polyurethane bone analogue. Additionally, the results from the PCF 20 are already comparable to those of similar studies (Ovesy, Aeschlimann and Zysset, 2020; Ovesy *et al.*, 2022), with potentially clinically useful results from PCF 12 depending on context.

PCF 25 is comparatively much less accurate in the critical region than the other foams studied, falling well outside the ±15% cut off in the critical zone with an average error of -25.357% ± 10.640% 95% CI, a decrease from the lowest cut off bound by ~10%. Taken in the context of the previous discussion on the relation of the flow angle of the model to the results, this set of results may indicate that the break for clinically relevant results from the DP1 model is between PFC 20 and PCF 25. The accuracy of the PCF 25 foam may have benefited from the DP2 or the VM model, which may be thought of as a Drucker-Prager model with a flow angle of 0°, though a further study is needed to confirm that these models would be appropriate for more dense foams.

It is possible that the denser foams exhibit less hydrostatic stress dependent yield behaviour, behaving more like solids in this regard. Therefore, it is not recommended that the DP1 model be used to predict the pull-out forces of orthopaedic pegs in a foam that is denser than PFC 20 or less dense than PCF 12.

4.5 Conclusion

It has been shown that for foams in the range PCF 12 – 20 the DP1 model is clinically useful. Moreover, this model is much more accurate with the inclusion of element deletion behaviour, achieving in PCF 20 an error with relation to the experimental of 5.40% ± 3.15% 95% CI. There was no difference between fracture energy and fracture displacement criteria. A further development was that of the aspect ratio compensation factors of 5 and 10, which while there was little to distinguish between the two models, both allowed the most effective improvement to be demonstrated, that of a uniform structured meshing technique. This was a single improvement that provided a reduction in average error of ~7.4% in the clinically relevant critical zone.

Future research may be useful to fully establish a link between the foam density and the angle of friction, though it was shown that the model data provided from Mullins, *et al.* (2009; Toal. V., 2013) was sufficient for the PCF 15 – 20 foams, with potential parameter change needed at the PCF 12 and 25 limits.

It is hoped that these models may be used to develop and optimise future orthopaedic pegs, a process that perhaps will lead to decreased development time and cost and therefore could be of immense benefit to the clinical setting and, ultimately, the patient.

Chapter 5 Optimisation of pegs through novel applications of nose cone geometry's

5.1 Introduction

This Chapter deals with Objective 2 which states "To use the generated computational model to produce an optimised peg design for primary fixation." Therefore this Chapter will take the optimised simulation model developed in Chapter 4 and use it to develop an optimised peg design.

As established in Chapter 1, the fixation geometry of an orthopaedic insert must achieve primary fixation and create the conditions for successful secondary fixation, with this study focusing on the optimisation of primary fixation. One of the primary methods achieving good primary fixation while allowing for reinsertion, an uncommon but possible outcome during surgery (Rahman, 2022), is with frictional forces. Therefore, this work will seek to optimise the primary fixation of a peg that is held in place via frictional effects generated by an interference fit. A goal of a increase in pull-out force of 10%, when compared to the regular round nose peg used in previous chapters, was chosen as the target for this optimisation.

5.2 Methodology

5.2.1 Experimental validation of the optimal peg

The experimental insertion studies in this Chapter were largely consistent with those of Chapter 2 and Chapter 4, specifically the interference range in this Chapter a 5.65mm peg was tested and simulated in an interference range from 0.6mm – 1.2mm with a 0.2mm step, which was defined as the "critical zone". Moreover, the foam used in this Chapter was also PCF 20 polyurethane (Sawbones, 2022) and the peg was inserted at 10mm/min the same rate as material tests in Chapter 3 to reduce the impact of viscoelastic effects on the pull-out force results. Three repeat tests were conducted per interference with the force and displacement recorded at 250hz during insertion and extraction of the peg.

5.2.2 Pressure distribution of a round nose peg

The friction forces that cause the primary fixation are exerted on the surface of the peg through pressure. This pressure is unlikely to be uniformly distributed and therefore, it is likely that some features on the peg contribute more to the fixation of the peg than others. To determine this surface pressure distribution and therefore the location that may contribute most to the primary fixation of the peg, a series of holes were drilled to create a range of interferences between 0.6mm and 1.2mm, in 0.2mm increments. These holes were then counterbored with a larger drill bit from the opposite side of the foam, to a controlled depth from the front surface, set at depths from 10mm – 2mm in 2mm increments. The actual remaining depth was measured by inserting the drill bit in backwards and using the depth probe on the vernier calipers to measure the depth between the drill bit shank face and the foam surface.

As the drill bit did not exactly come up to the hole depth due to the conical drill bit end, a calculation was done in the MATLAB (MathWorks, 2020) program, which was written to process the data. This calculation took into account the offset needed to get an accurate value for the hole depth. A cut away of this experiment in foam is shown in Figure 5.1.

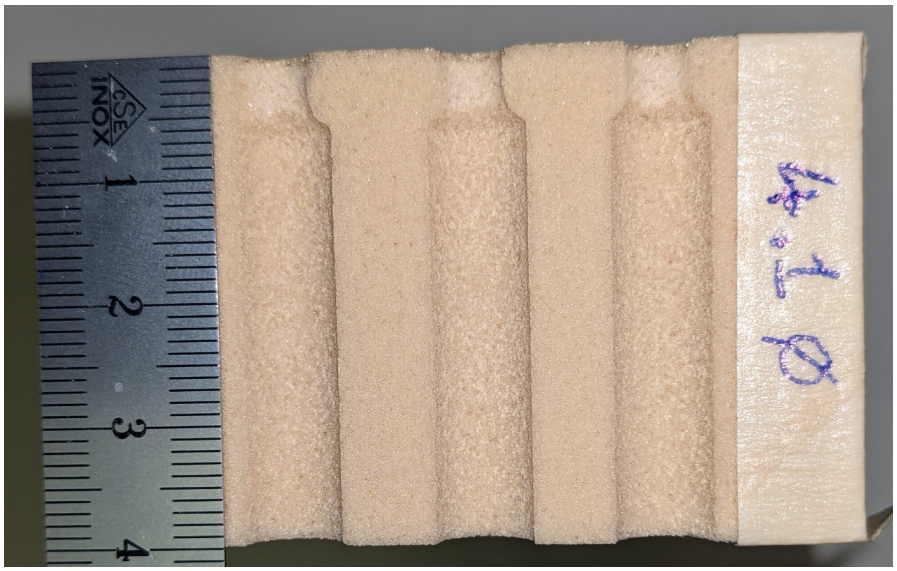

Figure 5.1: An illustrative cutaway example of the counter bore experiment for a high interference 4.1mm nominal hole ~1.6mm interference. This particular experimental data was not used in this study.

The hole depth was measured by inserting the large drill bit into the hole backwards and using the depth gauge on a calibrated vernier caliper (±0.012mm) to touch off against the flat surface of the drill bit shank. Then the diameter of the shank and the known angle of the drill bit tip were used to calculate the distance between where the shank would have intersected the counterbore tapered surface, and the bottom of the known diameter hole.

This then, correspondingly, allowed the surface area in contact with the peg to be calculated. This allowed the pegs to be inserted using the same method as the other experimental insertions and therefore the pull-out force contribution of increments along the surface could be determined.

A comparison to the push-in force would also allow the determination of the surface position where the most fixation force is "lost". The pull-out and push-in force values were turned into surface pressures by dividing the force by the calculated in contact surface area. As these are the forces acting in parallel to the direction of insertion and retraction, they also act in parallel to the surface of the peg.

To turn these forces into the surface normal forces, an assumed constant frictional coefficient of 0.3 was used. However, the specific magnitudes are less important than the indicated distribution. The pressure was then calculated from the area of contacting foam. Once the surface pressures are calculated for each of the hole depths, the isolated surface pressures from each of the smaller depths can be subtracted from the larger depths, to isolate the average surface pressure for that depth difference and location.

5.2.3 Considered designs

A peg may be thought of as a series of surfaces that contribute to the different phases of the insertion and retraction. Initially the peg must be inserted into the surrounding medium, during which it is desirable to cause as little damage to the surrounding material as possible while producing as small an axial force as possible. The peg, then, must be retracted, where it is desirable to have a large holding force. The surfaces then are the frontal area, the nose, which engages with the foam on the insertion stroke and guides the foam around the peg to the sides, and the planar area, the sides, which engage with the foam during insertion and retraction. The surface area in contact with the material is called the wetted area. Further, the ideal peg design would have a flat response to small changes in interference and nose shape, allowing predictable fixation to be achieved with minor errors in surgical procedure and implant manufacture.

The peg designs were aimed at minimising the axial force of the peg and maximising the radial, or frictional component, during retraction. This effect would be gained by guiding the foam smoothly around the frontal area of the peg during insertion rather than being crushed or torn by the leading edge of the peg, therefore preserving the foams ability to apply pressure to the sides of the peg to generate a high friction force on extraction.

A similar objective exists in the field of aerospace, where aircraft or rockets need to push through the air. One solution to this problem, reducing the axial force, or pressure drag of a rocket, as much as possible, are a series of three nose cone geometries which are known as the Haack series (Haack, 1946; Perkins, Jorgensen and Sommer, 1958). Each of the three is optimised for a different condition: length-volume (LV Haack), length-diameter (LD Haack also known as the von Karmen geometry), and diameter-volume (DV Haack). A representation of these Haack profiles as used for nose cones, adapted from Perkins, *et al.* (1958), is shown in Figure 5.2.

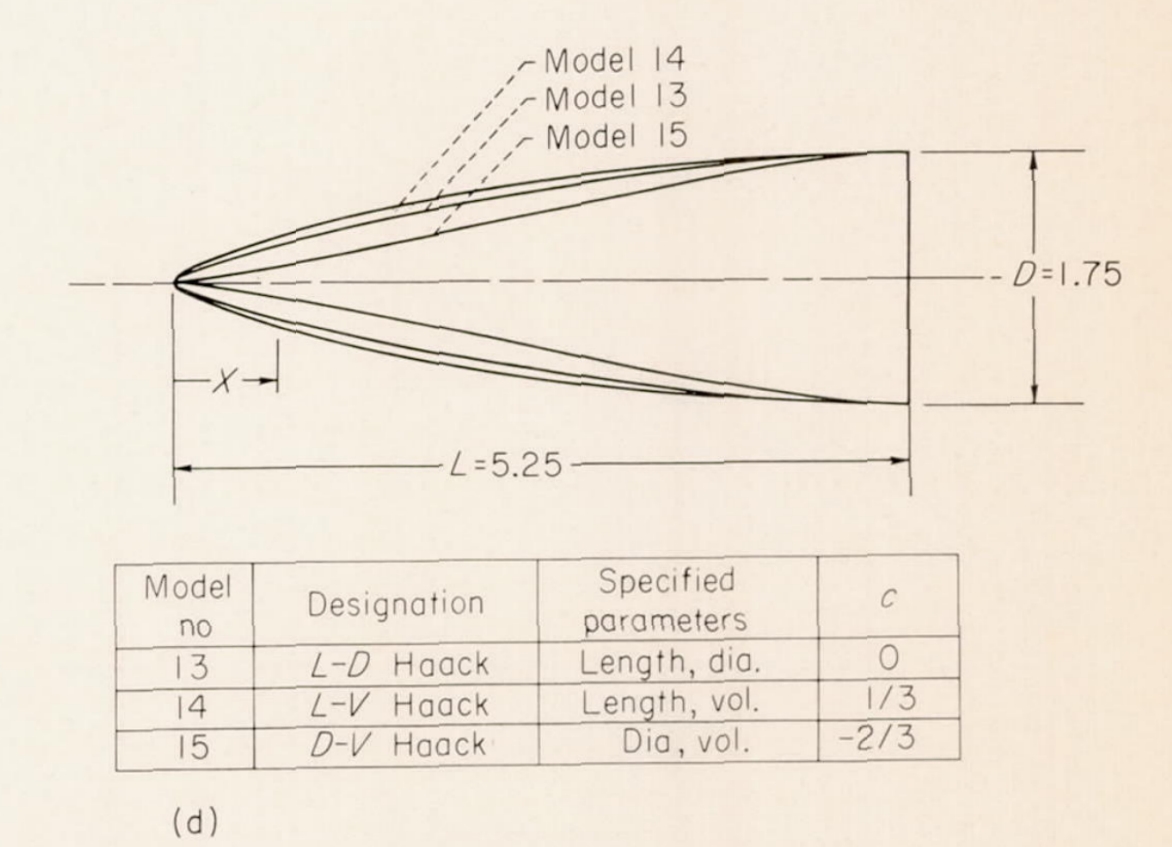

Model no	Designation	Specified parameters	C
13	L-D Haack	Length, dia.	0
14	L-V Haack	Length, vol.	1/3
15	D-V Haack	Dia, vol.	-2/3

(d)

Figure 5.2: A view of Haack nose cone profiles, LD, LV, DV, and the corresponding shape parameter. Adapted from Figure 1, d Perkins, et al. (1958).

Another commonly used geometry is a simple cone. Pegs which have been presented previously, have generally had either round nosed (Bahraminasab *et al.*, 2014; Berahmani *et al.*, 2015; Rahman, 2022; MacAulay *et al.*, 2024), or conical nose sections (van Arkel *et al.*, 2018; Ovesy, Aeschlimann and Zysset, 2020; Rahman, 2022; Jyoti and Ghosh, 2023a) and therefore this work will use a rounded peg as a comparison for the Haack series of pegs.

The Haack profiles shown in Figure 5.2 are adapted as they would be used in the application of a nose cone and so the start of the profile is not offset from the central axis of the rocket. This would not be the case in the orthopaedic peg application of these profiles. As only the section of the frontal area of the peg nose that is in contact with the foam needs to be optimised. Only 1.6mm of the outer diameter (0.8mm of the radius) was formed into the Haack geometry in this study. 1.6mm is the maximum interference likely to be seen by the peg (Berahmani *et al.*, 2015) in clinical use and this minimises the "wasted" surface area of the peg that would otherwise not be in contact with the foam at all if the geometries were allowed to start from the centreline of the peg. These profiles are shown in Figure 5.3.

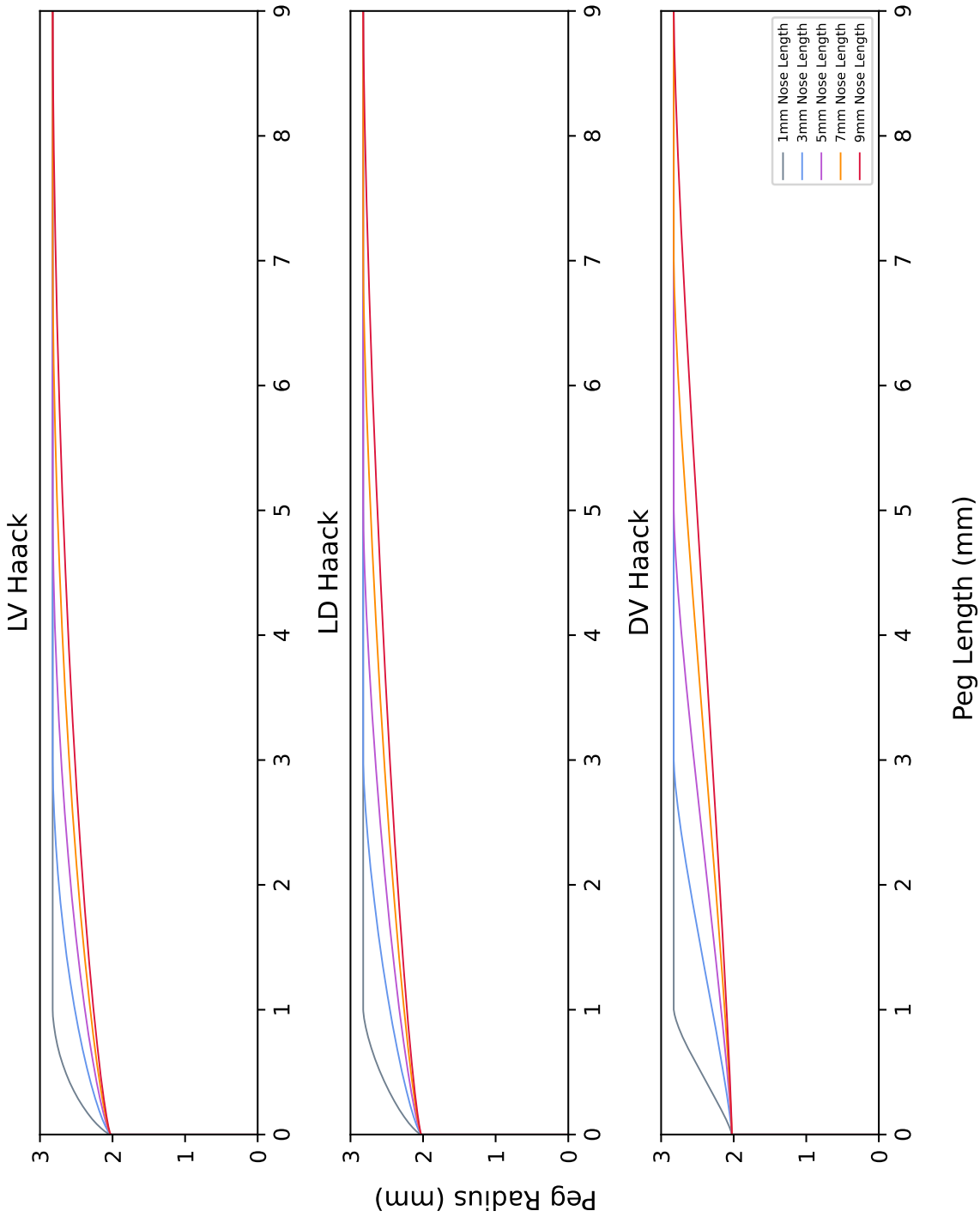

Figure 5.3: All Haack nose profiles used in this Chapter: LV, LD, and DV Haack nose profiles with a flat base to place the full nose surface area in contact with the foam.

Each of these Haack geometries is defined by the effective outer diameter and length of the shape, or its length to diameter ratio, also known as the fineness ratio (FR) of the shape; and a nose form specific parameter (LV: 1/3; LD: 0; DV: -2/3), the equation for these shapes is shown in Equation 5.1 and 5.2.

$$r = \frac{R}{\sqrt{\pi}}\sqrt{\varphi - \frac{1}{2}\sin 2\varphi + c\sin^3\varphi} \quad \text{(Eq. 5.1, (Perkins, Jorgensen and Sommer, 1958, p. 3))}$$

$$\varphi = \arccos 1 - \frac{2X}{L} \quad \text{(Eq. 5.2, (Perkins, Jorgensen and Sommer, 1958, p. 3))}$$

Where: r is equal to the current radius at point X along the length of the nose form, R is the maximum radius of the nose form, L is the maximum length of the form, and φ is the shape parameter.

Perkins, *et al.* (1958) reported a decrease in wave drag coefficient with increasing fineness ratio. Wave drag is an effect that is caused by compressibility in the medium that the shape is moving through and therefore is not expected in polyurethane foam at the insertion rates used in this study. However, this reported data may point to a possible effect that seems to make intuitive sense: that a decreased rate of change on the surface of the peg may make it easier to move the foam around the shape and result in a lower insertion force, potentially damaging the surrounding foam to a lesser degree. Correspondingly, less damage in the surrounding foam may lead to a higher pull-out force.

Therefore, the fineness ratio of the geometries on the peg noses was also altered to investigate this potential behaviour. The Haack nose lengths were varied between 1mm (FR 0.625) and 9mm (FR 5.625), the maximum depth the pegs were inserted too, in 2mm increments. The round nose and rounded edge pegs, both constrained by a fixed tangent condition on both ends of the curve, were limited to a length that equalled their effective radius.

5.2.4 Computational model

A number of models were run using a model made from ABAQUS and a Python script that allowed automatic generation of the model and peg geometry. The models were defined as 2D axisymmetric models. The peg was defined as a rigid body and the foam mass as a deformable body with the material properties of independently characterised PCF 20 polyurethane foam (Sawbones, 2022), Table 5.1.

Table 5.1: Polyurethane foam properties derived from characterisation

Property	Value
Modulus (MPa)	168.948
Yield stress (MPa)	3.722
Maximum plastic strain (End of test)	0.344
Maximum plastic energy (MJ) (End of test)	4.175

The foam was characterised in accordance with *Rigid cellular plastics - Determination of compression properties - BS EN ISO 844:2021* (British Standards Institution, 2021), while using a strain rate of 10mm/min in accordance with the peg insertion test speed.

The material model applied to the foam was that of a plastic hardening, with post-yield experimental data used as the hardening curve, Drucker-Prager model. The Drucker-Prager parameters were taken from those developed in a micro-indentation study (Mullins, Bruzzi and McHugh, 2009; Toal. V., 2013), shown in Table 5.2. Viscoelastic properties were not included in the material model definition.

Table 5.2: Drucker-Prager model parameters (Mullins, Bruzzi and McHugh, 2009; Toal. V., 2013)

Angle of friction (°)	Flow stress ratio	Angle of dilation (°)
46	1	0

Each model was run through a mesh convergence sequence, at its minimum nose length and an interference of 1.6mm, which searched for convergence from sizes of 1.00mm to 0.05mm. Convergence was defined as the point where the maximum absolute error compared to the next two smaller meshes models was under ±5% (Equation 2.1).

If convergence was not reached in this band, the smallest error over the next two models in the search range (1.00mm – 0.05mm) was chosen as the convergence mesh for simulation. This is not ideal, however, simulations requiring meshes smaller than 0.05 absorb enormous computational resources per simulation. The design study for a single nose shape requires 20 individual simulations to be run. Therefore, the simulations were taken as a preliminary study that narrowed the selection to the specific peg that was manufactured and tested.

5.2.5 Peg form measurement

A nose form design was chosen from the simulation results to validate the findings of the simulations empirically. This nose form was manufactured with a CNC lathe, the profile of which was verified using a photographic method. For the photographic measurements to be made each peg was placed on a blank piece of paper and a smart phone was held at a set height of 90mm using a jig. This was the closest distance the phone could be placed, to maximise the pixels covering the peg, and to maintain the photo in focus. The smart phone was a google pixel 5. Each peg was placed in the same place in relation to the jig, close to the centre of the photo, to attempt to minimise distortion effects. A photo was then taken of the peg with a known scale in the image. An example of which is shown in Figure 5.4.

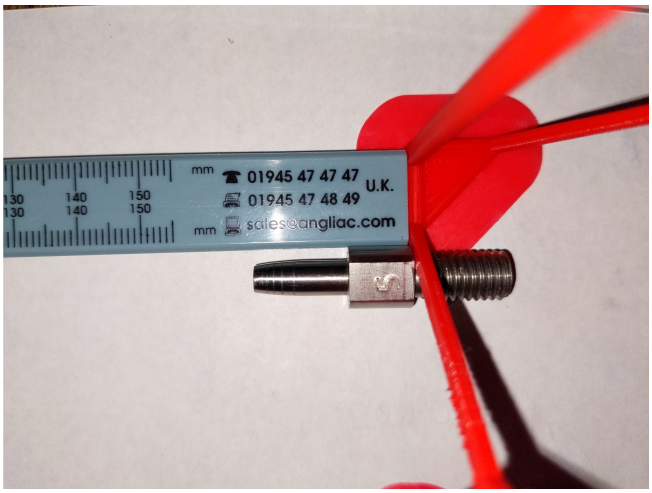

Figure 5.4: An image of a peg that was used in the photographic measurement process. The blue-grey scale can be seen towards the upper portion of the image, and the peg can be seen in the centre of the image. The red additively manufactured alignment jig can also be seen to the right of the image.

The photo of the peg was imported into the ImageJ2 (Rueden *et al.*, 2017) scientific image processing program and points were selected on the scale 20mm apart, and on the upper and lower profile edge of the peg from the front to the straight shaft. The peg straight edge was kept as close to parallel to the phone edge as possible to minimise the straight edge parallel misalignment with the x pixel axis field. The average of absolute misalignment over the shank of the peg was measured at ~9.96(± 2.86 95% CI) pixels over the length of the whole peg (15mm), with a maximum absolute value of ~15.07 pixels over the full length of the peg. These points were then extracted as pixel coordinates. Where the x pixel values did not align exactly, x points from the opposing side were interleaved and the y pixel value for that x point was linearly interpolated from the two pixel coordinate points to either side of the interleaved point. There were now two sets of pixel coordinate points where the x coordinates lined up on both the upper and lower surfaces. Therefore, the approximate diameter could be taken by the difference in the y values.

The maximum y value difference for the shank was ~221 pixels. From these pixel diameters and with the coordinate points of the two measurements 20mm apart, the millimetre diameter of the peg at each point could be determined. The photographic diameter measurement was then checked on the shanks of the pegs with a calibrated micrometer (± 0.004mm) where the error in measurement for all the pegs was an average of absolute maximum difference between the photographic measurement and the micrometer measurement, from the lower 95% confidence interval of the pixel diameter to the upper 95% confidence interval of the measured diameter, was 0.11mm (± 0.02mm 95% CI), with an absolute maximum difference of 0.14mm.

5.3 Results

It can be seen in Figure 5.5 that the main contributing pressure location for push-in force for the each of the interferences is concentrated towards the rear of the peg, at ~2mm depth. In general, the surface pressure increases from front to rear.

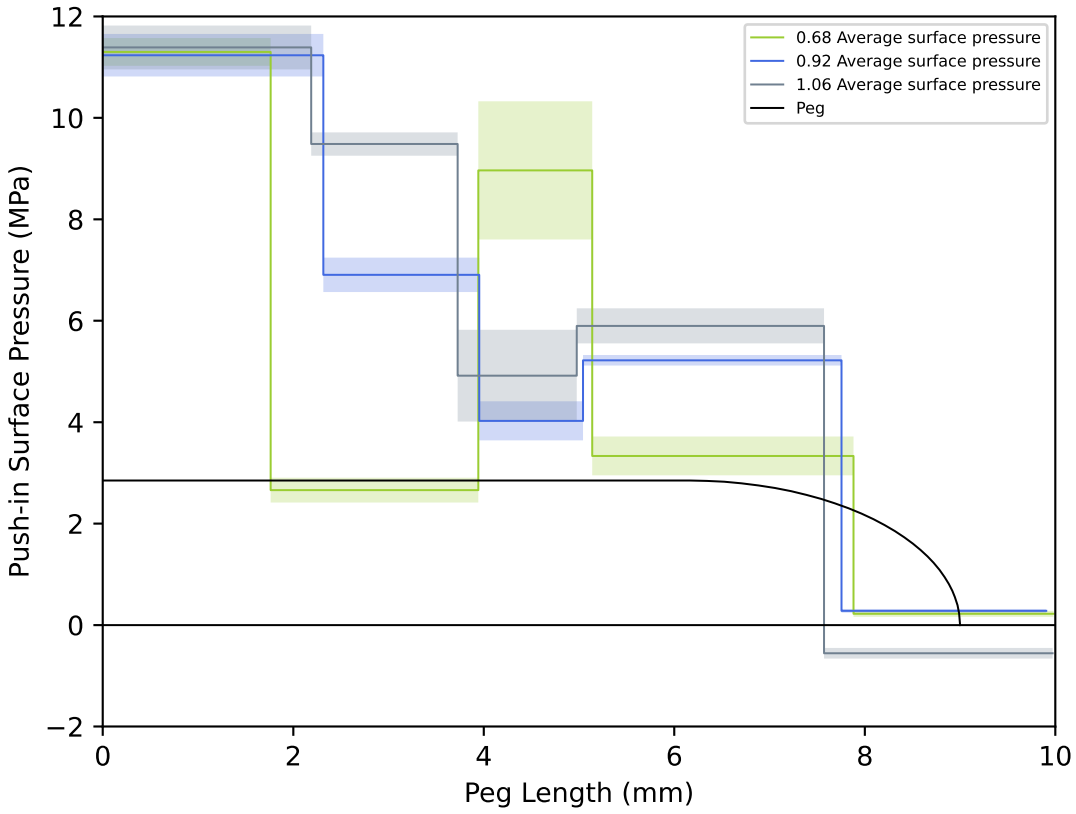

Figure 5.5: The pressure distribution on the surface of the peg during the push-in stroke, calculated from the push-in force values from the counter-bore experiments. Each test was run at a number of different interference values (0.68mm, 0.92mm, 1.06mm). A representation of a round nose peg is shown to help with an intuitive understanding of where the pressures are forming on the surface of the peg.

Noticeably, the 0.68mm interference has a large pressure spike just after the end of the nose section. Interestingly, there is a "thrust" force produced at the nose of the peg under the higher interference values.

In Figure 5.6 the pull-out pressure is in general somewhat uniform across the peg. With a pressure spike at ~4mm – ~5mm depth for the 0.68mm interference hole. This spike is delayed at the highest interference. There also a cosponsoring "thrust" in the higher interference 1.06mm hole. It should be noted that as the pull-out force is opposite to the push-in force these pressures are acting in the opposite direction.

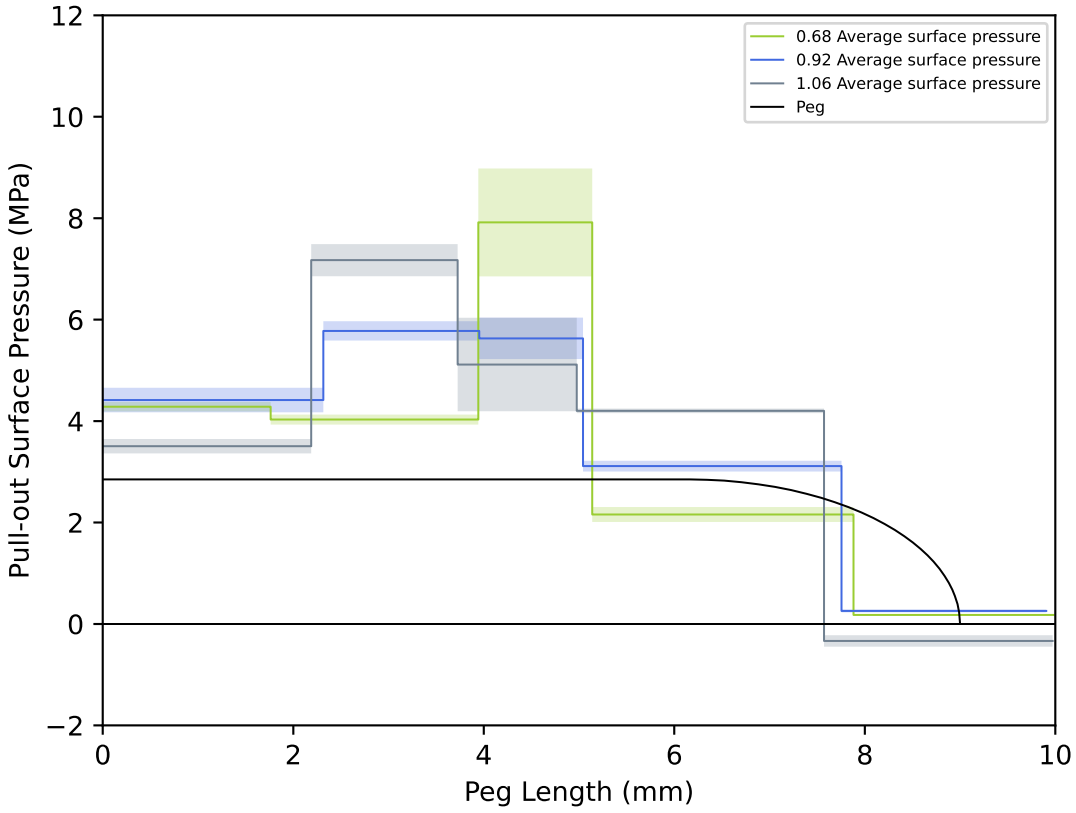

Figure 5.6: The pressure distribution on the surface of the peg during the pull-out stroke, calculated from the pull-out force values from the counter-bore experiments. Each test was run at a number of different interference values (0.68mm, 0.92mm, 1.06mm). A representation of a round nose peg is shown to help with an intuitive understanding of where the pressures are forming on the surface of the peg.

Mesh convergence was calculated for each 1mm nose form design for the next two smaller meshes with the results shown in Table 5.3.

Table 5.3: Mesh convergences for the nose geometries studied

Nose form	Convergence error (%)	Mesh size (mm)
LV Haack	11.7	0.8
LD Haack	16.2	0.7
DV Haack	29.1	0.9
Rounded nose radius 0.8mm	4.6	0.8

The mesh convergence was above the 5% goal for all of the nose forms except the 0.8mm radius rounded nose. The minimum non-converged mesh was for the LV Haack and the maximum for the DV Haack.

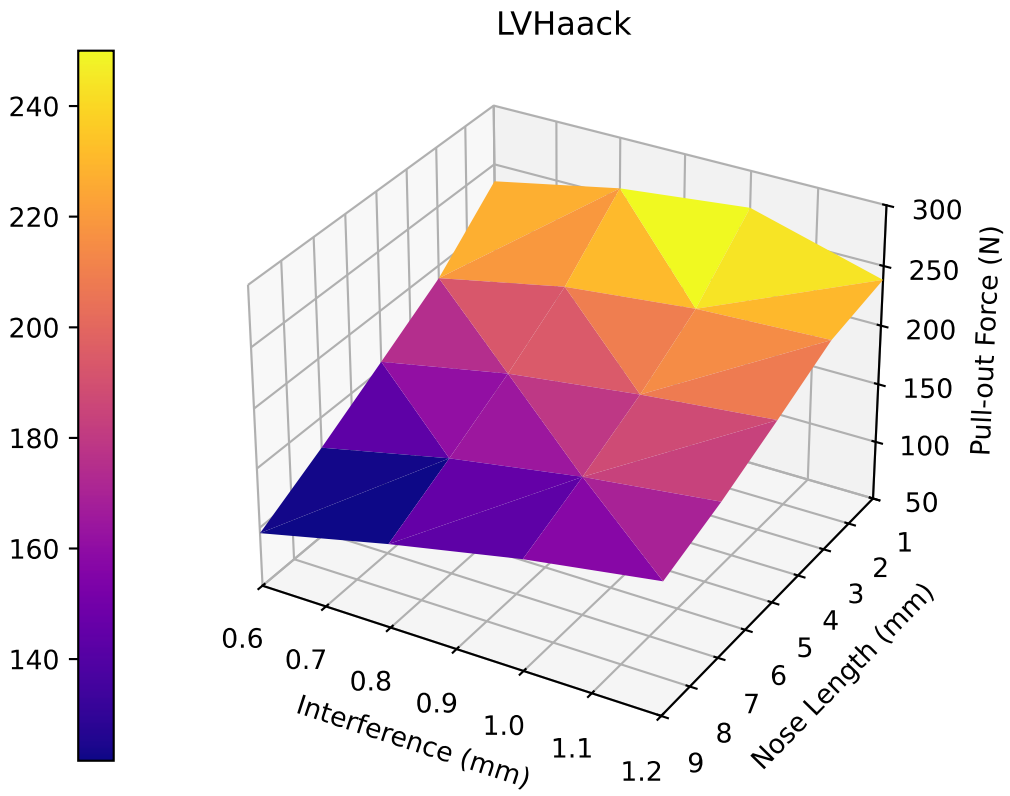

Figure 5.7: LVHaack nose profile, interference and nose length are plotted against maximum pull-out force. The colour scale is a representation of the pull-out force value.

The LV Haack nose form, in Figure 5.7 shows a general increase in pull-out force from 9mm to 1mm nose length, and from 0.6mm to 1.2mm interference, with a peak pull-out force at 1.0mm interference for 1mm nose length. The general pull-out force trend at low FR (1mm nose length) changes after 1.0mm interference, showing a drop in pull-out force from 1.0mm to 1.2mm interference.

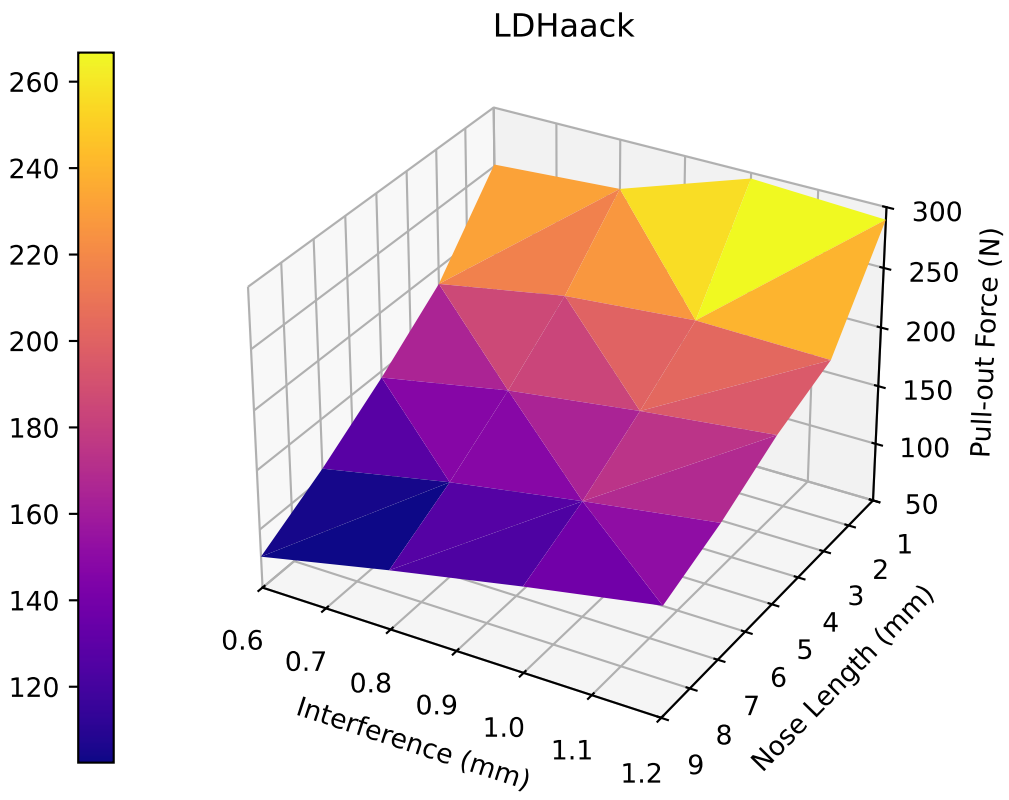

Figure 5.8: LDHaak nose profile, interference and nose length are plotted against maximum pull-out force. The colour scale is a representation of the pull-out force value.

The LD Haack nose (Figure 5.8) also shows a generally increasing pull-out force with decreasing FR (from 1mm nose length to 9mm nose length) and increasing interference with the foam (from 0.6mm to 1.2mm interference value). However, there is a dip in the trend at the 3mm and 1mm nose forms where the maximum pull-out force is seen at 1.0mm interference in both.

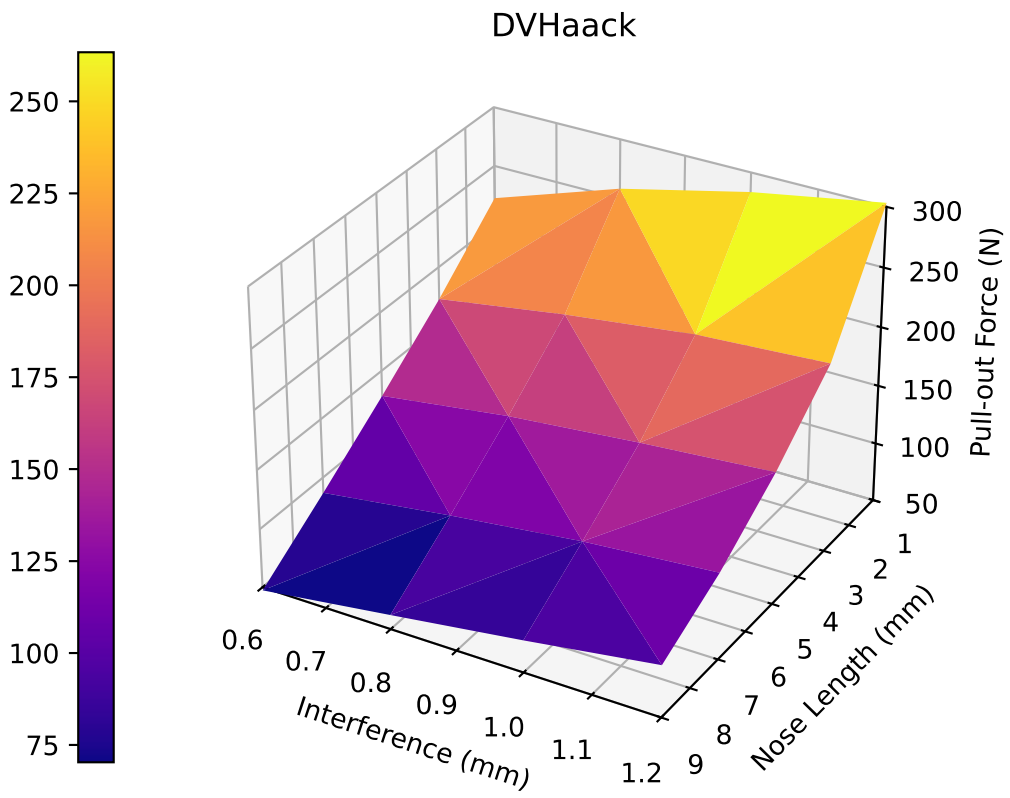

Figure 5.9: DVHaack nose profile, interference and nose length are plotted against maximum pull-out force. The colour scale is a representation of the pull-out force value.

The DV Haack nose form (Figure 5.9) again showed a pattern of increasing pull-out force as the FR decreased (from 9mm to 1mm nose length). It can also be seen that the pull-out force generally increases with interference at each nose length. The increase in pull-out force seems to increase at the upper interference value (1.2), whereas this effect is not seen at the lower interference value (0.6mm). Moreover, this is the only nose form where the pull-out force did not decrease from 1.0mm to 1.2mm at 1mm nose length (low FR nose form).

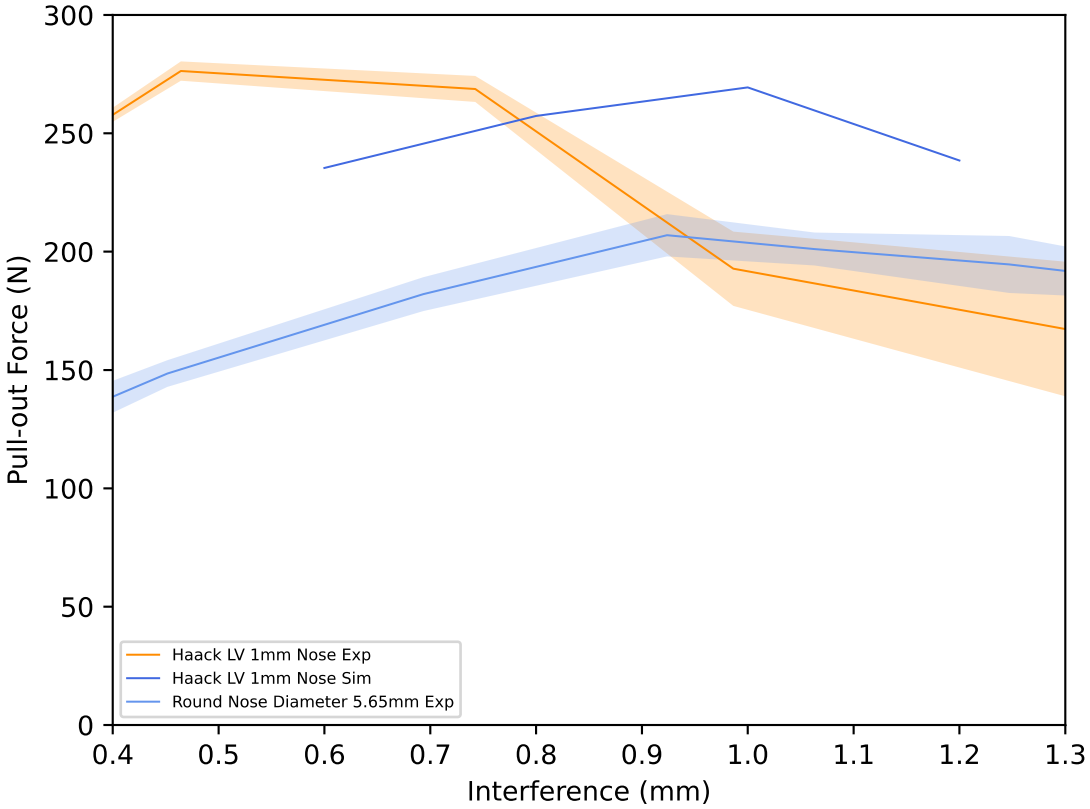

Figure 5.10: LV Haack experimental pull-out force values for a 1mm nose plotted with the corresponding experimental values. A conventional round nose 5.65mm peg are also plotted for comparison.

Figure 5.10 shows a comparison of the LV Haack simulation for 1mm nose length and experimental pull-out forces. The 1mm experimental produces a high pull-out force at low interferences (less than 0.8mm interference), similarly to the 1mm Haack simulation, but follows a steep decline at interferences greater than 0.8mm. The simulation values are an initial under prediction of 33.37N (268.75N at 0.74mm experimental to 235.37N at 0.6mm simulation) but have a crossover to 0.8mm to being an over prediction of 58.30N (180.20N at 1.14mm experimental to 238.49N at 1.2mm simulation).

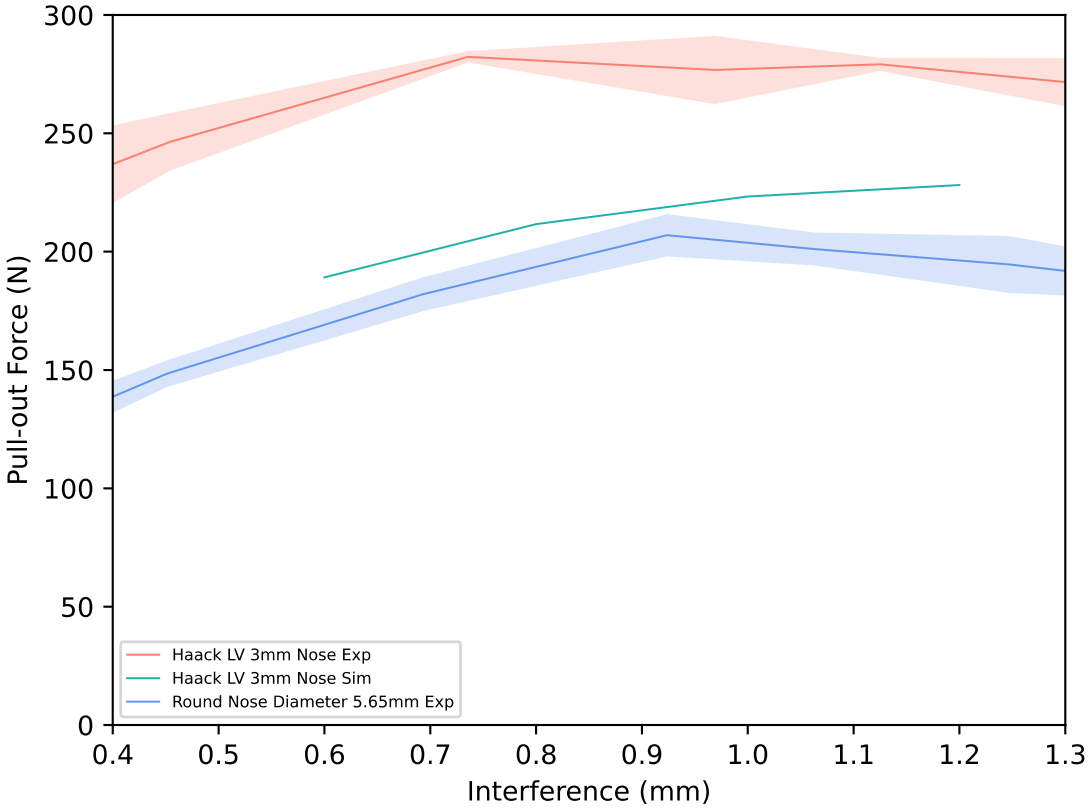

Figure 5.11: LV Haack experimental pull-out force values for a 3mm nose plotted with the corresponding experimental values. A conventional round nose 5.65mm peg are also plotted for comparison.

In Figure 5.11 the 3mm nose follows a similar pattern to the 3mm simulation delivering a relatively flat pull-out force response across all interferences. However, the simulated values are offset across the whole plotted interference range. The value alters with interference, from 93.16N (282.31N at 0.74mm experimental to 189.16N at 0.6mm simulation) to 50.99N (279.12N at 1.13mm experimental to 228.14N at 1.2mm simulation). The round nose 5.65mm peg follows a similar response to that of 3mm LV Haack but at ~100N lower pull-out force value.

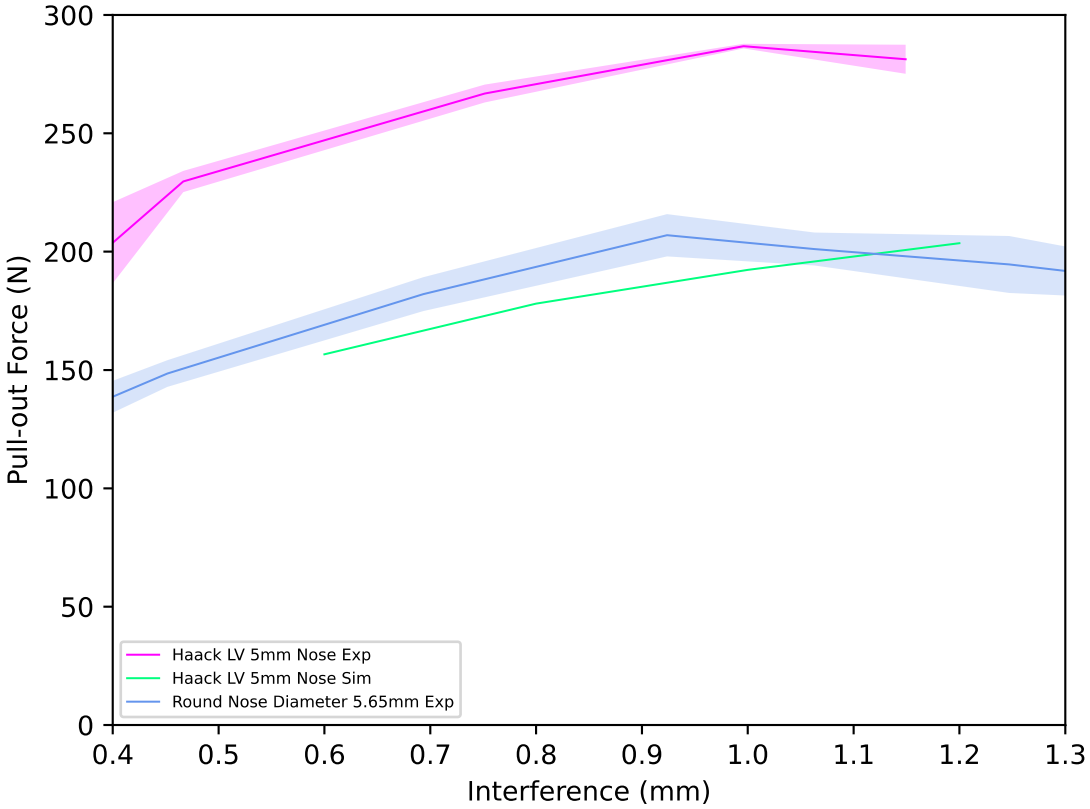

Figure 5.12: LV Haack experimental pull-out force values for a 5mm nose plotted with the corresponding experimental values. A conventional round nose 5.65mm peg are also plotted for comparison.

Figure 5.12 shows the 5mm LV Haack pull-out force values and the corresponding simulated values. A similar trend to the 3mm LV Haack peg is shown with the simulated values under predicting the experimental values, however, at generally lower values than the 3mm. The under prediction changes over the interference range from an under prediction of 110.15N (266.80N at 0.75mm experimental to 156.65N at 0.6mm simulation) to 77.73N (281.28N at 1.15mm experimental to 203.56N at 1.2mm simulation).

The 5mm experimental values eventually reach a similar maximum to the 3mm experimental trend, though at a later interference (~1.0mm) than the peak 3mm performance, and the 3mm experimental values are a flatter pull-out force response to increasing interference overall.

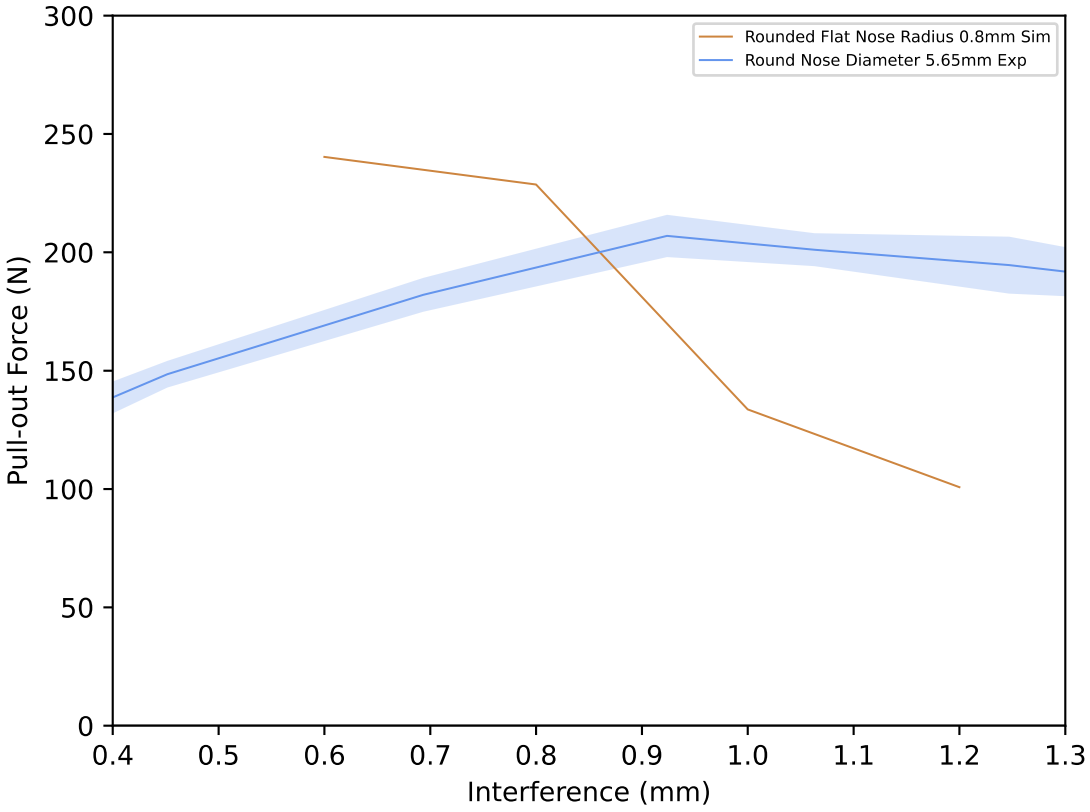

Figure 5.13: A simulated rounded nose flat bottom peg and a conventional round nose 5.65mm peg are plotted.

Figure 5.13 shows the rounded nose radius 0.8mm nose behaves similarly to the 1mm Haack showing an initially high fixation force, but steeply decreasing with increased interference from 0.8mm onwards. The round nose simulation is somewhat similar in form to the experimental values of the 1mm LV Haack peg.

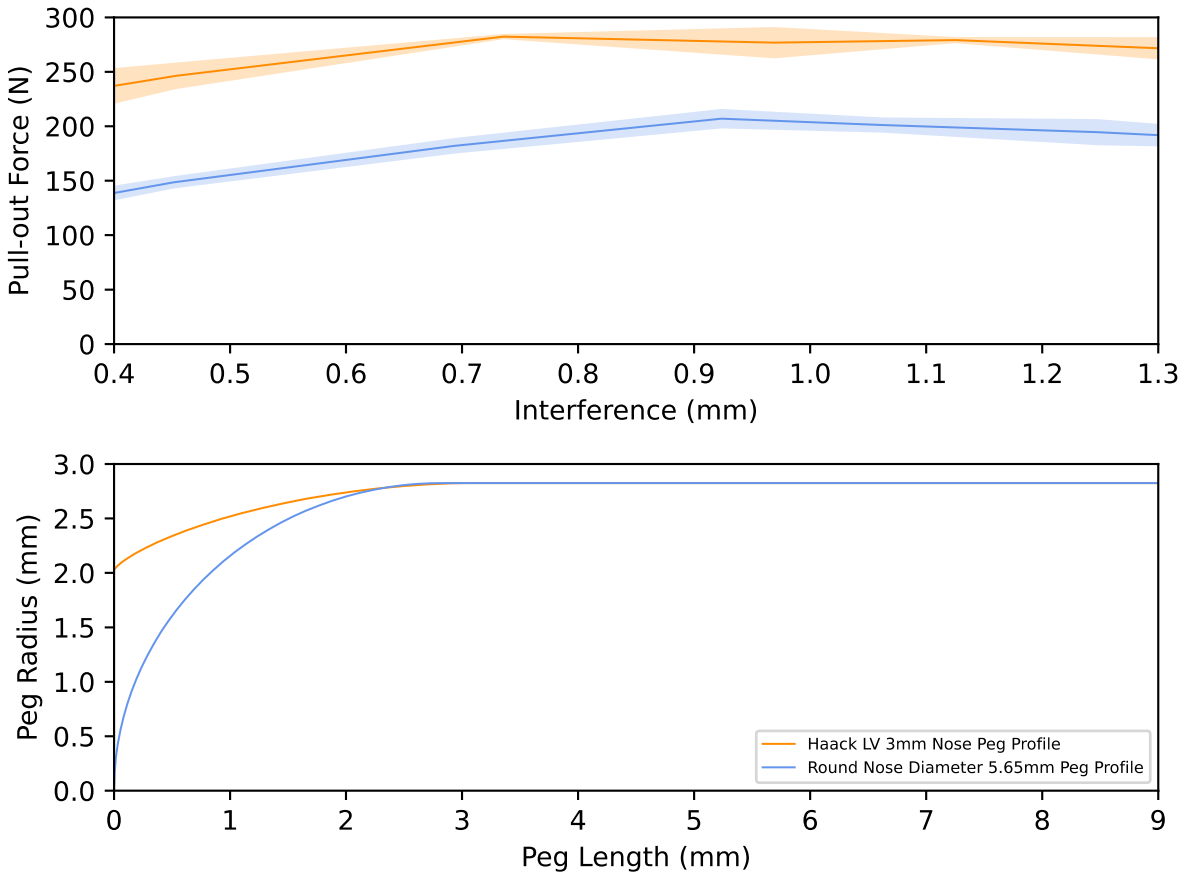

Figure 5.14: A plot of the optimal peg in comparison to the current conventional round nose peg. The upper plot is of the experimental pull-out force values, and the lower plot is of two peg profiles, the current round nose and the optimal LV Haack 3mm nose. The nose profiles are plotted as radius (mm) against length (mm).

Figure 5.14 is comparing the current conventional round nose peg and the optimal LV Haack peg experimental pull-out force values. The two pull-out force plots in the upper graph show that the LV Haack 3mm, an improvement in pull-out over current round nose peg over the full range of interferences plotted with a maximum improvement in pull-out force of 67.52% (129.88N at 0.30mm conventional round nose to 217.58N at 0.39mm LV Haack 3mm) and a minimum improvement of 25.60% (206.63N at 1.25mm conventional round nose to 259.52N at 1.26mm LV Haack 3mm).

5.4 Discussion

5.4.1 Surface pressure on a round nose peg

The surface pressure plots of Figures 5.5 and 5.6 show the main points of interest for the optimisation of the peg form. In particular, the difference between the push-in and pull-out pressure graphs is that there is a noticeable lack of pressure at the base of the peg in the pull-out pressure graph. This may be because the foam is damaged by the whole peg sliding past that section or it may be because the foam is "turned in" during the push-in stroke and "turned out" during the pull-out stroke, increasing and decreasing the normal force exerted by the surface of the foam on the peg. This turning effect is seen in the simulations and if it happens in reality is likely to be of small enough magnitude that it is not easily visible to the naked eye. However, what is immediately obvious is that the primary force generation region on the pull-out stroke is slightly separated from the tip of the peg nose (between the 4mm and 6mm marks on the peg length axis of Figure 5.6). This almost suggests that there may be a kind of "flow" in the axial and radial plane, from the initial point of contact to the midpoint of the peg that acts to reduce the pressure of the foam in contact with the peg on the front portion of the peg. It is also possible to think of this indicated "flow" behaviour as a permanent bending moment caused in the surface of the foam hole by the displacement caused by the peg insertion. This behaviour is interesting, as it would be expected that the foam would relax into contact with the peg when the peg is brought to rest at the end of the push-in stroke, and thereby producing a more even pressure distribution. It cannot be discounted that this effect may also be an artefact of the test method itself as the pressures are not measured *in situ* directly but must be inferred indirectly after the fact.

Despite these somewhat difficult to interpret results, the peak pressure in the mid of the peg is taken to indicate a potential way to increase the primary fixation, by increasing the surface pressure at this location. This could potentially be done by preserving the surface pressure by reducing the damage to the foam by easing its journey around the nose of the peg. However, as is indicated by the push-in results in Figure 5.5, this will also increase the surface pressure in the push-in stroke, therefore, increasing the push-in force too.

5.4.2 The effects of nose profile on pull-out force in simulation

The simulated LV, LD, and DV Haack nose geometries all behaved similarly generally, with the peak force generation being output at 1.2mm by the DV Haack. Moreover, the LD and LV Haack are the most similar in terms of features. Both show a maximum pull-out force at the 1mm nose length and a comparative decrease in the pull-out force at the 1.2mm interference. However, rate at which the different noses drop off from the peak 1mm – 3mm nose length pull-out force value varies, with drop of 93.24N (303.23N – 209.99N) at 1.2mm interference for the DV Haack, a drop of 80.25N (295.36N – 215.11N) at 1.0mm interference for the LD Haack, and a drop of 46.1N (269.40N – 223.30N) at 1.0mm interference for the LV Haack. Moreover, the LV Haack retains the pull-out force advantage over the increasing nose lengths from 3mm – 9mm across all the interferences. Therefore, the LV Haack shows a flatter decrease around the peak primary fixation nose length (1mm), meaning that a change in the nose FR will have a slower drop off from manufacturing errors, resulting in more predictable primary fixation at and around the optimal FR.

The LV Haack and LD Haack had smaller differences across the whole range when compared to the DV Haack. An example of this is the minimum pull-out force in each pegs case of 9mm nose length and 0.6mm interference where the LV and LD had pull-out forces of 95.29N and 76.71N respectively, and the DV Haack had a pull-out force value of 47.23N. This behaviour does align with the geometry that is produced by the LV and the LD Haack parameters being more similar than either are to the DV profile.

5.4.3 The effect of fineness ratio on pull-out force in simulation

A general reduction in push-in force was observed with the increase in FR for all pegs, which is consistent with the pattern of reduced drag coefficient observed by Perkins, *et al.* (1958), though to a different magnitude, for the LD Haack a reduction of 57.14% (0.07 at FR 3 to ~0.03 at FR 5) compared to a reduction of 18.16% (463.73N at FR 3.125 to 379.53 at FR 5.625, both at 1.2mm interference).

This is expected as the two effects are very likely caused by different behaviours in the medium. With this reduction push-force, however, rather than the pull-out force remaining the same or increasing, the pull-out force also decreased with the increase in FR. The reduction in pull-out force may be due to the surface pressure on the straight sides of the peg, dominating in the resistance to retraction possibly as the foam over nose profiles: is not strained to the full diameter of the peg so producing a correspondingly lower reaction force on the surface; and the reaction force on the surface will be split into an axial and radial resultant force, with the axial component acting to reduce the pull-out force of the peg. This would suggest that a peg which is able to expand the diameter of the hole in the foam to the outer diameter of the peg in the shortest axial distance without simply machining the foam away, as would happen with a sharp-edged or corner edged peg, will produce the highest pull-out force.

5.4.4 Optimal nose form for primary fixation

The form of the nose region also plays a role in how much force is produced. It seems that the LV Haack, while not producing the greatest peak fixation, still retains primary fixation performance over a range of FR's, and interferences than the other two Haack geometries considered. With the other two nose forms in order of ranking LD Haack, and DV Haack respectively.

The LV Haack was, therefore, the peg nose form chosen to be manufactured and tested. The LV Haack nose forms from were verified using the photographic method to be manufactured to a tolerance of ±0.1mm in the diametral and axial dimensions. However, this result is approximately equal to the measured inaccuracy of the method, so it can only be said that the surface error is below this value.

5.4.5 Simulation data in context of experimental results

A major feature of the experimental results, in comparison to the behaviour predicted by the simulations, was that the experimental results produced almost universally greater pull-out forces across all FR and interferences. Notably, the 1mm (FR 0.625) nose form pull-out experimental force pattern diverged substantially from this pattern and the simulated behaviour, showing a sharp drop in pull-out force past 0.8mm which was not reflected in the simulated pull-out force pattern. This may be due to the simulation being unable to model properly the foam damage at interferences above 0.8mm, that was caused as the foam flowed around the competitively tight radius. This may be due to a combination of: inaccuracy in the material model; the element size; and the convergence error. The model has been validated in previous studies with round nose pegs to an average error in the range 0.6mm to 1.2mm of 5.8% ± 2.3% 95% CI (Chapter 4).

The element size the convergence study arrived at (0.8mm) is comparable to the nose feature size, meaning approximately one element was in contact with the nose radius at a time. As only the nodes are in contact with the surface the links between the element nodes could potentially penetrate the pegs surface. This would necessarily cause that element to strain less than an equivalent system where there were many nodes all following the nose form surface, as would be the case in a denser mesh. It is uncertain how much this may contribute to the error.

A further reason for this divergence is the lack of proper convergence, as defined in the convergence criteria, achieved in the mesh convergence step. However, the largest error for the next two smaller meshes (0.7mm and 0.6mm) was 11.7% of the pull-out force. Combining the maximum material model error and the convergence error results in these factors, contributing a possible 19.8% (11.7% + 5.8% + 2.3%) error, which results in a maximum force from these errors of 53.34N (of 269.40N) at the maximum pull-out force at 1.0mm interference.

This value accounts for most of the minimum difference between the experimental results (192.80N ±15.69N 95%CI) and the simulated pull-out at 1.0mm of 60.91N. However, the difference between the simulated pull-out force and the experimental pull-out force is not a constant value and so does not account for the difference in pull-out force pattern.

The change in pattern from the lower interference range to the upper interference range, at 0.8mm, indicates that different effects may have contributed differently at higher interferences when compared to lower interferences, which is verified by the rounded nose radius 0.8mm peg, which had very similar simulated behaviour to the 1mm peg experimental pattern and, notably, converged. Though the mesh size was also comparable to the feature size (0.8mm mesh), this may cause errors with the meshes ability to accurately conform to the feature size.

In terms of physical performance of the 1mm nose form, it is possible that the tight radius of the 1mm nose may cause higher peak stresses in the foam, leading to higher plastic deformation in the foam, after elastic retraction, and therefore permanent deformation in the foam. Consequently this leads to a lower surface pressure on the peg after sliding past the tight radius. The plastic phase initiates when there is enough strain to begin plastic deformation. All other experimental pegs increase in pull-out force from 0.6mm to 0.8mm, whereas the 1mm peg begins to lose performance between 0.5mm and 0.8mm of interference. This is a useful design note, as it gives a rough estimate of the minimum radius of curvature feature size that can be sustained by PCF 20 polyurethane foam, which lies between 1mm and 3mm LV Haack nose form.

In contrast to the 1mm nose results, the 3mm (FR 1.875) nose form was the optimal from an experimental pull-out force stand point. The experimental pattern closely followed the simulated pattern with the simulation under-predicting the pull-out force by a decreasing margin as the interference increased of (~93N at 0.6mm to ~51N at 1.2mm).

The response of the 3mm LV Haack peg was very flat across the interference region which is desirable behaviour in the clinical context, as slight surgical and manufacturing errors would not cause a rapid drop of primary fixation, leading to more reliable and predictable results from the surgery. The 5mm (FR 3.125) nose form was very close to the performance of the 3mm peg but underperforming until a crossover at ~1.0mm where the two 95% confidence interval regions overlap for the remaining interference values, meaning there is little to distinguish the 5mm and 3mm pegs at interferences greater than 1.0mm. Moreover, the conventional round nose design is outperformed by a minimum of ~64N which occurs at ~1.0mm interference.

In the critical interference region the 3mm LV Haack peg out-performs the conventional round nose peg, used in previous chapters, by a minimum increase (lower 95%CI to upper 95%CI values) of 33.7% at ~1.2mm interference (276.32N for LV Haack at 1.13mm interference and 206.63N for round nose 5.65mm diameter peg at 1.25mm interference) and a maximum minimum increase (lower 95%CI to upper 95%CI values) of 50.5% at ~0.7mm interference (284.71N for LV Haack at 0.74mm interference and 189.20N for the round nose at 0.69mm interference). A direct comparison to the round nose peg can be seen in Figure 5.14, plotted with the peg forms for ease of comparison. The minimum pull-out force increase supersedes the initial target for 10% pull-out force improvement by about three times. However, it should also be noted that the push in force increased by a similar margin ~30% at ~1.2mm interference (529.92N for LV Haack to 407.56N for round nose 5.65mm diameter) and ~60% at 0.7mm interference (439.12N for LV Haack to 272.87N for round nose 5.65mm diameter).

As the peak push-in forces (Figure 5.5) are at a different location to the peak pull-out forces (Figure 5.6), specifically the top of the peg for the push-in and the mid-peg for the pull-out, it may be possible to reduce the push-in forces by a large margin by tapering in the top of the peg to reduce the effective interference. Rahman (2022) shows a similarly designed peg with a reduction in outer diameter in the upper 2mm of the peg which demonstrates a reduction in push-in force at 1.2mm interference from 357N to 292N from the conventional peg to the reduced peg, a statistically significant p value of 0.035 is shown for the two data sets (Rahman, 2022, p. 167 Figure 6.10 push-in graph). Tapering the top end of the peg would, however, immediately raise the spectre of structural fatigue, as this location is also where all the bending moments of the peg are resisted. That crucial point taken into consideration, this tapering approach may be still be a promising direction for future optimisation work to investigate.

The 3mm LV Haack peg also performs well in terms of pull-out force in relation to designs present in the literature, notably that by van Arkel, *et al.* (2018), whose barbed peg design showed a maximum pull-out force of ~450N and a corresponding push-in value of ~100N for a 8mm diameter and 16mm long peg in Fig. 6 (van Arkel *et al.*, 2018), when tested in PCF 20 polyurethane foam. To compare the peg studied in this work, a 5.65mm peg, must be scaled to that of the comparator peg. Using the surface area of the peg, an average surface pressure can be calculated, a peak pull-out force of 282.32N (±2.39N 95%CI) over the surface area of a 5.65mm peg that is inserted 9mm results in an average frictional surface pressure of 1.77N/mm^2 (±0.01N/mm^2). Specifically, this frictional surface pressure is the pressure that results from the friction force and is already multiplied by the frictional coefficient, which is not known in this case.

An estimate for the average normal surface's pressure could be obtained from this method if the coefficient of friction were known. An 8mm diameter peg in the form of the the 3mm LV Haack design inserted 16mm into polyurethane foam is predicted to produce a peak pull-out force of 711.76N. This assumes the peg will induce the same material effects which may not be the case and the peg may underperform this result. A potential reason for this large difference is that the barbs on the barbed peg may be holding the foam surface away from the foam surface so the peg may not be able to make use of the surface area. Further to this, the surface is porous which will decrease the surface contact of the peg. However, this feature in necessary for the successful development of secondary fixation and a similar feature would need to be included on the current 3mm LV Haack peg before it could be considered for full clinical use.

The van Arkel, *et al.* (2018) peg design retains a large advantage in the required push-in force, a push-in force of ~100N, compared to a calculated 1126.78N push-in force for a peg of the same size, which is a larger push-in force than the push-in force that the solid peg (Fig. 6 (van Arkel *et al.*, 2018)) produced in his study, a push-in force of ~800N. However, the same solid peg produced a much smaller pull-out force of ~110N than the proposed peg, indicating that the retention of pull-out force is predicted to be far better on this proposed 3mm LV Haack peg design than the solid peg from the study.

While the pull-out force is higher for the 3mm LV Haack, the push-in force is also higher which raises the possibility that the benefit gained from increased primary fixation may be offset by the cost of achieving it. This can be evaluated by comparing the 3mm LV Haack to the round nose peg in terms of their respective pull-out force responses to interference. The comparatively flat response of the pull-out force of the 3mm LV Haack form to altering interference values, in comparison to the more concave response of the round nose peg means that, as the interference value is reduced on the round nose peg it loses more pull-out force than the 3mm LV Haack for the same interference, therefore resulting in a greater capacity to reduce the interference value while maintaining a similar level of primary fixation. As previously established, this ability alone holds promise for a surgical error resistant peg design. However, it also allows for the reduction of interference to reduce the push-in force.

Moreover, the pull-out force performance advantage over the round nose peg that the 3mm LV Haack has, allows a further reduction in interference while maintaining a similar level of primary fixation to that of the peak performance of the round nose peg. The round nose peg has a peak pull-out force of 207N (±9N 95% CI) at 0.9mm interference, while the 3mm LV Haack can surpass that value at 0.4mm interference, with a pull-out force of 235N (±17N 95% CI), showing a potential to lower the interference further. Practically, however, a further reduction in interference would be undesirable, as very small interferences are difficult to achieve and small errors could quickly eliminate any interference and render the implant useless. A slightly higher interference is therefore useful to retain some margin for clinical errors in the drilling process.

Further, the 3mm LV Haack nose cone requires an average of 62N less push-in force, 8N from the highest CI bound to the lowest CI bound (from 287N (±40N 95% CI) at 0.4mm to 349N (±14 95% CI) at 0.9mm interference) to achieve that higher pull-out force. More substantively, the current keel design, when tested in PCF20 polyurethane foam, produces a maximum pull-out force of 178N, requiring a maximum push-in force of 738N to achieve that fixation force (Rahman, 2022, p. 139). This means that only a single 3mm LV Haack peg is required to out-perform the pull-out and push-in response of the current keel design and by a large margin, an average difference of 57N for the pull-out and and average of 389N for the push-in force.

While it is possible to design a tibial implant to use a single peg, for example using very small spikes on the underside of the tibial component to resist rotational force, in general a single peg would not be desirable due to the lack of constraint to resist rotational forces. Pitching moments could also cause comparatively high stresses at the base of the single peg in comparison to a two pegged design, due to splitting of the moment arm. However, this single peg performance does provide an argument for the use of a 3mm LV Haack peg in the clinical context to reduce the risk of periprosthetic fracture.

As discussed in Chapter 1, from Equation 1.1, it can be seen that to reduce the stress in the bone from the moment applied at the point of load, in this case the insertion slot or hole for the implant in the tibial plateau, either the distance of the insertion point can be brought closer to the cantilever point or the force acting at that moment arm can be reduced. Taking all other parameters in the equation as constant, which will not be the case as the slot geometry likely removes more second moment of area than the drilled hole as discussed in Chapter 1, the reduction in push-in force from the 3mm LV Haack peg is predicted to lead to a reduction in the moment applied to the knee of 61% for the 3mm LV Haack (287N) compared to the standard keel (738N). Both are multiplied by the same distance factor which then naturally cancels out. Correspondingly, the stress generated in the tibial bone by this moment will also reduce by 61%, providing an effective factor of safety boost of ~157% from using the new peg design. When compared to the round nose, the gains are more modest, with an average reduction of stress of ~18% and average factor of safety boost of ~22% from using the new 3mm LV Haack design.

Following both of these results, a compelling argument is made for the use of the new peg in the clinical context to reduce the risk of periprosthetic fracture in patients. However, this will naturally have a disproportionate benefit for Asian populations and particularly Asian female populations, who currently suffer from such startling fracture rates with the use of the current keel, from 10% - 11% (涂 *et al.*, 2012; Hiranaka *et al.*, 2020; Yudong *et al.*, 2022). There will likely still be a benefit to western populations even though the measure is less critical here as the risk of periprosthetic fracture is already comparatively low with the current keel design, ~0.2% (Mohammad *et al.*, 2021).

In the comparison of this peg with the current keel, it should be born in mind that it is roughened to allow secondary fixation to develop and that roughened surface causes damage to the bone during insertion, both decreasing the pull-out force gained and generally increasing the push-in force applied: an effect which increases at high interferences (Rahman, 2022). A demonstrative example of this is a study comparing rough pegs and smooth 4.7mm pegs done by Rahman (2022, p. 165), who showed that 0.4mm interference these pegs had essentially the same push-in force of ~147N but a difference in pull-out force of 52N (135N smooth to 83N rough). With the rough pull-out being approximately 61% of the smooth pull-out force, we can estimate how a rough 3mm LV Haack peg would perform, giving an estimated 143N, a value smaller than the standard keel.

However, there is a potential mitigation, a smooth nose and a roughened shank, a solution which Rahman (2022, p. 170) demonstrates on different round nose pegs reduces the push-in force and increases the pull-out force slightly, from 208N push-in and 183N 107N pull-out for the rough peg, to 183N push-in and 113N pull-out on the smooth tipped peg. The comparative lack of improvement in pull-out force of these pegs may be explained with the results of Figure 5.6, the smoothed part of the peg appears to be only the last 2mm or so of the peg (Rahman, 2022, p. 170 Figure 6.13) which, on a 5.7mm round nose smooth peg, is shown to contribute comparatively little to the pull-out force. If the smooth part of the peg was extended so that instead of the last 2mm it took up the last 5mm of the peg (from 4mm length to 9mm of the pegs length), then it would be expected that substantially more of the pull-out force may be retained. This would pose a problem from the perspective of secondary fixation however, as this would also substantially reduce the area of roughened surface. This however is an issue that should be addressed in future design of the secondary fixation considerations of this peg.

5.5 Limitations

The predominant limitation in this study is the lack of convergence achieved which very probably impacted the accuracy of the simulated results, particularly at lower FR's which was a potential reason for the consistent under prediction of the simulated pull-out force in comparison to the 3mm and 5mm LV Haack experimental pull-out forces. However, the pull-out force experimental results for the LV Haack nose form demonstrated a very similar pattern to the simulation results shown in Figure 5.7, with the pull-out force generally increasing with decreasing FR and interference. The notable exception to this being the 1mm nose length which showed great promise in the simulations which was not fulfilled in the experimental results, potentially due to the 0.8mm element sizes being too large to model adequately the high stress gradient caused by the 1mm nose feature size, and therefore unable to model the foam stress state. As discussed in Chapter 4, the plastic response of the model can cause long simulation times, which makes establishing convergence for and running very small meshes quite challenging. Therefore, while there is a lack of convergence which is certainly a limitation and, in future work, more time and computational resources would be beneficial to the simulation quality. The current study is seen as a functional trade off between the resources available and the simulation quality. Furthermore, due to the similarity of the patterns observed in experimental and simulation data, the the lack of convergence of these meshes is not expected to change the simulated conclusions of this Chapter outside the 1mm nose length, and it does not effect the conclusions of the experimental work.

Finally, the simulation developed in Chapter 2 and Chapter 4 were largely beneficial in achieving the optimisation of the peg this far. The failings of the model to capture high stress around the small feature sizes of the 1mm nose forms still highlights some elements for improvement with the FEA model, such as achieving convergence at small feature sizes, and accurately modelling the foam damage under the generated peak stresses at these small nose feature sizes. As well as that each simulation of the LV Haack nose forms under predicted, by at least ~50N and generally ~100N, the experimental values.

It can be said that, with these limitations taken into account, FEA (and its application in multidisciplinary studies) is certainly a useful tool to converge rapidly on a series of potentially optimal designs, but as of yet has not removed the need for the experimental validation of that small sub-set of designs.

5.6 Conclusion

A novel approach to orthopaedic peg design has been shown and discussed. Three aerodynamic nose forms have been investigated and compared, the DV, LD, and LV Haack profiles. Each profile was compared at a range of interferences and fineness ratios. The LV Haack was shown to be the optimal nose form due to the competitively flat pull-out response, with an optimal nose length of 1mm (FR 0.625).

The LV Haack nose was then manufactured and tested in PCF 20 polyurethane foam. From this testing, the 3mm (FR 1.875) was shown to be the optimal, achieving at least a 33% increase in pull-out force in comparison to the round nose peg and the 3mm LV Haack as shown in Figure 5.14. This is better than the target 10% pull-out force improvement in Objective 2, exceeding it. A possible reason for the 3mm LV Haack peg being optimal as opposed to the 1mm peg predicted by the simulations was that the tight radius of the 1mm nose may have caused damage that the simulation was unable to capture. Accordingly, a design limit was proposed that minimum radii in contact with the foam during insertion should be limited to the rate of curvature of a LV Haak 3mm (FR 1.875) nose, if using the simulation proposed in this study to design it. Furthermore, this peg compares well to those found in the literature, with a higher predicted pull-out force. Moreover, although a large push-in force was associated with this pull-out force, an estimated reduction of 61% and ~18% in bone stress caused by the insertion force, when compared to the current keel design and a conventional round nose peg respectively, was predicted. This lead to an estimated effective factor of safety increase of ~157% and ~22% compared to the current keel design and round nose peg respectively when using the new 3mm LV Haack design, a strong indicator for the use to potentially alleviate the very high fracture risk of Asian women under the current design.

Consequently, it is strongly hoped that this design will lead to further work on similarly low damaging orthopaedic fixation pegs and, in particular, ones that take into account the needs of long term secondary fixation while limiting reduction of primary fixation from these changes.

Chapter 6 Design and development of a novel knee joint simulator

6.1 Introduction

The goal of this Chapter is to fulfil Objective 3 which says "To enable the evaluation of wear of the current OUKR and future primary fixation of novel OUKR designs through the completion of the development of a novel knee wear simulator." This will be done by completing the development and validation of a novel knee wear simulator for the OUKR that could potentially be developed in future studies to characterise the performance of novel fixation elements, such as a new peg design, under dynamic loading conditions.

As the machine is designed to simulate the Oxford Knee in motion, it will allow the investigation of the motion of the mobile bearing under the dynamic loading conditions, consequently allowing further studies on bearing design, or bearing overhang, which may have an impact on bearing wear rates (Martin *et al.*, 2019). The key focus of this chapter is to characterise the response of this machines motion system to dynamic and static loading, a critical step towards later developing the machine to study implant micromotion.

This chapter was written as part of work conducted with a team over many years. The author of this thesis solely designed the tibial baseplate and its associated fittings (which accepts two OUKR tibial components) to allow a lubrication system to be attached to the machine while minimising the moving mass, the underside support structure for mounting of the tibial base plate, femoral component adaptors, as well as the lubrication attachment guide for the fluid pipes (which attached to the z loading axis). He also designed the gearing system that allowed the rotation of the machine about the flexion axis to be measured.

Moreover, he wrote a substantial part of the MATLAB program that calculated the error in between demand and measured wave forms, in particular, the functions that identified the directory file names, the function that wrote the processed data to file, the flection calibration function, and the main function that tied all the subfunctions together to make the program flow. He also modified the MATLAB scripts written by a team member originally, to fit in the main function data flow, and compiled the MATLAB script into a stand alone binary executable. Further to this, he modified the AeroScript (*AeroScript Programming Language*, 2024) control program that was originally supplied informally by the installation technician from Aerotech. The author also modified the design selection matrix from its original form to a more suitable 1, 3, 9 selection matrix while preserving the selection results, which is shown in Concept selection matrix. Further, the author wrote the original procedure document for running, performing experiments on, and shutting down the machine. Finally, most experiments for this chapter and all of the analysis were done directly by the author, while some of the experiments were done by a colleague under the supervision of the author.

6.2 Methodology

6.2.1 Design Aims

The knee simulator was designed as a bolt on system for a 10.0kN SI-Plan fatigue testing machine. Primary requirements were to test Oxford Phase 3 components. The axes of movement the motion system were designed to achieve were mapped onto the principle axes of motion from the *BS ISO 14243-3* (British Standards Institution, 2014) standard for testing total knees.

The primary axes were: Vertical loading (Perpendicular to traverse plane); Flexion (rotation about the medio-lateral axis); and anterior-posterior motion. These axes were in relation to a coordinate system fixed to the proximal tibia. Ideally a tibial rotation axis would be included. However, this would also increase the mechanical complexity of the design.

Further design requirements were drawn directly from the *BS ISO 14243-3* (British Standards Institution, 2014) standard, specifically mentioning a cycle limit of greater than 1 million cycles at and an operating frequency of 1Hz; and from the motion profile in Table A1 from Annex A: a maximum uniaxial compression in the vertical axis of 2.6kN; a flexion angle requirement of 58 degrees; an anterior-posterior total motion of 5.17mm.

As an Si-Plan fatigue testing machine rated to 10.0kN was available, it was used as the basis for the novel knee simulator. This required the addition of further movement axes directly from the standard; one for the rotation (flexion/extension) of the femoral component, and a second for the sliding (anterior-posterior translation) of the tibial component relative to the femoral component. This would mimic the basic movement of a human knee. As in a human knee there is rotation of the tibia about the central axis of the tibia, a further axis will be added in future. A lubrication system was also added to the machine.

As these criteria were considered, six conceptual designs were produced and evaluated. The selection criteria were: cost, ease of design and manufacture; number of test components; speed; accuracy of motion; maximum load; and robustness. A binary dominance matrix was produced, and evaluation of the desired features was performed in using the conventional 1, 3, and 9 enumerators to enhance the separation of similar scoring concepts. This matrix if fully shown in Concept selection matrix.

6.2.2 Evaluation of torque

The dry torque of the machine is the worst-case scenario in terms of friction coefficient between the cobalt-chrome alloy components and the ultra-high molecular weight polyethylene (UHMWPE) bearing, and therefore the limiting case for the simulators driving torque. The upper mechanism required 4 motors for balance, using 1.96Nm motors, with a gearing ratio of 3.697, acting at the radius of the femoral component 23.5mm, would stall at a vertical force of 1.23kN. Similarly, for the tibial platform; 1 motor, rated at 4.31Nm with a leaver arm of 35mm would stall at a horizontal force of 0.246kN, equating to a vertical force of 1.231kN when the friction coefficient of 0.2 is taken into account. Inertial and moving part friction losses for both movement systems were estimated and found to be negligible compared to the driving torques to overcome friction. The lubrication system allows lower frictional coefficients between the bearing and joint surfaces, opening the door to higher vertical forces.

6.2.3 Control system

The control system was implemented using an Aerotech iXI4 control box (*Automation1 iXI4 Servo Interface with Motion Controller | Aerotech*, 2024) and a custom program to read in a motion comma separated variable (.csv) file and control the motion of the axes. The goal was to provide accurate positioning and recording of position data to an output .csv file.

This was achieved using the Aerotech iXI4 control box (*Automation1 iXI4 Servo Interface with Motion Controller | Aerotech*, 2024) with the Automation 1 software (*Automation1 iSMC Intelligent, Software-Based Motion Controller | Aerotech*, 2024) and the AeroScript programming language (*AeroScript Programming Language*, 2024).

The control box has a pre-installed control loop which can operate in a closed loop if the motor attached were capable of that functionality. In this application however, the motors used were off the shelf stepper motors which were not capable of closed loop control. Consequently, the machine was run in open loop control. The closed loop control subsystem is designed for servo motors, the use of which would potentially have increased the positional accuracy and ease of use of the machine, but would certainly have increased the complexity of the system.

The proposed design called for five stepper motors, four on the rotational axis and one on the linear axis. The four rotational steppers were RS 798-3646 using 4.4V and 2.0A and the single linear motor was an RS 798-3640 using 6.4V and 2.0A. Both stepper motors had a 1.8 degree per index types. The rated voltage and current draw resulted in net rated motor power requirement of 48W which was supplied by a separate power supply. The power was distributed and controlled by five Geckodrive 201X 10 micro-stepping (minimum 0.18 degree steps) stepper drivers, with the power output set to deliver a maximum of 2.2A (max 52.8W).

Feedback on each axis was measured directly, an elpm75 eurosensor linear potentiometer was used to measure the displacement of the tibial bed in the AP direction, using a direct linkage. The flexion was measured likewise with a direct gear train (ratio 1:1). Both linkages allowed load to be minimised on the sensors while measuring displacement accurately.

The iXI4 control box (*Automation1 iXI4 Servo Interface with Motion Controller | Aerotech*, 2024) was supplied by its own 12V power supply, and interfaced with the stepper motor control pins via a custom wiring loom. The step pulse was wired into each stepper for the rotation to allow single point control of all stepper drivers with the polarity switched on the motors which needed to rotate in the opposite direction.

6.2.4 Calibration

Each axis was calibrated independently. In both cases the voltage reading was tested to make sure that the expected range of the axis would remain within the limits of their respective potentiometers (0 to 5V in both cases). Each axis was placed into a defined "zero" state, for the anterior-posterior axis this was when the rear face of the bearing was parallel to the tibial component, and for the flexural axis, this was when the lower flat of the femoral component was parallel to the tibial plateau.

A desired linear ramp displacement was input to each axis, 0 to 5mm and 0 to 60deg to the anterior-posterior and flexural axis respectively. The actual displacement was measured using a pair of vernier calipers (±0.04mm) for the anterior-posterior axis and a digital protractor (±0.1°). The difference between the desired and measured movement gave a ratio to adjust the steps per unit motion in the Automation 1 axis calibration. This calibration method was repeated until the maximum error between the demand and the measured position over three tests was below ±5% (±3% anterior-posterior and ±0.3% rotation).

6.2.5 Evaluation

The specification in the standard requires that the machine to be able to move in both the flexural axis and the anterior-posterior axis while applying load in the vertical axis. During motion, each of these axes is expected to be synchronised with each other to achieve the required combined accurate positioning.

As the control system records data analogue data from each of the axes as well as the demand signal for that axis, a test was derived to assess the accuracy with which the axis follows the input demand motion profile as the root mean square (RMS) error of the demand and actuation signals, calculated in the units of each axis. As the control system does not directly control the vertical loading, there is no demand to compare against and, consequently, no RMS error calculated. Following this as each demand signal is properly synchronised, the maximum degree of de-synchronisation between axes will be a result of the maximum RMS error of each axis.

6.2.6 Constant vertical load lubrication tests

As the vertical load varies in the AP and flexion *BS ISO 14243-3* (British Standards Institution, 2014) load profiles, it is difficult to asses the points of peak loading on the system caused by the combined motion of the axes and the vertical load. Therefore, a constant vertical load testing cycle was run after the machine was calibrated, where the AP and flexural axes were made to follow their *BS ISO 14243-3* (British Standards Institution, 2014) profiles.

The first constant load test was on the influence of lubrication on the practical motor stall load. This is in effect a study of the effect of coefficient of friction of the bearing surfaces on the motor stall load. When the stepper motors were unable to follow the demand profile, they would lose their location, a process where the motor was either prevented from rotating or back driven by the forces applied to the axis. In both of these cases an audible “clicking” sound is heard from the motor, and this was designated as “skipping”. First the lubrication system was checked to make sure it was clean from the previous run, if not it was cleaned with dishwashing liquid and water. Then the new lubricant was then loaded slowly into the system by pouring it onto the tibial tray drainage holes. The peristaltic motors were on during this step, and the outlets were positioned in a drainage bin. The fluid loading continued until the outflow of the outlet pipes was consistently observed to be the input fluid, at which point, the motors were turned off and the outlet lines were attached to the fluid pipe support holder.

Following this process, the pumps were restarted and the fluid level was topped up until a uninterrupted stream of the test lubricant was observed running into the joint. The vertical load was then applied and the motion profile was run for a period of 120 cycles at 1Hz with the results recorded. The load was varied from 200N upwards in increments of 200N until the skipping sound was heard. The load at which this happened and the corresponding lubrication used was recorded. This test was repeated three times at each load. However, some loads were skipped in the Olive Oil test and the load was rapidly increased up to 7kN after 3kN.

6.2.7 Constant vertical load error baseline

Once the motor stalling load was established under different lubrication conditions, a further test was done under constant loading conditions to establish the baseline RMS error for the AP and flexural axes under the worst case scenario for coefficient of friction, dry conditions. The machine was then subjected to one thousand cycles in dry conditions at a low compression load of 5N, and at the maximum non-stalling load of 600N. With the RMS error under each load recorded, and three test done of each.

6.2.8 Long term sinusoidal loading

With the baseline error established, the machine was then tested under "long term" tests of ten thousand cycles in dry and wet lubrication conditions simulating knee motion with the *BS ISO 14243-3* AP and flection profiles. The vertical load was a sinusoid with variation of ±50% of the median load. The load forms applied under these dynamic vertical loading are shown in Figure 6.1, each normalized to a percentage of their maximum values. The load forms applied to the knee joint under constant vertical loading were the same for AP and Flexural motion, but the vertical load was a constant set load.

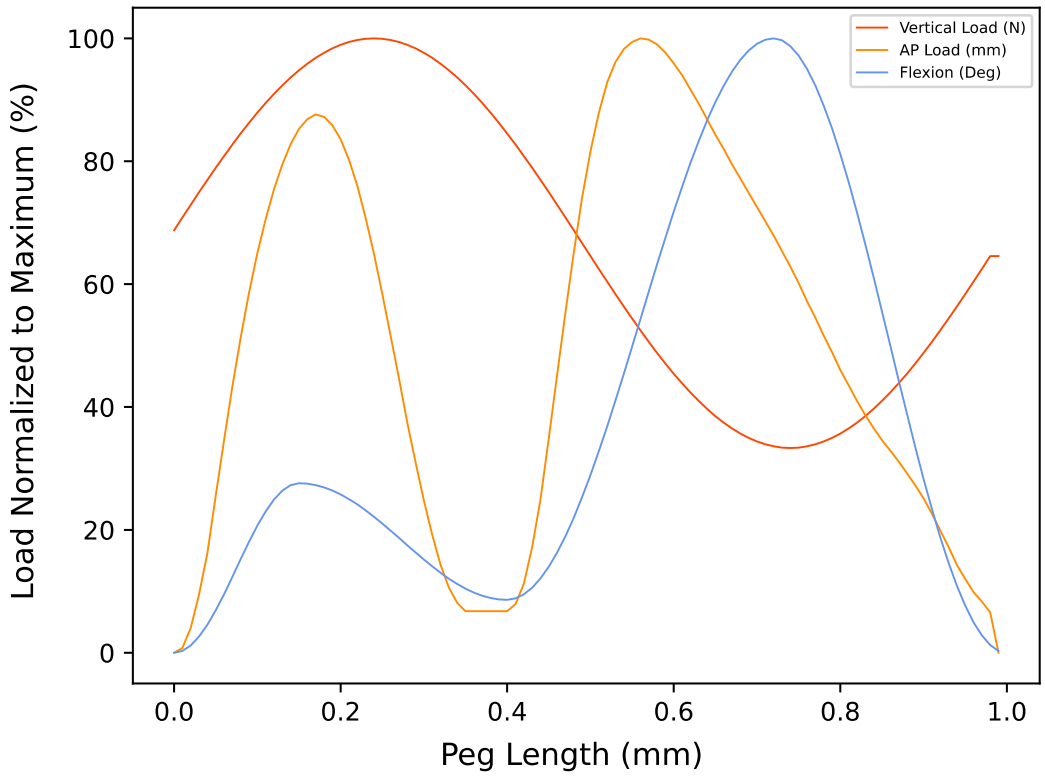

Figure 6.1: The load forms applied to the the knee joint by the machine under dynamic vertical loading. Each is normalized to a percentage of its maximum value.

Then a full *BS ISO 14243-3* (British Standards Institution, 2014) load profile was used with Olive Oil lubrication, the greater lubricity allowing the higher loads to be applied to the joints. The standard calls for 2.6kN per joint meaning a total of 5.2kN for the whole machine as there are two joint compartments. This load profile is shown in Figure 6.2.

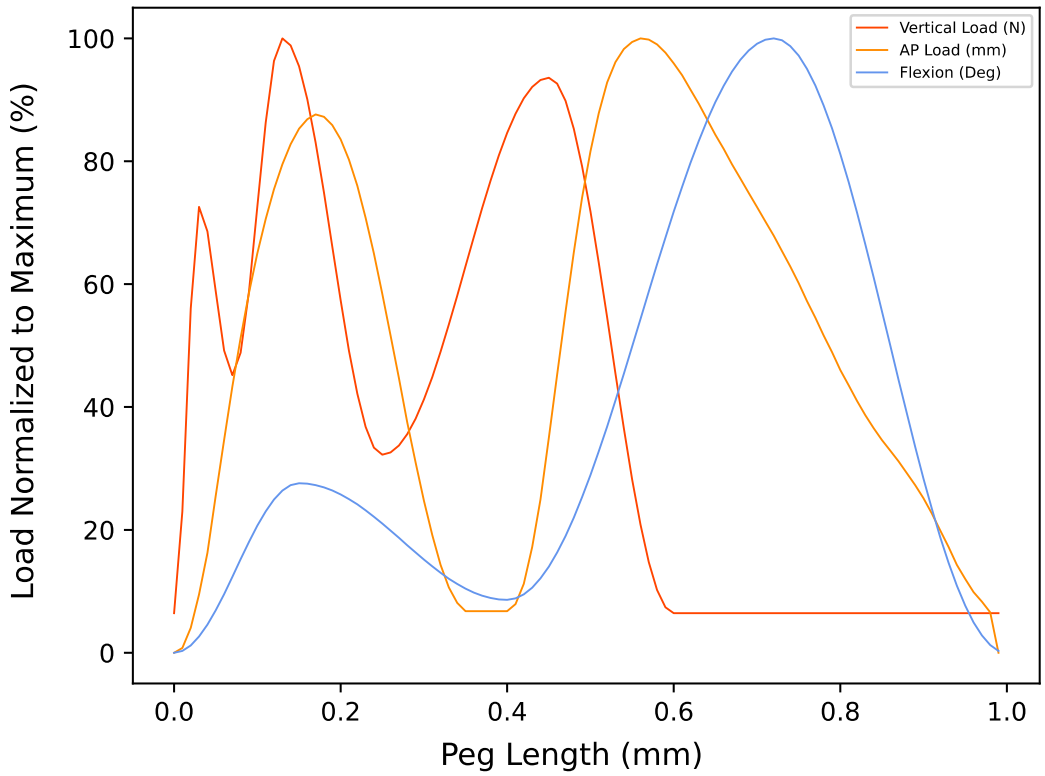

Figure 6.2: The BS ISO 14243-3 (British Standards Institution, 2014) load applied using the Olive Oil lubricant.

From this standard load pattern the machine can be assessed against principal design loading. In the "long term" tests the RMS was calculated over ten cycles every 100 cycles allowing the error progression of the machine to be tracked.

6.2.9 Statistical methods

The RMS error response of the AP and Flexion axes of the machine to increasing load established under the constant loading baseline test was analysed for statistical significance using a single factor analysis of variance (ANOVA) test using Microsoft Excel (Microsoft Corporation, 2021). The test was done to compare AP data under 5N and then under 600N, and then the flexion data under the same conditions. The three experimental data points for each state were used in the analysis.

6.3 Results and Discussion

Based on the design criteria established and the results of the concept selection matrix, a two axis bolt on system was selected to as the preferred form of the design and was continued to detailed design and manufacture. The selected design is shown in Figure 6.3, which has some old test components designed by colleagues in it. The components designed by the author, which are currently on the machine, are shown in Figures 6.4 – 6.10.

6.3.1 Machine design

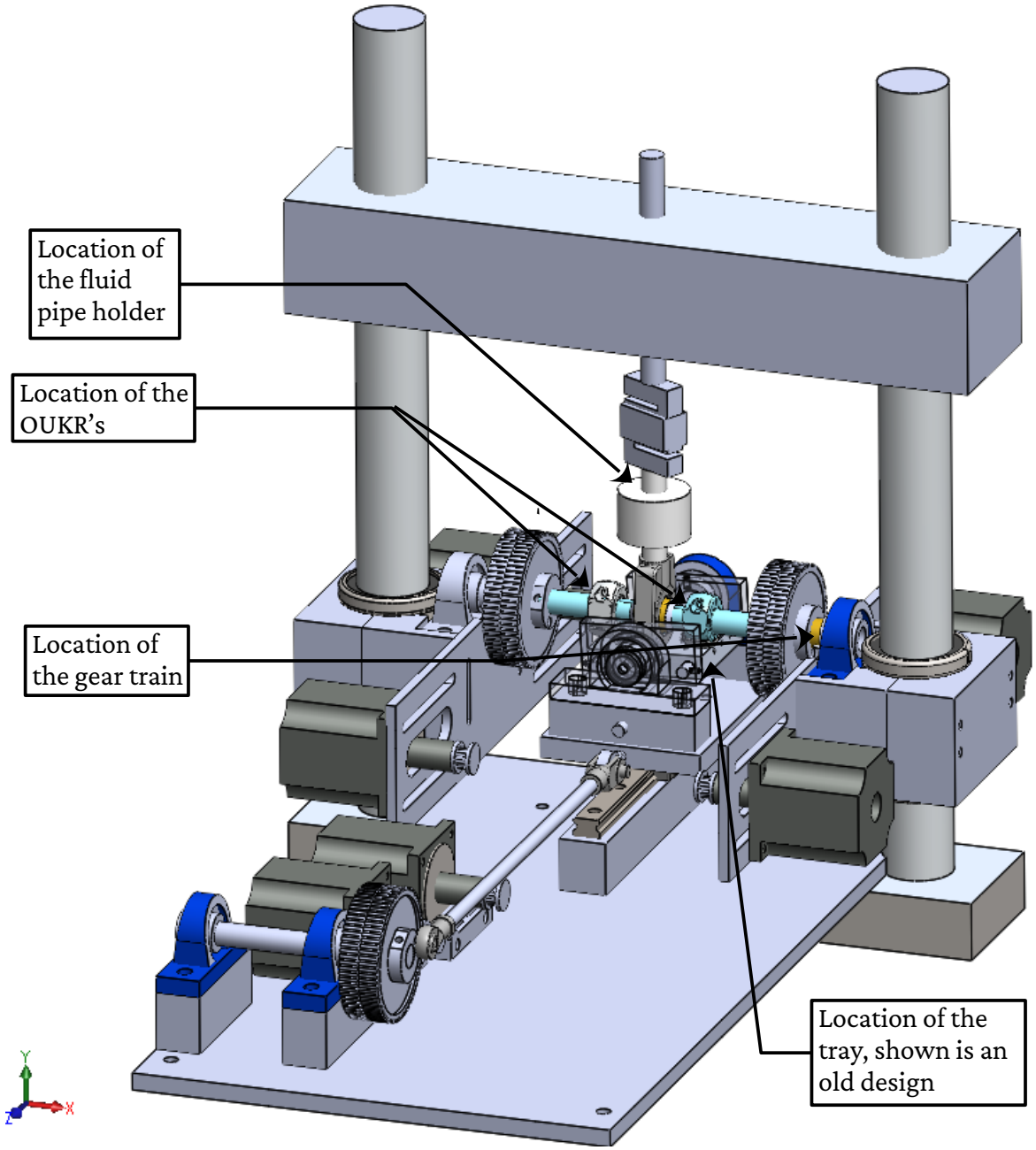

Figure 6.3: Isometric view of the preferred additional two axis design built onto the frame of the SIPlan fatigue machine, which can be seen in as the vertical frame.

As the tibial baseplate design was a moving part, the design made heavy use of the concept of isogrids to lighten the structural mass as much as possible while retaining stiffness (Huybrechts and Meink, 1997; Li *et al.*, 2019). The tray design also features a sloped surface design to funnel lubricant run off and wear debris from the OUKR towards the drainage holes where it would be filtered and recirculated, shown in Figure 6.4.

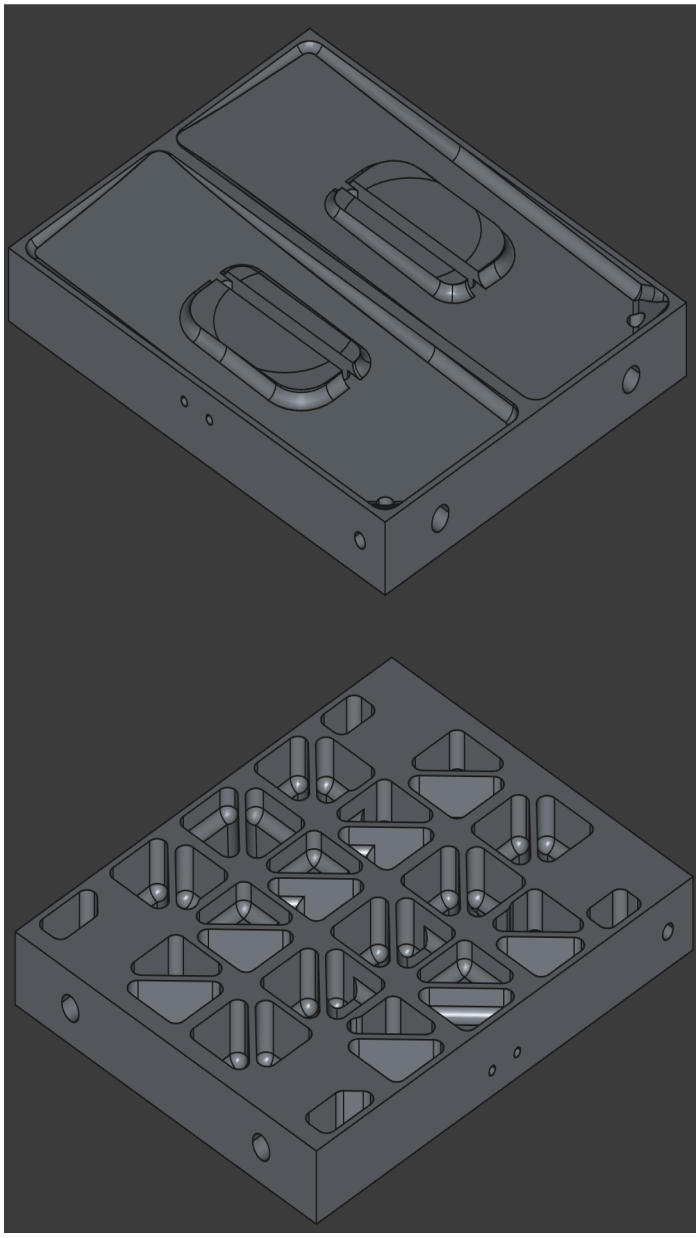

Figure 6.4 The tibial baseplate top and bottom views. The tray's sloped surface for fluid drainage can be seen in the top view. The isogrid structures can be seen in the lower view. Both views are from an isometric perspective.

The tibial base plate required a plate on which to mount it, which would also be reciprocating and so the design made heavy use of the isogrid structures as well, shown in Figure 6.5.

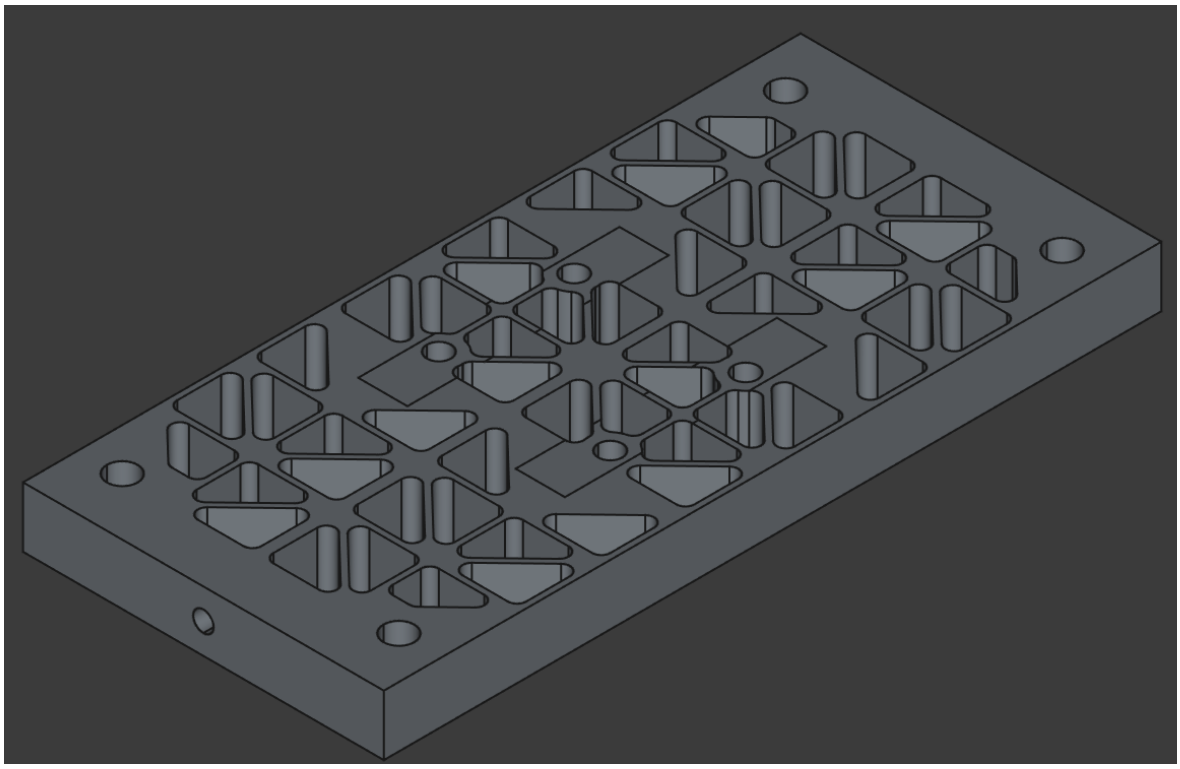

Figure 6.5: The support structure to mount the tibial base plate to, shown in isometric view.

The femoral components needed to be mounted on the flexural shaft, which can be seen running transversely in Figure 6.3. This required an adaptor to be designed; the one designed by the author was a redesign of one a colleague had designed earlier. The current design was also designed to be additively manufactured for ease of replacement if it became damaged and so could act as a sort of mechanical fuse saving the rest of the machine from damage in the case of a control error, or erroneous user input. The front and back of both sides of the design are shown in Figure 6.6.

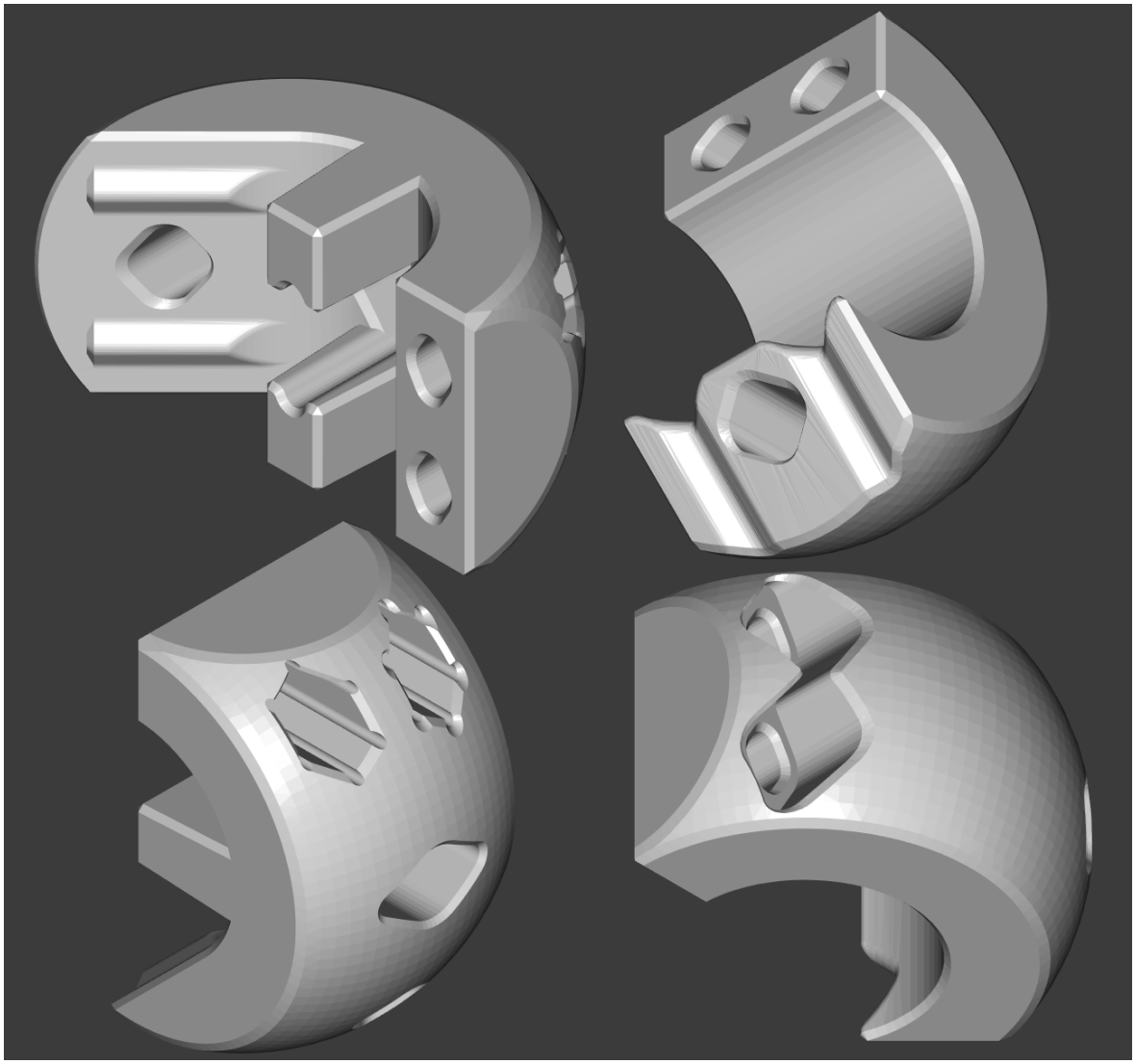

Figure 6.6: Upper left: Femoral component holder side 1 showing its inside (shaft side) features, Lower left: Femoral component holder side 1 showing its outside (femoral component interface side) features. Upper right: Femoral component side 2 showing its inside (shaft side) features, Lower right: Femoral component side 2 showing its outside features.

The tibial baseplate, its support structure, two OUKR tibial components and their bearings are shown integrated into the machine in Figure 6.7.

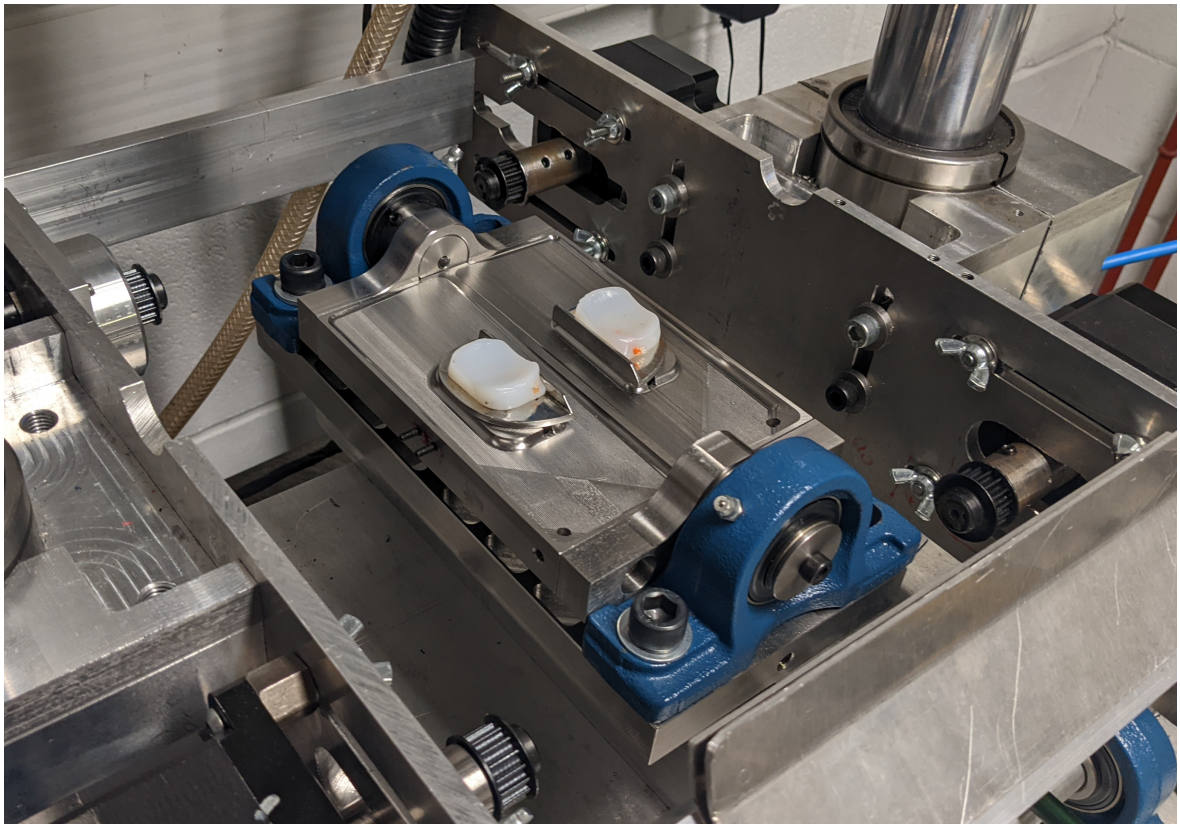

Figure 6.7: The tibial baseplate with two OUKR tibial components and their bearings. The sides of the tibial base plate show the associated fittings designed to hold the baseplate in the pillow bearings. Underneath this is shown the light-weighted support structure.

The fluid support holder is designed to take two pipes and hold them over the femoral component holders, one in each side of the machine test space. The fluid then drips down and flows over the bearing surfaces of the femoral component, being distributed over the bearing and tibial component as well. The design is shown in Figure 6.8.

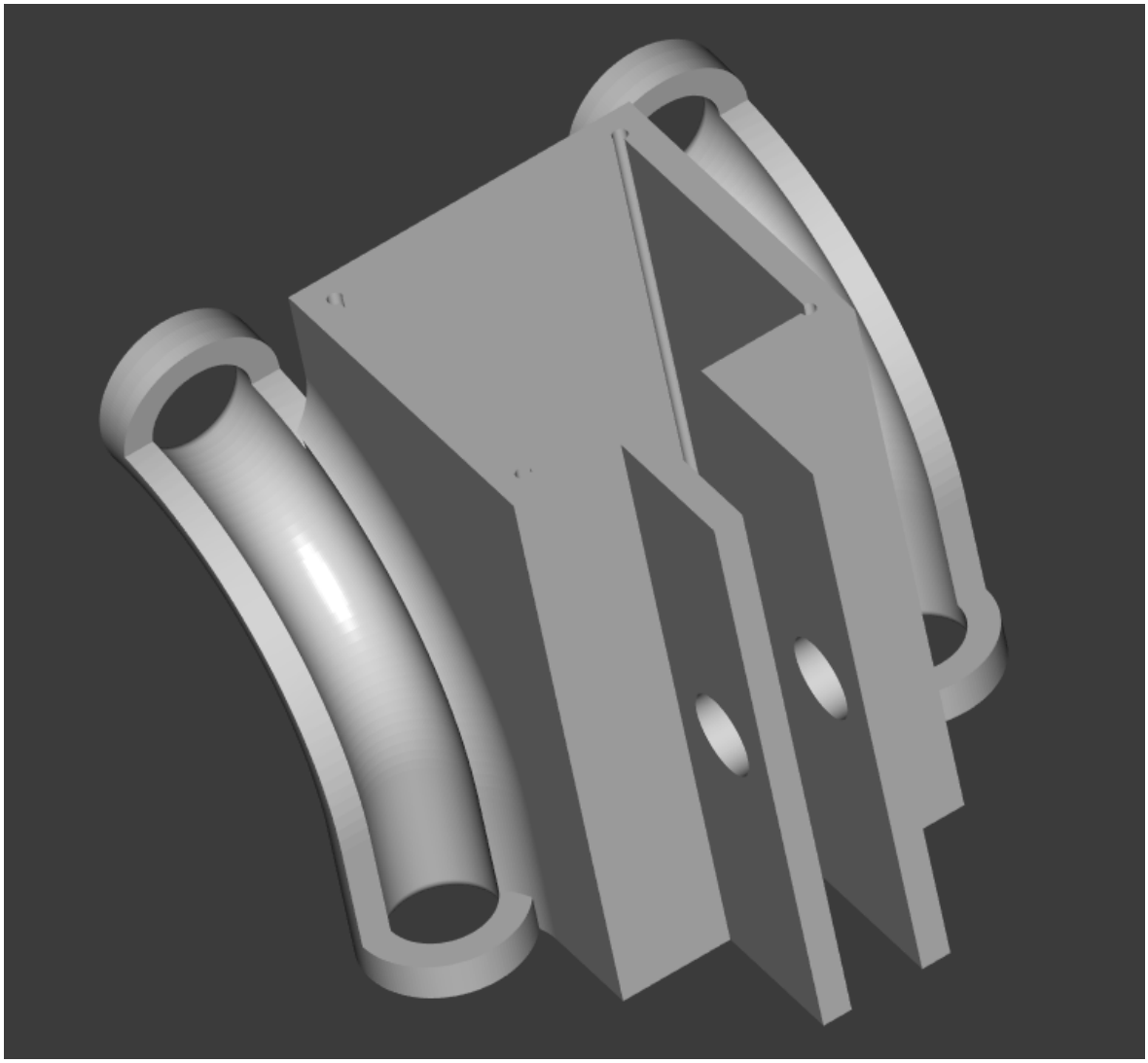

Figure 6.8: Fluid pipe support, shown in isometric view.

The gears were designed to allow the rotation of the flexural axis to be transmited in a ratio of 1:1 to a potentiometer mounted on the side of the movable support structure shown in 6.3. The gears were of a herringbone design for smooth meshing to minimise the transmitted chatter for accurate positional measurement.

The gears were additively manufactured for the low density of the plastic, the design is an improvement of one originally put forward by Heath (2020), with improved gear thickness and added support surfaces for engagement on the flexural shaft and potentiometer shaft. The improved design is shown in Figure 6.9.

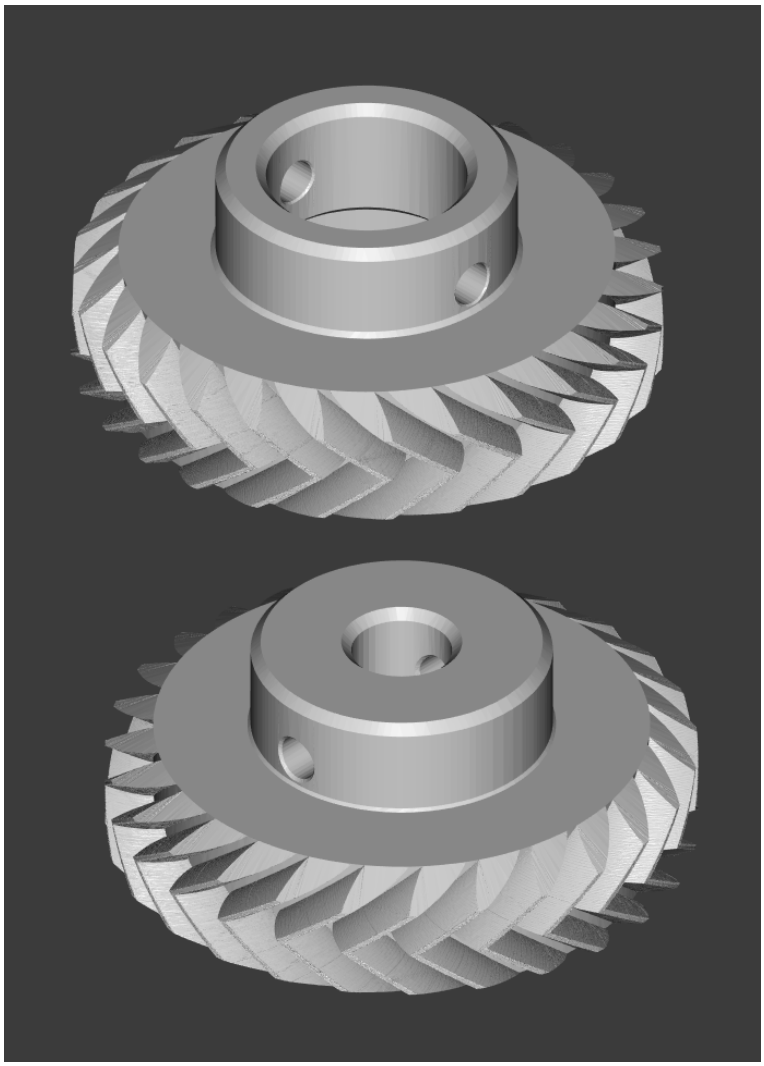

Figure 6.9: The gears to allow measurement of flexural motion. Top: Shaft side gear, Bottom: Potentiometer side gear.

These extra components are shown integrated into the machine in Figure 6.10. The white component holding the fluid pipes was designed by a colleague.

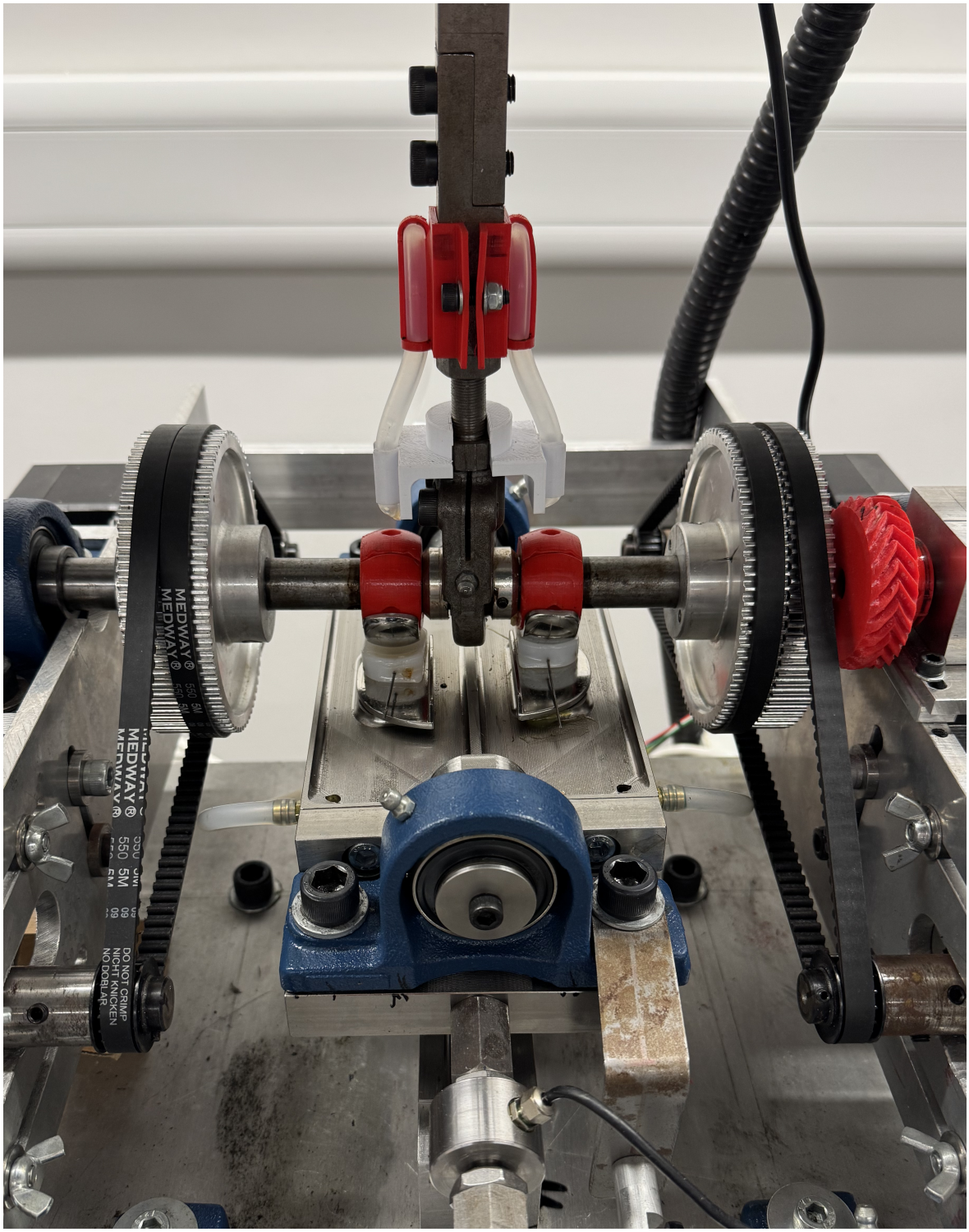

Figure 6.10: The working elements of the machine, showing integration of: the tibial baseplate; the tibial baseplate support structure; the fluid support pipes; and the flexion gearing. Components the Author additively manufactured and designed are shown in a red material. The white component was designed by a colleague.

6.3.2 Constant load lubrication tests

Table 6.1 shows results for the load at which the motors start skipping steps. This varies under different loading conditions, Dry (800N) and Wet (1200). The motor skipping could not be induced under the Oil lubrication condition and the Si Plan maximum load was reached.

Table 6.1: Knee simulator skipping load under lubrication conditions

Lubrication	Constant Load before skipping (N)
Dry	800
Wet	1200
Olive Oil	>7000 demand

For the simulator to achieve the *BS ISO 14243-3* (British Standards Institution, 2014) vertical loading profile, it is required to work, within the required accuracy parameters, under a maximum load of 5.2kN, or 2.6kN in each compartment. The currently proposed machine can achieve this using olive oil as a lubricant between the articulating surfaces. The lubrication system designed to address this was a further bolt-on addition, allowing easy removal for cleaning in the event of biological lubricants being required. However, in certain circumstances, such as a study of bearing ware or rotation, it may be desirable to simulate the effect of a greatly increased frictional coefficient. In these cases the current simulator can be used, but requires a reduction or scaling of the load appropriately. Further, under dry loading conditions the bearings were observed to get noticeably warmer during the test, which may change the specific dynamics of the interaction between bearing and metallic components. Due to this, it is recommended that in conventional use, lubrication is applied to the bearing which allows the standard test loading to be applied. However, the simulator is capable of scaled unconventional loading conditions if required.

6.3.3 Baseline RMS error

The Linear RMS error for a dry bearing is shown to increase with relation to constant load applied (Table 6.2), from 0.483mm at 5N to 0.542mm at 600N. An increase of 12.22%. The RMS error for the flexural axis decreases with increasing constant load, from 5.910deg at 5N to 5.262deg at 600N, a decrease of 10.96%. There was comparably high variability in the flexural error readings at 5N load.

Table 6.2: RMS error at increasing loading under dry lubrication conditions.

Axis	RMS error at 5N constant load	RMS error at 600N constant load
Anterior Posterior (mm)	0.483 (±4.488*10^{-3} 95% CI)	0.542 (±1.490*10^{-3} 95% CI)
Flexion (deg)	5.910 (±0.287 95% CI)	5.262 (±0.073 95% CI)

The baseline error of the knee simulator is 0.483mm RMS error on the anterior-posterior axis and 5.910deg on the flexural axis. In both cases, this error equates to ~10% (9.3% and 10.8%) of the maximum displacement in each axis (5.16mm and 54.75deg respectively). Further, the average RMS over the whole test for the anterior-posterior and rotational axes showed an increase in error under more strenuous loading conditions, (Table 6.2). Specifically, the linear error increases by approximately 12%, a change of 0.06mm. This is similar in magnitude to the measurement error of equipment used in the calibration (±0.04mm). This might suggest that there is effectively little change happening in the machine system from its baseline load to close to its maximum, a good feature for comparative testing. However, the change is statistically significant ($p = 3.679*10^{-5}$) which still indicates that there is a change, however, slight, under increased loading.

The same can be said for the rotational axis (Table 6.2), as the RMS error decreased under increased loading conditions from 5.910 deg at 5N to 5.262deg at 600N, a change of ~0.65deg. This decrease was also statistically significant ($p = 0.025$), indicating that although the change is slight, there is still a shift in error.

6.3.4 Long-term error tests

In Table 6.3, there is an increase in the anterior-posterior axis RMS error (from 0.535mm to 0.641mm) as the maximum load under lubricated conditions increases, and a decrease in flexural axis RMS error (from 5.895deg to 5.533deg) under the same conditions.

Table 6.3: Loading condition and average RMS error between demand and measured

Load and lubrication	Average anterior posterior RMS error (mm)	Average flexural RMS error (deg)
Sinusoidal 400N ± 200N – Dry	0.535	5.895
Sinusoidal 600N ± 300N – Wet	0.548	5.704
BS ISO 14243-3 Load (5.2kN peak load) – Oil	0.641	5.533

The 600N limit on the dry loading (Table 6.3) is below the *BS ISO 14243-3* (British Standards Institution, 2014) load of a 5.2kN rough sinusoid in vertical load. For this study two relatively inert lubricants were used: water, and olive oil. Under lubrication conditions, the loads were able to be raised to a maximum of 1.2kN and 5.2kN respectively. Further, at greater states of lubricity and load the error of the axes shifts, in the anterior-posterior axis increasing by 0.158mm and in the flexural axis decreases by 0.377deg.

The changes observed under maximum loading were both greater (anterior-posterior) and lesser (flexural) than those seen in the maximum loading under dry conditions (Table 6.2), but both in the same direction as the maximum constant load test. This may indicate a more complex relationship of the RMS error to both the lubrication state and the vertical loading condition, which may be an avenue for further exploration in future studies.

In the wider literature, Maletsky *et al.* (2005) designed a research knee simulator as well and showed a repeatable error of ±5% after conditioning cycles and a maximum sensor error of ±7% in measuring loads, which is between 50% and 70% of this machines maximum error. Moreover, commercial testing machines by AMTI state that they have between 5% (AMTI, 2025) and <1% (AMTI, 2022) error on their website and machine specification respectively. Other commercial machines are available but do not provide much information outside of their compliance to one or more of *BS ISO 14243-1* (British Standards Institution, 2009) *BS ISO 14243-3* (British Standards Institution, 2014) respectively (Prosim, 2023, 2025; EndoLab, 2024).

The *BS ISO 14243-3* (British Standards Institution, 2014) standard states that for all loads that the magnitude of the load must be maintained to a tolerance of ±5%, and at the phasing must be held to ±3% of the full cycle, so it can be assumed that these commercial machines meet those requirements. This machine would fall outside of these requirements with an RMS error rate that is roughly double the allowable tolerance of the maximum load. Moreover, the error is comparable to the maximum sensor error of the machine created by Maletsky *et al.* (2005).

Further still, while this machine does have a lubrication system it is unheated at the moment, whereas the offerings by Prosim (Prosim, 2023), AMTI (AMTI, 2022), and EndoLab (EndoLab, 2024) all have temperature controlled lubrication systems making them the superior choices in terms of raw specifications. However, the machine created in this study is likely substantially cheaper than the commercial machines, having an estimated bill of materials cost of ~£10k for add-on parts and the control system. This lower cost and therefore increased accessibility to research institutions means that, in this case, an increased error rate and unheated fluid system is an acceptable trade-off, though naturally this requires a free SI-Plan fatigue machine or similar to accomplish the cost of which is not factored in here. Moreover, even with the current measured error of the machine and the lubrication system limitations, this wear machine is still capable of doing comparative studies between wear conditions, bearing locations, and joint configurations, all of which are useful study areas for further work in this field. However, a goal for future work should be to address the current limitations by lowering the RMS error rate of this machine to within the bounds allowable by the *BS ISO 14243-3* (British Standards Institution, 2014) standard, as well as adding a heated fluid system along side the upgrades to measure micromotion.

6.3.5 Conversion to a micromotion simulator

The future design study that will convert this machine into a micromotion simulator has a comparatively cheap and open, in the intellectual property sense, design to work from. However, there are some limitations imposed by the current design, specifically that the measurements will have to be fitted with consideration to the tibial tray and the floating flexural axis support structure. Conventionally, the Linear Variable differential transformer (LVDT) has been a successful method of measuring implant micromotion, with a reported accuracy of 1µm (1×10^{-3}mm) (Ellenrieder *et al.*, 2020). The LVDT method requires drilling into the bone (or analogue) and attaching the LVDT to the implant which then measures the difference in motion between the bone and implant at their common interface.

In optical methods, there has been research demonstrating the use of RSA for *in vivo* calculation of micromotion under physiological loads (Horsager *et al.*, 2017; Rahman, 2022). However, this method is less accurate than the LVDT method with a range of 0.1mm – 0.2mm (Short *et al.*, 2005; Simpson *et al.*, 2010; van IJsseldijk *et al.*, 2011; Rahman, 2022). Moreover, this method requires the use of bulky equipment that is not suitable for the confines of the machine. Digital image correlation (DIC) is another optical method that has shown good accuracy in experimental settings. Hoult *et al.* (2013) showed a mean error range of between -0.2×10^{-3}mm and 0.8×10^{-3}mm over a 67.9mm analysis circle in a strain test, comparing DIC to conventional foil strain gages, proving to be comparably accurate to the LVDT methodology.

Moreover, DIC only requires a speckle on the implant and bone to track the motion and a camera positioned reliably to track the measurements (McCormick and Lord, 2010; Rahman, 2022), and DIC has also been demonstrated to be a successful method of measuring implant micromotion in experimental results (Berahmani, Janssen and Verdonschot, 2017; Rahman, 2022).

Kohli *et al.* (2021) establishes a limit of 112µm or 0.112mm for micromotion which is lower than the previous limit of 150µm and well within the capability of both the DIC and LVDT methods. The limitation of DIC in relation to LVDT is that the LVDT measures the bone implant interface directly, where as the DIC method is an indirect measurement based on the outside of the bone. This is a fair assumption in the case of a uniform strain field, but that is not the case in micromotion, meaning that the LVDT method is the preferred on from this perpective. Whereas, the LVDT penetrating the bone will likely impact the strain field directly and therefore introduce potential measurement artefacts, favouring the DIC method. It is likely that if both methods can be mounted to the machine, then both will provide good measurements as long as the limitations of each are born in mind.

The mounting of the sensors to the machine poses a challenge, as to achieve accurate results under tibial baseplate motion (AP motion the measuring devices will have to be mounted directly to the tibial base plate, which will require fittings to be designed, increasing the mass of the AP axis and potentially leading to greater RMS error. More concerningly, these are sensitive components which will be subject to forced vibrational loads which may damage them over time and introduce a source of error into the measurements. The LVDT method may have an advantage here, as it is potentially more lightweight in both required fitting design and being closer to the baseplate.

Rahman (2022) used a stock Cannon 4000D with a stock lens, a comparatively bulky solution but one which provided good quality results. The knee machine currently has a smaller camera associated with it, an Svpro 4K Webcam (Amazon UK, 2025), which is used to video experiments. This camera is comparatively lightweight and has a USB feed which also allows direct streaming of images and video to the attached computer. As this camera is smaller, cheaper, and with lower mass, this may be a promising avenue to be included in the future design study if it can be proven to produce comparable results. However, if not, then the LVDT option may be the best option going forward.

In both the DIC and LVDT cases the chosen equipment will be subject to vibrational loads which may negatively effect the measurements taken. However, a full design study will need to be undertaken to select between these options, and to design the mounting hardware for the specific measurement devices selected.

6.4 Conclusion

Under dry loading conditions it has been shown that the machine has a maximum RMS error under load of ~10%, and that this error increases in the AP axis under load and decreases in the flexion axis under the same conditions. This is roughly twice as large as the tolerance measurement tolerance called for in the *BS ISO 14243-3* standard and larger than current commercial offerings. However, this is comparable to the maximum sensor error of other research machines that have been developed (Maletsky and Hillberry, 2005). These were deemed acceptable trade-offs for the comparatively low bill of material cost of the add-on components of the machine and even with these limitations the current machine is capable of conducting useful studies for this field. However, future work on this machine should seek to reduce these limitations to be comparable with current commercial machines as this would enhance the usefulness of the current machine.

The machine is capable of operating under physiological loading conditions represented in the *BS ISO 14243-3* standard with sufficient lubrication (Olive Oil). Therefore, the simulator can be used to investigate and assess the factors which may be of high importance to wear of the OUKR mobile bearing such as: overhang, and motion. Moreover, and critically for this work, the knee machine now serves as a basis for future work which will develop the machine further to enable study of the micromotion of novel fixation geometries under physiologically relevant loads. Depending on the design of this add-on feature, it has been suggested that either the methods of DIC or LVDT are potentially suitable for measurement of micromotion in the context of this machine. These elements combine to fulfil Objective 3. If this future design study is successful. This would allow the further development of the design proposed in Chapter 5 towards a more clinically applicable design, as well as the study of other future designs of novel fixation geometry.

Chapter 7 Conclusions and Contributions

7.1 The problem

The Oxford Unicompartmental Knee Replacement is an effective treatment for antero-medial osteoarthritis of the knee (Goodfellow *et al.*, 2015), which is the commonest form of the disease (FELSON, 1988; UK and London, 2014; Stoddart *et al.*, 2021; Reed *et al.*, 2024). In 2023, 116,845 primary knee replacements of all kinds were carried out in the United Kingdom (Reed *et al.*, 2024), and it is predicted that future numbers of knee replacements will increase (Kurtz *et al.*, 2007). Currently UKR usage is at ~14% as a ratio of all knee replacements (Reed *et al.*, 2024). Moreover, cementless UKR usage from 2004 2023 shows a general trend of increasing usage as a proportion of all knee replacements, a trend which may continue into the future (Reed *et al.*, 2024, p. 186 Table 3.K2). Following the same trend, the cementless version of the OUKR is currently the most common variant of the OUKR in use (Reed *et al.*, 2024). However, while compared to the cemented OUKR the cementless OUKR has a lower overall revision rate. The cementless OUKR still has an increased tibial periprosthetic fracture rate (Mohammad *et al.*, 2021). In western populations, this fracture rate is ~0.2% (Mohammad *et al.*, 2021). This effect is exacerbated in Asian populations with fracture rates between ~7% (涂 *et al.*, 2012; Yudong *et al.*, 2022) and ~8% (Hiranaka *et al.*, 2020). Furthermore, there is a strong sex specific risk with Asian women showing fracture rates between ~10% (涂 *et al.*, 2012; Yudong *et al.*, 2022) and ~11% (Hiranaka *et al.*, 2020). A contributing factor to this may be the bone morphology, the MEL projecting from the tibial shaft has been suggested to hold predictive capability for fracture risk (Yoshikawa *et al.*, 2020), which may be explained from an engineering point of view as the stress generated in cantilever as done in Chapter 1.

It has also been suggested in Chapter 1 that the increased bone removal to form the keel slot required by the current design may remove second moment of area from the tibial plateau section, resulting in higher stress experienced by the material. A possible remedy to these numbers is an alteration to the design of the fixation geometry (Rahman, 2022).

This thesis has attempted to address this key issue by developing an FEA model that is capable of accurately simulating an orthopaedic peg for analysis and optimisation. Then, it is possible to use this model to optimise the peg for primary fixation (pull-out force), and finally, continuing the development of a novel knee wear simulator that will in future integrate micromotion measuring equipment capable of assessing the success of primary fixation of future designs.

7.2 Summary of chapter conclusions

Chapter 2 established that the best material model for simulating primary fixation was a plastic hardening model, as all three plastic hardening models tested (DP1, DP2, and VM) remained within the allowable limit over the clinically relevant interferences in the critical zone. The linear elastic model was capable of accurately simulating the interaction between peg and hole from ~0.3mm to ~0.5mm interference indicating that plastic effects become dominant between ~0.5mm to ~0.7mm interference for a 5.65mm peg. Plastic hardening material models were therefore recommended for use in interferences beyond ~0.5mm for a 5.65mm peg. These models were then further selected between in Chapter 4.

Chapter 3 resulted in the determination of the mechanical material properties that were used in Chapter 4's model. This chapter further demonstrated that the mechanical properties of the sawbones rigid polyurethane foam were dependent on density, largely in accordance with the equations put forward in "Cellular Solids" (Gibson and Ashby, 1997). The coefficients presented ($C_1 = 1.341$, and $C_5 = 0.614$) fell outside the expected values ($C_1 \approx 1.000$, $C_4 \approx 0.050$, and $C_5 \approx 0.300$) which suggested that while the open-cell foam equations may be used with the given coefficients, the closed-cell foam equations may be necessary for a more accurate prediction of the polyurethane foam's property variation with density and a deeper understanding of the foams properties. The C_4 value were closer to the expected values than the C_5 values, this may further suggest that the foams retain a dominant elastic failure mechanism; this is despite half of the samples being considered in the plastic region by the elastic-plastic criterion in Equation 1.7.

Chapter 4 showed that for foams in the range PCF 12 – 20, the DP1 model was useful in clinically relevant interference ranges, and the most accurate model of the three models carried over from Chapter 2. Moreover, this model was much more accurate with the inclusion of element deletion behaviour. There was no difference between fracture energy and fracture displacement criteria. A further development was that of the aspect ratio compensation factors of 5 and 10, which while there was little to distinguish between the two models both allowed the most effective improvement to be demonstrated, that of a uniform structured meshing technique. Which showed a reduction in average error of ~7.4% in the clinically relevant critical zone of 0.6mm to 1.2mm interference, achieving the first objective.

Chapter 5 used the optimal FEA model developed in Chapter 4 to allow the design and evaluation of novel peg geometries for optimising primary fixation. Three aerodynamic nose forms were investigate and compared, the DV, LD, and LV Haack profiles. Each profile was compared at a range of interferences and fineness ratios. The LV Haack was shown to be the optimal nose form due to the competitively flat pull-out force response, with an optimal nose length of 1mm (FR 0.625).

The LV Haack nose was then manufactured and tested in PCF 20 polyurethane foam. From this testing the 3mm (FR 1.875) was shown to be the optimal. A possible reason for this was that the tight radius of the nose may have caused damage that the simulation was unable to capture. Due to this damage, a design limit was proposed that minimum radii in contact with the foam during insertion should be limited to the rate of curvature of a LV Haak 3mm (FR 1.875) nose. Furthermore, this peg compares well to those found in the literature and those from previous chapters, with a higher pull-out force compared to the round nose peg of ~50% and ~60% compared to values in the literature, therefore, achieving the second objective. Even though this improvement came at the cost of a large push-in force, a benefit was still demonstrated with relation to the current keel design and the round nose peg design. A potential reduction of 61% and ~18% in bone stress was shown, caused by the insertion force in comparison to the current keel and round nose peg respectively. Moreover, a corresponding increase in factor of safety of ~157% and ~22% when compared to the current keel design and round nose peg respectively, was shown from using the designed 3mm LV Haack design. These benefits showed strong indications of potentially addressing the very high fracture rates of the Asian woman population caused by the current keel design.

Furthermore, Chapter 5 demonstrated that while the developed simulation is a useful tool in culling the design space comparatively rapidly, it is not yet sufficient to solely predict the optimal design. A number of promising designs must still be run through an experimental validation step to find the final optimal design.

Chapter 6 completed the development a novel knee wear simulator and characterised its properties. This machine was shown to perform similarly to other such research machines under dry loading conditions, but it underperformed in comparison to commercially available machines. Further, under lubricated conditions, it was capable of motion under physiologically representative loading (British Standards Institution, 2014). It was also suggested that the use of DIC or LVDT's equipment could be a possible path forward for a design upgrade to allow the machine to measure micromotion in the new peg design, described in Chapter 5.

7.3 Thesis limitations

Chapter 2 and Chapter 4 presented an FEA model that was able to model the primary fixation of a peg accurately to within 5.40% ± 3.15% 95% CI of the experimental values. However, the same model was not able to model the insertion force accurately. The insertion force of the simulations was very often in the region of ~30% inaccurate. It is possible that the push-in error may be contributed to by the friction value that was set at a constant value of 0.2. It is probable that the pull-out force is dominated by the static coefficient of friction, whereas the push-in force is dominated by the dynamic coefficient of friction. From this it follows that a more advanced approach to modelling the friction coefficient would potentially help with the push-in error discrepancy. However, the coefficient of friction is likely to be only one of the effects that prevents accurate simulation of push-in forces.

Another effect may be that the simulated foam showed oscillations during the push-in stroke and dynamic oscillations may induce temporary high friction scenarios during the periods where the foam returns from an oscillation and effectively “slaps” the peg in a small collision interaction. This is similar to the effect described in Chapter 5, where the foam was seen to be “turned in” and so may pressed harder on the surface of the peg either generally or at a specific location. Both result in the same outcome, a higher normal force induces a higher push-in force. A possible remedy for the oscillations is mass scaling, where the density of a solid is increased. Increasing the effective mass may reduce its dynamic response. However, there is a limit to the mass scaling technique as eventually the solid will cease to behave as the foam would.

The results presented in Chapter 3 of this work should be taken in light of the nuances of the methodology that were previously discussed, in particular that there were only two fresh specimens for the material characterisation of PCF 12, 15, and 25, limiting the significance of the 95% CI values presented. Furthermore, the logarithmic strain conversion was used to produce the true stress graph rather than relying on DIC or some areal compensation and so the actual true stress curve will be at lower values than those presented herein.

Further, there are only four data points presented; it is possible that with more data points, a clearer trend on the behaviour of these foams in the intermediate density region would emerge, though this is also a factor in the rest of the thesis. More information on trends could be drawn from the data had more points been established. However, this was not possible due to time limitations, especially in the case of the simulations conducted in this thesis. Moreover, each experiment costs money both in specimen cost and in machine time. A demonstrative point of this is shown again by Chapter 3, as the "most natural" fit of the graphs would deviate from the equations presented in "Cellular Solids" (Gibson and Ashby, 1997). The equations of best fit presented had to be tested independently to obtain an r^2 value. While this of itself does not invalidate the formulae used, especially considering that the lowest r^2 value was 0.934. It may however, further support the need for more research into foam behaviour in this particular region.

In Chapter 5 lack of defined convergence of the simulations mesh involved in the study may have caused some unreliable pull-out force results. Realistically, the convergence was done with a 1mm nose and at 1.6mm of interference and it took around 2 weeks of simulation time to complete a single simulation at a mesh size of 0.05mm. It is likely that the convergences selected would have shown convergence for the larger meshes. However, this is not certain and ideally more computational resources would be available for computation of smaller meshes so convergence, as defined, could be found.

The accuracy of the photographic measurement method was ~0.1mm, ideally a more capable metrological device would be available to make precise surface measurements to validate the shapes of the peg.

The results of this study were obtained primarily using PCF 20 polyurethane which is somewhat representative of some cancellous bone. However, cancellous bone is a very variable material and the effects of altering material properties on pull-out force are not captured by this experiment. Future studies looking into these pegs may benefit from testing the optimal pegs in cadaveric bone. Furthermore, it may be useful to characterise the effect of altering material modulus and density on the ideal nose form.

As discussed in Chapter 1, bone is not a dry foam. It is filled with bone marrow, which has a number of properties in the context of this thesis. Two important ones are that the poroelastic effects introduced by the incompressible fluid would potentially alter the material properties of the foam making it stiffer, and would contribute to lubricating the peg as it slides in. Both of these effects may alter the results in this study for Chapter 2, Chapter 3, Chapter 4, and Chapter 5. The behaviour of the peg under these considerations is important for understanding the probable behaviour of the peg in a clinical setting. Moreover, the possible implications of this are a potential change in the optimal peg nose, which could shift the conclusions of the study but also shed more light on the relation of the FR to the foam conditions. That would potentially lead to greater understanding and a greater power to design pegs in the future.

In a similar vein, cross validation of the peg behaviour with animal or Cadaveric bone studies is critical to the further validation of the pegs performance and development towards use in clinical settings if any differences are shown, again leading to greater understanding. Bone studies were not done in this study as such studies take a great deal of time and cost to set up, run and, importantly, to dispose of the remains. Further, the results of these studies can be difficult to interpret due to the large variation in bone properties between patients. To overcome the inter-specimen variation, and the anisotropic properties of the bone relative to principal alignment of the trabeculae, further studies would need to be undertaken as well as the insertion study. Only when the specimen specific properties are understood will it possible to link the behaviour of the peg in the insertion studies to the bone properties, and from that make conclusions about the performance of the new peg in a clinical environment.

Moreover, the access to an use of Cadaveric material is understandably tightly controlled. All of these elements present problems to overcome in a validation study, be it Cadaveric or animal bone, and for these reasons validation in bone was not done in the present study.

7.4 Future work

The contributions of this thesis lend themselves to the building blocks of a framework for future development. Specifically a validated finite element model that can predict the pull-out force of a peg, and a novel peg design.

The limited data points in an number of chapters but specifically Chapter 3 were a concern, future studies should aim to fill in more data so that the trends that this thesis has shone light on to can be elucidated further, and spread of the data clarified with more accurate 95% confidence intervals.

In Chapter 1 it was suggested that the removal of material from the tibial section may lead to a decrease in second moment of area of the tibial plateau section which in turn may lead to an increase in the stress which is applied to the material of the tibial plateau. A study of this effect would be very important to quantify the loss of second moment of area in different cut slot and drilled holes and the effect that has on fracture force. A similar loaded to fracture experiment could be done to the work of Rahman (2022), where tibial shaped foam blocks are cut systematically and then the force of fracture is recorded. This would provide more insight into the mechanics at play in risk of fracture due to the loss of second moment of area.

It is proposed that, as in the work of Rahman (2022), where a two peg design was evaluated for primary fixation in both pull-out and micromotion, a two pegged tibial component design be developed from the peg presented in Chapter 5. Which could be followed by a characterisation of the performance of such a two pegged tibial component design for its effect on micromotion under dynamic loading using the novel knee simulator, when the machine is further developed to have the capability assessing micromotion, following the recommendations of this thesis. This would allow more general comparisons with current implant designs. It is also hoped that such a two peg design, while it would take a long time to get through all the validation procedures before being deployed in a clinical setting, would benefit the end patients.

If it were possible to access more computational resources, it would be beneficial for future work to rerun the simulations for Chapter 5, which while useful in their current iteration did not fully converge at the mesh sizes studied. A further mesh study, using smaller elements could be undertaken to establish whether behaviour such as that of the simulated rounded nose 1.6mm flat bottom peg, which matched the pattern of the 1mm LV Haack nose quite well in terms of pattern, was a function of the limited mesh sizes allowable with the currently available computational resources or if the material model itself is incapable of simulating the observed experimental behaviour of the 1mm LV Haack nose cone and to see if the behaviour of the other longer noses changes at the finer meshes.

Moreover, while this work has presented a finite element model that is able to predict the pull-out force of a peg accurately. This was not the case for the push-in force. And so, future work may focus on developing the capability for the simulation to predict push-in forces as well. Further, adaptation to, and validation of the models in cadaveric bone would extend the direct clinical applicability of the FEA model, and would allow the exploration of the post-yield behaviours of trabecular bone in the context of primary fixation. The DP1 parameter set was developed to model nano-indentation in cortical bone, so it is hoped that there is generalizability of this material model to one that could be developed solely by performing a careful mechanical characterisation of cancellous bone, and substituting those values for those of the polyurethane foam, as was done at the end of Chapter 4.

Additionally, if possible, it would be enormously interesting to test the model proposed by Schwiedrzik, *et al.* (2013) and used by Ovesy, *et al.* (2022) to simulate insertion of cementless implants. The effectiveness of the DP1 model could be directly compared in the simulation of these implants in bone. This study would benefit the field as it would help to establish the relative strengths and weaknesses of each model under comparable conditions, consequently leading to a recommendation of the correct model to use for an specific set of requirements.

Finally, the knee wear machine presented in Chapter 6 should be fully developed into a micromotion simulator. Further investigation into the best method of micromotion measurement should be undertaken, selecting between DIC and LVDT methodologies or another as yet unseen better choice. Once the measurement method has been selected, a design should be created to hold the measurement device in place and tested and validated to ensure valid data on the primary fixation micromotion can be obtained. A contributing factor to valid data would be to reduce the error on the machine to a level that is in compliance with the *BS ISO 14243-3 (British Standards Institution, 2014)* standard of 5% of maximum load or displacement.

Ultimately, it is hoped that this current work will contribute to a generalisable model that will allow patient specific implants to be generated and made, tailored to the unique densities and environment of that patient. However, this work is just a small step in that long journey.

7.5 Final conclusions

Each objective that this thesis set out to achieve was met, an FEA simulation based on a Drucker-Prager failure criterion using the parameters defined by Mullins, *et al.* (2009; Toal. V., 2013) has been developed, validated, and optimised with a regular mesh element deletion, ultimately demonstrating an error of 5.40% ± 3.15% 95% CI in relation to the experimental pull-out force data conducted in PCF 20 PU foam. This model was then demonstrated to have useful predictive power for foams of PCF 12, and 15 density showing the model was not over fitted in these cases. Moreover, the model has been used to design a novel peg, optimised for the production of primary fixation that showed strong promise for future development with an increase in the estimated factor of safety of the patients bone during insertion of ~157% compared to the current keel design and ~22% increase over a round nose peg, while retaining the same primary fixation.

The development of a novel knee wear simulator has been completed as the first stage to future integration with micromotion measuring equipment, that will allow future studies into secondary fixation design limitations, as well as to study current limitations of UKRs such as wear.

These contributions show promise for the further development of the Oxford Knee towards a lower fracture risk design that could be implanted into patients, especially Asian patients who suffer under very high fracture rates with the current cementless design. It has been projected that knee replacements will increase in numbers rapidly in the coming years, as will the the proportion of knee replacements that are UKRs, and so this need is a pressing one. Moreover, it is undoubtedly the case that lowing the fracture rate with the proposed low risk design will benefit patients of both sexes and all races, but in particular Asian women stand to gain by far the most from such a design. It is the authors fervent hope that his work helps to address this need.

References

Abdullah, H., Mohd Nor, F. and Abdul Jamil, M.M. (2016) 'Human Bone Histomorphological Pattern Differences Between Genders: A Review', in F. Ibrahim, J. Usman, M.S. Mohktar, and M.Y. Ahmad (eds) *International Conference for Innovation in Biomedical Engineering and Life Sciences*. Singapore: Springer, pp. 183–187. Available at: https://doi.org/10.1007/978-981-10-0266-3_38.

Adam, C.J. and Swain, M.V. (2011) 'The effect of friction on indenter force and pile-up in numerical simulations of bone nanoindentation', *Journal Of The Mechanical Behavior Of Biomedical Materials*, 4(7), pp. 1554–1558. Available at: https://doi.org/10.1016/j.jmbbm.2011.03.026.

AeroScript Programming Language (2024) *Aerotech US*. Available at: http://help.aerotech.com/automation1/Content/AeroScript-Programming-Language.htm (Accessed: 7 October 2024).

Affatato, S. (2016) 'Displacement or Force Control Knee Simulators? Variations in Kinematics and in Wear', *Artificial Organs*, 40(2), pp. 195–201. Available at: https://doi.org/10.1111/aor.12508.

Ahlback, S. (1968) 'Osteoarthrosis of the knee. A radiographic investigation', *Acta Radiol Diagn (Suppl)*, 277, pp. 7–72.

Amazon UK (2025) *Svpro 4K Webcam with 2.8-12mm Varifocal Lens, 4X Optical Zoom Manual Focus USB Camera,IMX317 Sensor UVC Compliant Industrial Camera for Mac/Window/Linux/Android: Amazon.co.uk: Computers & Accessories*. Available at: https://www.amazon.co.uk/dp/B08YJTT6KZ?th=1 (Accessed: 23 September 2025).

American Society for Testing and Materials (2008) 'Standard Specification for Rigid Polyurethane Foam for Use as a Standard Material for Testing Orthopaedic Devices and Instruments - ASTM F1839-08'. Available at: https://doi.org/10.1520/F1839-08R21.

Amstutz, H.C., Campbell, P., Kossovsky, N. and Clarke, I.C. (1992) 'Mechanism and clinical significance of wear debris-induced osteolysis', *Clin Orthop Relat Res*, (276), pp. 7–18.

AMTI (2022) 'ADL Knee Simulator Specifications'. AMTI. Available at: https://www.amti.biz/wp-content/uploads/2022/04/AMTI-Knee-Simulator.pdf (Accessed: 22 September 2025).

AMTI (2025) 'ADL Knee Simulator | Advanced Knee Implant Wear Testing', *AMTI*. Available at: https://www.amti.biz/product/knee-simulator/ (Accessed: 22 September 2025).

Andriacchi, T.P., Stanwyck, T.S. and Galante, J.O. (1986) 'Knee biomechanics and total knee replacement', *The Journal of Arthroplasty*, 1(3), pp. 211–219. Available at: https://doi.org/10.1016/s0883-5403(86)80033-x.

van Arkel, R.J., Ghouse, S., Milner, P.E. and Jeffers, J.R.T. (2018) 'Additive manufactured push-fit implant fixation with screw-strength pull out', *Journal of Orthopaedic Research*, 36(5), pp. 1508–1518. Available at: https://doi.org/10.1002/jor.23771.

Ashman, R.B. and Jae Young Rho (1988) 'Elastic modulus of trabecular bone material', *Journal of Biomechanics*, 21(3), pp. 177–181. Available at: https://doi.org/10.1016/0021-9290(88)90167-4.

Automation1 iSMC Intelligent, Software-Based Motion Controller | Aerotech (2024) *Aerotech US*. Available at: https://www.aerotech.com/product/automation1-software-based-machine-controller/ (Accessed: 7 October 2024).

Automation1 iXI4 Servo Interface with Motion Controller | Aerotech (2024) *Aerotech US*. Available at: https://www.aerotech.com/product/automation1-ixi4-motion-servo-controller/ (Accessed: 7 October 2024).

Bahraminasab, M., Sahari, B.B., Edwards, K.L., Farahmand, F., Jahan, A., Hong, T.S. and Arumugam, M. (2014) 'On the influence of shape and material used for the femoral component pegs in knee prostheses for reducing the problem of aseptic loosening', *Materials & Design*, 55, pp. 416–428. Available at: https://doi.org/10.1016/j.matdes.2013.10.020.

Baker, T.J. (2005) 'Mesh generation: Art or science?', *Progress in Aerospace Sciences*, 41(1), pp. 29–63. Available at: https://doi.org/10.1016/j.paerosci.2005.02.002.

Bayraktar, H.H., Morgan, E.F., Niebur, G.L., Morris, G.E., Wong, E.K. and Keaveny, T.M. (2004) 'Comparison of the elastic and yield properties of human femoral trabecular and cortical bone tissue', *Journal of Biomechanics*, 37(1), pp. 27–35. Available at: https://doi.org/10.1016/S0021-9290(03)00257-4.

Bensusan, J., Davy, D., Heiple, K. and Verdin, P. (1983) 'Tensile, compressive and torsional testing of cancellous bone', *Trans Orthop Res Soc*, 8, p. 132.

Berahmani, S., Janssen, D., van Kessel, S., Wolfson, D., de Waal Malefijt, M., Buma, P. and Verdonschot, N. (2015) 'An experimental study to investigate biomechanical aspects of the initial stability of press-fit implants', *Journal of the Mechanical Behavior of Biomedical Materials*, 42, pp. 177–185. Available at: https://doi.org/10.1016/j.jmbbm.2014.11.014.

Berahmani, S., Janssen, D. and Verdonschot, N. (2017) 'Experimental and computational analysis of micromotions of an uncemented femoral knee implant using elastic and plastic bone material models', *J Biomech*, 61, pp. 137–143. Available at: https://doi.org/10.1016/j.jbiomech.2017.07.023.

Biedermann, A., Kudoke, C., Merten, A., Minogue, E., Rotermund, U., Ebert, H.-P., Heinemann, U., Fricke, J. and Seifert, H. (2001) 'Analysis of Heat Transfer Mechanisms in Polyurethane Rigid Foam', *Journal of Cellular Plastics*, 37(6), pp. 467–483. Available at: https://doi.org/10.1106/KEMU-LH63-V9H2-KFA3.

British Standards Institution (2009) 'BS ISO 14243-1:2009: Implants for surgery. Wear of total knee-joint prostheses. Loading and displacement parameters for wear-testing machines with load control and corresponding environmental conditions for test'. British Standards Institute.

British Standards Institution (2014) 'BS ISO 14243-3:2014: Implants for surgery. Wear of total knee-joint prostheses. Loading and displacement parameters for wear-testing machines with displacement control and corresponding environmental conditions for test'. British Standards Institute.

British Standards Institution (2021) 'Rigid cellular plastics - Determination of compression properties - BS EN ISO 844:2021'. London: British Standards Institution.

Burger, J.A., Jager, T., Dooley, M.S., Zuiderbaan, H.A., Kerkhoffs, G. and Pearle, A.D. (2021) 'Comparable incidence of periprosthetic tibial fractures in cementless and cemented unicompartmental knee arthroplasty: a systematic review and meta-analysis', *Knee Surg Sports Traumatol Arthrosc* [Preprint]. Available at: https://doi.org/10.1007/s00167-021-06449-3.

Burkhart, T.A., Andrews, D.M. and Dunning, C.E. (2013) 'Finite element modeling mesh quality, energy balance and validation methods: A review with recommendations associated with the modeling of bone tissue', *J Biomech*, 46(9), pp. 1477–1488. Available at: https://doi.org/10.1016/j.jbiomech.2013.03.022.

Cabrita, G.J.M., Ferreira, B.S., Silva, C.L. da, Gonçalves, R., Almeida-Porada, G. and Cabral, J.M.S. (2003) 'Hematopoietic stem cells: from the bone to the bioreactor', *Trends in Biotechnology*, 21(5), pp. 233–240. Available at: https://doi.org/10.1016/S0167-7799(03)00076-3.

Calvert, K.L., Trumble, K.P., Webster, T.J. and Kirkpatrick, L.A. (2010) 'Characterization of commercial rigid polyurethane foams used as bone analogs for implant testing', *J Mater Sci Mater Med*, 21(5), pp. 1453–61. Available at: https://doi.org/10.1007/s10856-010-4024-6.

Campi, S., Mellon, S., Ridley, D., Foulke, B., Dodd, C.A.F., Pandit, H. and Murray, D. (2018) 'Optimal interference of the tibial component of the cementless Oxford Unicompartmental Knee Replacement', *Bone & Joint Research*, 7. Available at: https://doi.org/10.1302/2046-3758.73.BJR-2017-0193.R1.

Carnelli, D., Lucchini, R., Ponzoni, M., Contro, R. and Vena, P. (2011) 'Nanoindentation testing and finite element simulations of cortical bone allowing for anisotropic elastic and inelastic mechanical response', *Journal of Biomechanics*, 44(10), pp. 1852–1858. Available at: https://doi.org/10.1016/j.jbiomech.2011.04.020.

Carter, D.R. and Hayes, W.C. (1977) 'The compressive behavior of bone as a two-phase porous structure', *JBJS*, 59(7), p. 954.

Carter, D.R., Schwab, G.H. and Spengler, D.M. (1980) 'Tensile Fracture of Cancellous Bone', *Acta Orthopaedica Scandinavica*, 51(1–6), pp. 733–741. Available at: https://doi.org/10.3109/17453678008990868.

Cheng, F.B., Ji, X.F., Zheng, W.X., Lai, Y., Cheng, K.L., Feng, J.C. and Li, Y.Q. (2010) 'Use of anthropometric data from the medial tibial and femoral condyles to design unicondylar knee prostheses in the Chinese population', *Knee Surgery, Sports Traumatology, Arthroscopy*, 18(3), pp. 352–358. Available at: https://doi.org/10.1007/s00167-009-0876-z.

Choi, K., Kuhn, J.L., Ciarelli, M.J. and Goldstein, S.A. (1990) 'The elastic moduli of human subchondral, trabecular, and cortical bone tissue and the size-dependency of cortical bone modulus', *Journal of Biomechanics*, 23(11), pp. 1103–1113. Available at: https://doi.org/10.1016/0021-9290(90)90003-L.

Clough, R. (1960) 'The finite element method in plane stress analysis', in *Am. Soc. of civ. Eng. 2nd Conference on Electronic Computation*.

Clough, R.W. (1990) 'Original formulation of the finite element method', *Finite Elements in Analysis and Design*, 7(2), pp. 89–101. Available at: https://doi.org/10.1016/0168-874X(90)90001-U.

Cordey, J., Mikuschka-Galgoczy, E., Blümlein, H., Schneider, U. and Perren, S.M. (1979) 'Importance of the friction between plate and bone in the anchoring of plates for osteosynthesis. Determination of the coefficient of metal-bone friction in animal in vivo', *Helvetica Chirurgica Acta*, 46(1–2), pp. 183–187.

Currey, J.D. (1984) *The mechanical adaptations of bones*. Princeton University Press. Available at: https://cir.nii.ac.jp/crid/1570291225160317824.

Da Silva, E.H.P., De Barros, S., Vieira, A.F.C., Da Costa, R.R.C. and Ribeiro, M.L. (2023) 'Accelerated Aging on the Compression Properties of a Green Polyurethane Foam: Experimental and Numerical Analysis', *Polymers*, 15(7), p. 1784. Available at: https://doi.org/10.3390/polym15071784.

Damage evolution and element removal for ductile metals (2024). Available at: https://abaqus-docs.mit.edu/2017/English/SIMACAEMATRefMap/simamat-c-damageevolductile.htm (Accessed: 26 September 2024).

Dassault Systemes (2020) 'Abaqus 2020'. ABAQUS Inc.

Della Rocca, G.J., Leung, K.S. and Pape, H.-C. (2011) 'Periprosthetic Fractures: Epidemiology and Future Projections', *J Orthop Trauma*, 25 Suppl 1(1), pp. S66–S70. Available at: https://doi.org/10.1097/BOT.0b013e31821b8c28.

DesJardins, J.D., Walker, P.S., Haider, H. and Perry, J. (2000) 'The use of a force-controlled dynamic knee simulator to quantify the mechanical performance of total knee replacement designs during functional activity', *Journal of Biomechanics*, 33(10), pp. 1231–1242. Available at: https://doi.org/10.1016/S0021-9290(00)00094-4.

Dyrby, C.O. and Andriacchi, T.P. (2004) 'Secondary motions of the knee during weight bearing and non-weight bearing activities', *J Orthop Res*, 22(4), pp. 794–800. Available at: https://doi.org/10.1016/j.orthres.2003.11.003.

Ellenrieder, M., Souffrant, R., Schulze, C., Mittelmeier, W. and Bader, R. (2020) 'Micromotion and subsidence of a cementless conical fluted stem depending on femoral defect size – A human cadaveric study', *Clinical Biomechanics*, 80, p. 105202. Available at: https://doi.org/10.1016/j.clinbiomech.2020.105202.

EndoLab (2024) 'Knee Simulator - EndoLab', 18 July. Available at: https://endolab.org/simulators/knee-simulator/ (Accessed: 22 September 2025).

Felippa, C. (2012) 'FEM Modeling Mesh, Loads and BCs - Felippa - 2013 - 7 FEM Modeling: Mesh, Loads and BCs Chapter 7: - Studeersnel', in *Introduction to FEM*. TU Delft. Available at: https://www.studeersnel.nl/nl/document/technische-universiteit-delft/introduction-to-the-finite-element-method/fem-modeling-mesh-loads-and-bcs-felippa-2013/10154558 (Accessed: 31 August 2023).

FELSON, D.T. (1988) 'EPIDEMIOLOGY OF HIP AND KNEE OSTEOARTRRITIS', *Epidemiologic Reviews*, 10(1), pp. 1–28. Available at: https://doi.org/10.1093/oxfordjournals.epirev.a036019.

Finnie, I. and Patel, M. (1970) 'Structural features and mechanical properties of rigid cellular plastics(Rigid cellular plastics mechanical properties based on model assuming pentagonal dodecahedron cell form)', *Journal of Materials*, 5, pp. 909–932.

Fish, J. (2010) *Multiscale Methods: Bridging the Scales in Science and Engineering*. OUP Oxford.

Font-Rodriguez, D.E., Scuderi, G.R. and Insall, J.N. (1997) 'Survivorship of Cemented Total Knee Arthroplasty', *Clinical Orthopaedics and Related Research®*, 345, p. 79.

Geraldes, D.M., Hansen, U. and Amis, A.A. (2017) 'Parametric analysis of glenoid implant design and fixation type', *Journal of Orthopaedic Research*, 35(4), pp. 775–784. Available at: https://doi.org/10.1002/jor.23309.

Gersie, T., Bitter, T., Freeman, R., Verdonschot, N. and Janssen, D. (2025) 'Bone stress relaxation in press-fit femoral knee implant fixation: A combined experimental and computational analysis', *Journal of the Mechanical Behavior of Biomedical Materials*, 169, p. 107067. Available at: https://doi.org/10.1016/j.jmbbm.2025.107067.

Gibson, L.J. (1985) 'The mechanical behaviour of cancellous bone', *Journal of Biomechanics*, 18(5), pp. 317–328. Available at: https://doi.org/10.1016/0021-9290(85)90287-8.

Gibson, L.J. and Ashby, M.F. (1997) *Cellular Solids: Structure and Properties*. Cambridge University Press.

Gong, L., Kyriakides, S. and Jang, W.-Y. (2005) 'Compressive response of open-cell foams. Part I: Morphology and elastic properties', *International Journal of Solids and Structures*, 42(5), pp. 1355–1379. Available at: https://doi.org/10.1016/j.ijsolstr.2004.07.023.

Goodfellow, J., O'Connor, J., Pandit, H., Murray, D. and Dodd, C. (2015) *Unicompartmental Arthroplasty with the Oxford Knee*. Goodfellow Publishers, Limited.

Goodfellow, J.W., O'Connor, J.J. and Murray, D.W. (2010) 'A critique of revision rate as an outcome measure: RE-INTERPRETATION OF KNEE JOINT REGISTRY DATA', *The Journal of Bone & Joint Surgery British Volume*, 92-B(12), pp. 1628–1631. Available at: https://doi.org/10.1302/0301-620X.92B12.25193.

Gray, H., Zavatsky, A. and Gill, H. (2010) 'The sclerotic line: why it appears under knee replacements (a study based on the Oxford knee).', *Clinical biomechanics (Bristol, Avon)*, 25(3). Available at: https://doi.org/10.1016/j.clinbiomech.2009.12.002.

Gurkan, U.A. and Akkus, O. (2008) 'The Mechanical Environment of Bone Marrow: A Review', *Ann Biomed Eng*, 36(12), pp. 1978–1991. Available at: https://doi.org/10.1007/s10439-008-9577-x.

Gustafsson, A. (2019) *The role of microstructure for crack propagation in cortical bone*. PhD. Department of Biomedical Engineering, Lund university.

Gustafsson, A., Wallin, M. and Isaksson, H. (2019) 'Age-related properties at the microscale affect crack propagation in cortical bone', *J Biomech*, 95, p. 109326. Available at: https://doi.org/10.1016/j.jbiomech.2019.109326.

Haack, W. (1946) 'Projectile forms of minimum wave resistance', *Douglas Aircraft Co., MC., Rep*, 288.

Haïat, G., Wang, H.-L. and Brunski, J. (2014) 'Effects of Biomechanical Properties of the Bone –Implant Interface on Dental Implant Stability: From In Silico Approaches to the Patient's Mouth', *Annual Review of Biomedical Engineering*, 16(1), pp. 187–213. Available at: https://doi.org/10.1146/annurev-bioeng-071813-104854.

Han, S., Patel, R.V., Ismaily, S.K., Jones, H.L., Gold, J.E. and Noble, P.C. (2021) 'Micromotion and Migration of Cementless Tibial Trays Under Functional Loading Conditions', *The Journal of Arthroplasty*, 36(1), pp. 349–355. Available at: https://doi.org/10.1016/j.arth.2020.07.017.

Hayes, W.C. and Carter, D.R. (1976) 'Postyield behavior of subchondral trabecular bone', *Journal of Biomedical Materials Research*, 10(4), pp. 537–544. Available at: https://doi.org/10.1002/jbm.820100409.

Heath, D. (2020) *Development of a Test Rig for the Acquisition of Valid Wear Data from the Oxford Lateral Unicompartmental Meniscal Bearing: Representative Loading Conditions*. MEng. Oxford Brookes University. Available at: https://doi.org/10.13140/RG.2.2.22106.57283/1.

Hiranaka, T., Yoshikawa, R., Yoshida, K., Michishita, K., Nishimura, T., Nitta, S., Takashiba, K. and Murray, D. (2020) 'Tibial shape and size predicts the risk of tibial plateau fracture after cementless unicompartmental knee arthroplasty in Japanese patients', *Bone Joint J*, 102-B(7), pp. 861–867. Available at: https://doi.org/10.1302/0301-620X.102B7.BJJ-2019-1754.R1.

Horsager, K., Kaptein, B.L., Rømer, L., Jørgensen, P.B. and Stilling, M. (2017) 'Dynamic RSA for the evaluation of inducible micromotion of Oxford UKA during step-up and step-down motion', *Acta Orthopaedica*, 88(3), pp. 275–281. Available at: https://doi.org/10.1080/17453674.2016.1274592.

Horsager, K., Madsen, F., Odgaard, A., Fink Jepsen, C., Romer, L., Kristensen, P.W., Kaptein, B.L., Soballe, K. and Stilling, M. (2019) 'Similar polyethylene wear between cemented and cementless Oxford medial UKA: a 5-year follow-up randomized controlled trial on 79 patients using radiostereometry', *Acta Orthop*, 90(1), pp. 67–73. Available at: https://doi.org/10.1080/17453674.2018.1543757.

Hoult, N.A., Andy Take, W., Lee, C. and Dutton, M. (2013) 'Experimental accuracy of two dimensional strain measurements using Digital Image Correlation', *Engineering Structures*, 46, pp. 718–726. Available at: https://doi.org/10.1016/j.engstruct.2012.08.018.

Hrennikoff, A. (1941) 'Solution of problems of elasticity by the framework method', *Journal of Applied Mechanics*, pp. 169–175.

Huybrechts, S. and Meink, T.E. (1997) 'Advanced grid stiffened structures for the next generation of launch vehicles', in *1997 IEEE Aerospace Conference*. *1997 IEEE Aerospace Conference*, Snowmass, CO, USA: IEEE, pp. 263–270 vol.1. Available at: https://doi.org/10.1109/AERO.1997.574417.

Hvid, I., Bentzen, S.M., Linde, F., Mosekilde, L. and Pongsoipetch, B. (1989) 'X-ray quantitative computed tomography: The relations to physical properties of proximal tibial trabecular bone specimens', *Journal of Biomechanics*, 22(8), pp. 837–844. Available at: https://doi.org/10.1016/0021-9290(89)90067-5.

Hvid, I., Christensen, P., Søndergaard, J., Christensen, P.B. and Larsen, C.G. (1983) 'Compressive Strength of Tibial Cancellous Bone: Instron® and Osteopenetrometer Measurements in an Autopsy Material', *Acta Orthopaedica*, pp. 819–825. Available at: https://doi.org/10.3109/17453678308992915.

van IJsseldijk, E.A., Valstar, E.R., Stoel, B.C., Nelissen, R.G.H.H., Reiber, J.H.C. and Kaptein, B.L. (2011) 'The robustness and accuracy of in vivo linear wear measurements for knee prostheses based on model-based RSA', *Journal of Biomechanics*, 44(15), pp. 2724–2727. Available at: https://doi.org/10.1016/j.jbiomech.2011.08.013.

Jakobi, A., Schulze, C., Zietz, C., Souffrant, R., Bader, R. and Kluess, D. (2021) 'Computational modelling of cementless cup fixation in total hip arthroplasty (THA)', in *Computational Modelling of Biomechanics and Biotribology in the Musculoskeletal System*. Elsevier, pp. 397–414. Available at: https://doi.org/10.1016/B978-0-12-819531-4.00015-8.

Jasty, M., Bragdon, C., Burke, D., O ' Connor, D., Lowenstein, J.A.Y. and Harris, W.H. (1997) 'In Vivo Skeletal Responses to Porous-Surfaced Implants Subjected to Small Induced Motions', *J Bone Joint Surg Am*, 79(5), pp. 707–14. Available at: https://doi.org/10.2106/00004623-199705000-00010.

Jyoti and Ghosh, R. (2023a) 'A combined FE-hybrid MCDM framework for improving the performance of the conical stem tibial design for TAR with the addition of pegs', *Computer Methods and Programs in Biomedicine*, 237, p. 107574. Available at: https://doi.org/10.1016/j.cmpb.2023.107574.

Jyoti and Ghosh, R. (2023b) 'The role of the depth of resection of the distal tibia on biomechanical performance of the tibial component for TAR: A finite element analysis with three implant designs', *Medical Engineering & Physics*, 119, p. 104034. Available at: https://doi.org/10.1016/j.medengphy.2023.104034.

Kelly, N., Cawley, D.T., Shannon, F.J. and McGarry, J.P. (2013) 'An investigation of the inelastic behaviour of trabecular bone during the press-fit implantation of a tibial component in total knee arthroplasty', *Medical Engineering & Physics*, 35(11), pp. 1599–1606. Available at: https://doi.org/10.1016/j.medengphy.2013.05.007.

Kelly, N., Harrison, N.M., McDonnell, P. and McGarry, J.P. (2013) 'An experimental and computational investigation of the post-yield behaviour of trabecular bone during vertebral device subsidence', *Biomech Model Mechanobiol*, 12(4), pp. 685–703. Available at: https://doi.org/10.1007/s10237-012-0434-3.

Kelly, N. and McGarry, J.P. (2012) 'Experimental and numerical characterisation of the elasto-plastic properties of bovine trabecular bone and a trabecular bone analogue', *Journal Of The Mechanical Behavior Of Biomedical Materials*, 9, pp. 184–197. Available at: https://doi.org/10.1016/j.jmbbm.2011.11.013.

Kendrick, B.J.L., Simpson, D.J., Kaptein, B.L., Valstar, E.R., Gill, H.S., Murray, D.W. and Price, A.J. (2011) 'Polyethylene wear of mobile-bearing unicompartmental knee replacement at 20 years', *The Journal of Bone & Joint Surgery British Volume*, 93-B(4), pp. 470–475. Available at: https://doi.org/10.1302/0301-620x.93b4.25605.

Kohli, N., Ho, S., Brown, S.J., Sawadkar, P., Sharma, V., Snow, M. and García-Gareta, E. (2018) 'Bone remodelling in vitro: Where are we headed?: -A review on the current understanding of physiological bone remodelling and inflammation and the strategies for testing biomaterials in vitro', *Bone*, 110, pp. 38–46. Available at: https://doi.org/10.1016/j.bone.2018.01.015.

Kohli, N., Stoddart, J.C. and Van Arkel, R.J. (2021) 'The limit of tolerable micromotion for implant osseointegration: a systematic review', *Scientific reports*, 11(1). Available at: https://doi.org/10.1038/s41598-021-90142-5.

Küçükdurmaz, F., Tuncay, İ., Elmadag, M. and Tuncer, N. (2014) 'Morphometry of the medial tibial plateau in Turkish knees: correlation to the current tibial components of unicompartmental knee arthroplasty', *Acta Orthopaedica et Traumatologica Turcica*, 48(2), pp. 147–151. Available at: https://doi.org/10.3944/AOTT.2014.3006.

Kurtz, S., Ong, K., Lau, E., Mowat, F. and Halpern, M. (2007) 'Projections of Primary and Revision Hip and Knee Arthroplasty in the United States from 2005 to 2030', *JBJS*, 89(4), p. 780. Available at: https://doi.org/10.2106/JBJS.F.00222.

Lafortune, M.A., Cavanagh, P.R., Sommer, H.J. and Kalenak, A. (1992) 'Three-dimensional kinematics of the human knee during walking', *Journal of Biomechanics*, 25(4), pp. 347–357. Available at: https://doi.org/10.1016/0021-9290(92)90254-X.

Laurencin, C.T., Zelicof, S.B., Scott, R.D. and Ewald, F.C. (1991) 'Unicompartmental Versus Total Knee Arthroplasty in the Same Patient.', *Clinical Orthopaedics and Related Research (1976-2007)*, 273, p. 151.

Li, M., Lai, C., Zheng, Q., Han, B., Wu, H. and Fan, H. (2019) 'Design and mechanical properties of hierarchical isogrid structures validated by 3D printing technique', *Materials & Design*, 168, p. 107664. Available at: https://doi.org/10.1016/j.matdes.2019.107664.

Liddle, A.D., Judge, A., Pandit, H. and Murray, D.W. (2014) 'Adverse outcomes after total and unicompartmental knee replacement in 101 330 matched patients: a study of data from the National Joint Registry for England and Wales', *The Lancet*, 384(9952), pp. 1437–1445. Available at: https://doi.org/10.1016/S0140-6736(14)60419-0.

Linde, F., Hvid, I. and Pongsoipetch, B. (1989) 'Energy absorptive properties of human trabecular bone specimens during axial compression', *Journal of Orthopaedic Research*, 7(3), pp. 432–439. Available at: https://doi.org/10.1002/jor.1100070316.

Linde, F., Nørgaard, P., Hvid, I., Odgaard, A. and Søballe, K. (1991) 'Mechanical properties of trabecular bone. Dependency on strain rate', *Journal of Biomechanics*, 24(9), pp. 803–809. Available at: https://doi.org/10.1016/0021-9290(91)90305-7.

Liu, W.K., Li, S. and Park, H.S. (2022) 'Eighty Years of the Finite Element Method: Birth, Evolution, and Future', *Archives of Computational Methods in Engineering*, 29(6), pp. 4431–4453. Available at: https://doi.org/10.1007/s11831-022-09740-9.

Lu, F., Zhang, Q., Liu, P. and Guo, W. (2020) 'Anthropometry of the medial tibial plateau in the Chinese population: the morphometric analysis and adaptability with Oxford Phase III tibial components', *Knee Surgery, Sports Traumatology, Arthroscopy*, 28(9), pp. 3048–3054. Available at: https://doi.org/10.1007/s00167-019-05777-9.

Ma, T., Tu, Y.-H., Xue, H.-M., Wen, T. and Cai, M.-W. (2015) 'Clinical Outcomes and Risks of Single-stage Bilateral Unicompartmental Knee Arthroplasty via Oxford Phase III', *Chinese Medical Journal*, 128(21), pp. 2861–2865. Available at: https://doi.org/10.4103/0366-6999.168042.

MacAulay, A., Rahman, A., Marks, L., Murray, D.W. and Mellon, S.J. (2024) 'A finite element model for investigating the influence of keel design and position on unicompartmental knee replacement cementless tibial component fixation', *Medical Engineering & Physics*, 125, p. 104119. Available at: https://doi.org/10.1016/j.medengphy.2024.104119.

Maletsky, L.P. and Hillberry, B.M. (2005) 'Simulating Dynamic Activities Using a Five-Axis Knee Simulator', *Journal of Biomechanical Engineering*, 127(1), pp. 123–133. Available at: https://doi.org/10.1115/1.1846070.

Martin, B.R., Pegg, E.C., van Duren, B.H., Mohammad, H.R., Pandit, H.G., Mellon, S.J. and Murray, D.W. (2019) 'Posterior Bearing Overhang Following Medial and Lateral Mobile Bearing Unicompartmental Knee Replacements', *J Orthop Res*, 37(9), pp. 1938–1945. Available at: https://doi.org/10.1002/jor.24339.

Martins, J.R.R.A. and Lambe, A.B. (2013) 'Multidisciplinary Design Optimization: A Survey of Architectures', *AIAA Journal*, 51(9), pp. 2049–2075. Available at: https://doi.org/10.2514/1.J051895.

MathWorks (2020) 'MATLAB'. Natick, Massachusetts, USA: The MathWorks, Inc.

Matsen, F.A.I., Clinton, J., Lynch, J., Bertelsen, A. and Richardson, M.L. (2008) 'Glenoid Component Failure in Total Shoulder Arthroplasty', *JBJS*, 90(4), p. 885. Available at: https://doi.org/10.2106/JBJS.G.01263.

Mayya, A., Banerjee, A. and Rajesh, R. (2016) 'Haversian microstructure in bovine femoral cortices: An adaptation for improved compressive strength', *Materials Science and Engineering: C*, 59, pp. 454–463. Available at: https://doi.org/10.1016/j.msec.2015.10.047.

McCormick, N. and Lord, J. (2010) 'Digital Image Correlation', *Materials Today*, 13(12), pp. 52–54. Available at: https://doi.org/10.1016/S1369-7021(10)70235-2.

McElhaney, J.H., Fogle, J.L., Melvin, J.W., Haynes, R.R., Roberts, V.L. and Alem, N.M. (1970) 'Mechanical properties of cranial bone', *Journal of Biomechanics*, 3(5), pp. 495–511. Available at: https://doi.org/10.1016/0021-9290(70)90059-X.

Microsoft Corporation (2021) 'Microsoft Excel'.

Milovanovic, P., Potocnik, J., Djonic, D., Nikolic, S., Zivkovic, V., Djuric, M. and Rakocevic, Z. (2012) 'Age-related deterioration in trabecular bone mechanical properties at material level: Nanoindentation study of the femoral neck in women by using AFM', *Experimental Gerontology*, 47(2), pp. 154–159. Available at: https://doi.org/10.1016/j.exger.2011.11.011.

Mises, R. v (1913) 'Mechanik der festen Körper im plastisch-deformablen Zustand', *Nachrichten von der Gesellschaft der Wissenschaften zu Göttingen, Mathematisch-Physikalische Klasse*, 1913, pp. 582–592.

Mises, R.V. (1928) 'Mechanik der plastischen Formänderung von Kristallen', *ZAMM - Journal of Applied Mathematics and Mechanics / Zeitschrift für Angewandte Mathematik und Mechanik*, 8(3), pp. 161–185. Available at: https://doi.org/10.1002/zamm.19280080302.

Mohammad, H.R., Bullock, G.S., Kennedy, J.A., Mellon, S.J., Murray, D. and Judge, A. (2021) 'Cementless unicompartmental knee replacement achieves better ten-year clinical outcomes than cemented: a systematic review', *Knee Surgery, Sports Traumatology, Arthroscopy* [Preprint]. Available at: https://doi.org/10.1007/s00167-020-06091-5.

Mohammad, H.R., Campi, S., Murray, D. and Mellon, S. (2018) 'Instruments to reduce the risk of tibial fracture following cementless unicompartmental knee replacement', *Knee*, 25(6), pp. 988–996. Available at: https://doi.org/10.1016/j.knee.2018.09.001.

Mullins, L.P., Bruzzi, M.S. and McHugh, P.E. (2009) 'Calibration of a constitutive model for the post-yield behaviour of cortical bone', *Journal Of The Mechanical Behavior Of Biomedical Materials*, 2(5), pp. 460–470. Available at: https://doi.org/10.1016/j.jmbbm.2008.11.003.

Netter, J., Hermida, J.C., D'Alessio, J., Kester, M. and D'Lima, D.D. (2015) 'Effect of Polyethylene Crosslinking and Bearing Design on Wear of Unicompartmental Arthroplasty', *The Journal of Arthroplasty*, 30(8), pp. 1430–1433. Available at: https://doi.org/10.1016/j.arth.2015.03.026.

Ngai, V. and Wimmer, M.A. (2009) 'Kinematic evaluation of cruciate-retaining total knee replacement patients during level walking: a comparison with the displacement-controlled ISO standard', *J Biomech*, 42(14), pp. 2363–8. Available at: https://doi.org/10.1016/j.jbiomech.2009.06.030.

Ovesy, M., Aeschlimann, M. and Zysset, P.K. (2020) 'Explicit finite element analysis can predict the mechanical response of conical implant press-fit in homogenized trabecular bone', *J Biomech*, 107, p. 109844. Available at: https://doi.org/10.1016/j.jbiomech.2020.109844.

Ovesy, M., Indermaur, M. and Zysset, P.K. (2019) 'Prediction of insertion torque and stiffness of a dental implant in bovine trabecular bone using explicit micro-finite element analysis', *Journal Of The Mechanical Behavior Of Biomedical Materials*, 98, pp. 301–310. Available at: https://doi.org/10.1016/j.jmbbm.2019.06.024.

Ovesy, M., Silva-Henao, J.D., Fletcher, J.W.A., Gueorguiev, B., Zysset, P.K. and Varga, P. (2022) 'Non-linear explicit micro-FE models accurately predict axial pull-out force of cortical screws in human tibial cortical bone', *Journal Of The Mechanical Behavior Of Biomedical Materials*, 126, p. 105002. Available at: https://doi.org/10.1016/j.jmbbm.2021.105002.

Pandit, H., Jenkins, C., Gill, H.S., Barker, K., Dodd, C.A. and Murray, D.W. (2011) 'Minimally invasive Oxford phase 3 unicompartmental knee replacement: results of 1000 cases', *J Bone Joint Surg Br*, 93(2), pp. 198–204. Available at: https://doi.org/10.1302/0301-620X.93B2.25767.

Pandit, H., Murray, D., Dodd, C.A., Deo, S., Waite, J., Goodfellow, J. and Gibbons, C.L. (2007) 'Medial tibial plateau fracture and the Oxford unicompartmental knee', *Orthopedics*, 30.

Pandit, H., Van Duren, B.H., Gallagher, J.A., Beard, D.J., Dodd, C.A.F., Gill, H.S. and Murray, D.W. (2008) 'Combined anterior cruciate reconstruction and Oxford unicompartmental knee arthroplasty: In vivo kinematics', *The Knee*, 15(2), pp. 101–106. Available at: https://doi.org/10.1016/j.knee.2007.11.008.

Parithimarkalaignan, S. and Padmanabhan, T.V. (2013) 'Osseointegration: An Update', *The Journal of Indian Prosthodontic Society*, 13(1), pp. 2–6. Available at: https://doi.org/10.1007/s13191-013-0252-z.

Pegg, E., Murray, D., Pandit, H.G., O'Connor, J.J. and Gill, H.S. (2013) 'Fracture of mobile unicompartmental knee bearings: a parametric finite element study', *Proceedings of the Institution of Mechanical Engineers. Part H, Journal of engineering in medicine*, 227. Available at: https://doi.org/10.1177/0954411913494326.

Pegg, E., Pandit, H., Gill, H., Keys, G.W., Svard, U.G., O'Connor, J.J. and Murray, D. (2011) 'Examination of ten fractured Oxford unicompartmental knee bearings', *The Journal of bone and joint surgery. British volume*, 93. Available at: https://doi.org/10.1302/0301-620x.93b12.27408.

Pegg, E.C., Bare, J., Gill, H.S., Pandit, H.G., O'Connor, J.J., Murray, D.W. and Price, A.J. (2015) 'Influence of consciousness, muscle action and activity on medial condyle translation after Oxford unicompartmental knee replacement', *Knee*, 22(6), pp. 646–52. Available at: https://doi.org/10.1016/j.knee.2015.09.017.

Pegg, E.C., Walter, J., D'Lima, D.D., Fregly, B.J., Gill, H.S. and Murray, D.W. (2020) 'Minimising tibial fracture after unicompartmental knee replacement: A probabilistic finite element study', *Clin Biomech (Bristol, Avon)*, 73, pp. 46–54. Available at: https://doi.org/10.1016/j.clinbiomech.2019.12.014.

Perkins, E.W., Jorgensen, L.H. and Sommer, S.C. (1958) *Investigation of the Drag of Various Axially Symmetric Nose Shapes of Fineness Ratio 3 for Mach Numbers from 1.24 to 7.4*. Technical Report REPORT 1386. Ames Aeronautical Laboratory: NACA. Available at: https://ntrs.nasa.gov/citations/19930091022 (Accessed: 29 November 2024).

Prada, D.M., Galvis, A.F., Miller, J., Foster, J.M. and Zavaglia, C. (2022) 'Multiscale stiffness characterisation of both healthy and osteoporotic bone tissue using subject-specific data', *Journal of the Mechanical Behavior of Biomedical Materials*, 135, p. 105431. Available at: https://doi.org/10.1016/j.jmbbm.2022.105431.

Price, A., Rees, J., Beard, D.J., Gill, R.H., Dodd, C.A. and Murray, D.M. (2004) 'Sagittal plane kinematics of a mobile-bearing unicompartmental knee arthroplasty at 10 years: a comparative in vivo fluoroscopic analysis', *Journal of Arthroplasty*, 19. Available at: https://doi.org/10.1016/j.arth.2003.12.082.

Price, A.J., Short, A., Kellett, C., Beard, D., Gill, H., Pandit, H., Dodd, C.A. and Murray, D.W. (2005) 'Ten-year in vivo wear measurement of a fully congruent mobile bearing unicompartmental knee arthroplasty', *J Bone Joint Surg Br*, 87(11), pp. 1493–7. Available at: https://doi.org/10.1302/0301-620X.87B11.16325.

Prosim (2023) 'The Prosim Knee Wear Simulator: Machine Specification'. Prosim. Available at: https://www.prosim.co.uk/wp-content/uploads/2023/03/Machine-Spec-Knee-Wear-Sim-v1.pdf (Accessed: 22 September 2025).

Prosim (2025) 'The Prosim Knee Joint Wear Simulator', *Prosim*. Available at: https://www.prosim.co.uk/products/prosim-knee-wear-simulator/ (Accessed: 26 June 2024).

Raffa, M.L., Nguyen, V.-H., Hernigou, P., Flouzat-Lachaniette, C.-H. and Haiat, G. (2021) 'Stress shielding at the bone-implant interface: Influence of surface roughness and of the bone-implant contact ratio', *Journal of Orthopaedic Research*, 39(6), pp. 1174–1183. Available at: https://doi.org/10.1002/jor.24840.

Rahman, A.S.S. (2022) *Assessing and improving clinical outcomes of the cementless Oxford unicompartmental knee replacement tibial component*. DPhil. University of Oxford. Available at: https://ora.ox.ac.uk/objects/uuid:2f3f8132-224c-410a-a531-21c37199fdcc (Accessed: 30 August 2023).

Reed, M., Achakri, H., Bridgens, J., Brittain, R., Howard, P., Wilkinson, M., Wilton, T., Pegg, D., Dawson-Bowling, S., Craig, R., Esler, C., Goldberg, A., Hamoodi, Z., Jameson, S., Porteous, A., Watts, A., Young, E., Boulton, C., Spoerry, J., Taylor, D., McCormack, V., Newell, C., Royall, M., Swanson, M., Ben-Shlomo, Y., Blom, A., Clark, E., Deere, K., Evans, J., Gregson, C., Jones, T., Judge, A., Lenguerrand, E., Marques, E., Nduru, M., Porter, M., Price, A., Rees, J., Sayers, A. and Whitehouse, M. (2024) *NJR 21st Annual Report 2024*. Annual Registry Report 21. National Joint Registry. Available at: https://reports.njrcentre.org.uk/Portals/0/PDFdownloads/NJR%2021st%20Annual%20Report%202024.pdf.

Roff, W. and Scott, J. (1971) *Fibres, Films, Plastics and Rubbers: A handbook of common polymers*. Butterworth-Heinemann, Oxford.

Rothwell, A., Taylor, J., Wright, M., Devane, P., Tobin, H., Denham, P., Henwood, A., Miles, K., Hobbs, T. and Frampton, C. (2009) *The New Zealand Joint Registry. Ten year report. January 1999 to December 2008*. Registry Report. The New Zealand Joint Registry. Available at: https://www.nzoa.org.nz/sites/default/files/NJR%2010%20Year%20Report.pdf (Accessed: 13 August 2025).

Rougraff, B.T., Heck, D.A. and Gibson, A.E. (1991) 'A Comparison of Tricompartmental and Unicompartmental Arthroplasty for the Treatment of Gonarthrosis', *Clinical Orthopaedics and Related Research®*, 273, p. 157.

Rueden, C.T., Schindelin, J., Hiner, M.C., DeZonia, B.E., Walter, A.E., Arena, E.T. and Eliceiri, K.W. (2017) 'ImageJ2: ImageJ for the next generation of scientific image data', *BMC Bioinformatics*, 18(1), p. 529. Available at: https://doi.org/10.1186/s12859-017-1934-z.

Runkle, J.C. and Pugh, J. (1975) 'The micro-mechanics of cancellous bone. II. Determination of the elastic modulus of individual trabeculae by a buckling analysis', *Bulletin of the Hospital for Joint Diseases*, 36(1), pp. 2–10.

Sawbones (2022) *Block, Solid Foam, 20 PCF, 40 mm Thick*. Available at: https://www.sawbones.com/block-20-40-x-130-x-180mm-1522-03.html.

Schileo, E., Taddei, F., Cristofolini, L. and Viceconti, M. (2008) 'Subject-specific finite element models implementing a maximum principal strain criterion are able to estimate failure risk and fracture location on human femurs tested in vitro', *J Biomech*, 41(2), pp. 356–67. Available at: https://doi.org/10.1016/j.jbiomech.2007.09.009.

Schulze, C., Vogel, D., Sander, M. and Bader, R. (2019) 'Calibration of crushable foam plasticity models for synthetic bone material for use in finite element analysis of acetabular cup deformation and primary stability', *Computer Methods in Biomechanics and Biomedical Engineering*, 22(1), pp. 25–37. Available at: https://doi.org/10.1080/10255842.2018.1524884.

Schwiedrzik, J.J., Wolfram, U. and Zysset, P.K. (2013) 'A generalized anisotropic quadric yield criterion and its application to bone tissue at multiple length scales', *Biomech Model Mechanobiol*, 12(6), pp. 1155–68. Available at: https://doi.org/10.1007/s10237-013-0472-5.

scikit-learn (2025) *scikit-learn: machine learning in Python — scikit-learn 1.7.2 documentation*. Available at: https://scikit-learn.org/stable/index.html (Accessed: 20 October 2025).

Sharkey, P.F., Hozack, W.J., Rothman, R.H., Shastri, S. and Jacoby, S.M. (2002) 'Why Are Total Knee Arthroplasties Failing Today?', *Clinical Orthopaedics and Related Research®*, 404, p. 7.

Shichman, I., Roof, M., Askew, N., Nherera, L., Rozell, J.C., Seyler, T.M. and Schwarzkopf, R. (2023) 'Projections and Epidemiology of Primary Hip and Knee Arthroplasty in Medicare Patients to 2040-2060', *JBJS Open Access*, 8(1), p. e22.00112. Available at: https://doi.org/10.2106/JBJS.OA.22.00112.

Short, A., Gill, H.S., Marks, B., Waite, J.C., Kellett, C.F., Price, A.J., O'Connor, J.J. and Murray, D.W. (2005) 'A novel method for in vivo knee prosthesis wear measurement', *Journal of Biomechanics*, 38(2), pp. 315–322. Available at: https://doi.org/10.1016/j.jbiomech.2004.02.023.

Simmons, C.A., Meguid, S.A. and Pilliar, R.M. (2001a) 'Differences in osseointegration rate due to implant surface geometry can be explained by local tissue strains', *Journal of Orthopaedic Research*, 19(2), pp. 187–194. Available at: https://doi.org/10.1016/S0736-0266(00)90006-8.

Simmons, C.A., Meguid, S.A. and Pilliar, R.M. (2001b) 'Mechanical regulation of localized and appositional bone formation around bone-interfacing implants', *Journal of Biomedical Materials Research*, 55(1), pp. 63–71. Available at: https://doi.org/10.1002/1097-4636(200104)55:1<63::AID-JBM90>3.0.CO;2-V.

Simpson, D.J., Kendrick, B.J.L., Kaptein, B.L., Price, A.J., Murray, D.W. and Gill, H.S. (2010) 'Development of a Model-Based Roentgen Stereophotogrammetric Analysis System to Measure Polyethylene Wear in Unicompartmental Arthroplasty', *Proceedings of the Institution of Mechanical Engineers, Part H: Journal of Engineering in Medicine*, 224(11), pp. 1235–1243. Available at: https://doi.org/10.1243/09544119JEIM812.

Smith, L.J., Schirer, J.P. and Fazzalari, N.L. (2010) 'The role of mineral content in determining the micromechanical properties of discrete trabecular bone remodeling packets', *Journal of Biomechanics*, 43(16), pp. 3144–3149. Available at: https://doi.org/10.1016/j.jbiomech.2010.07.038.

Snell, R.S. (2004) *Clinical Anatomy*. 7th edn. Baltimore, Maryland, USA: Lippincott Williams & Wilkins.

Stoddart, J.C., Dandridge, O., Garner, A., Cobb, J. and van Arkel, R.J. (2021) 'The compartmental distribution of knee osteoarthritis - a systematic review and meta-analysis', *Osteoarthritis Cartilage*, 29(4), pp. 445–455. Available at: https://doi.org/10.1016/j.joca.2020.10.011.

Sun, Y., Li, Z., Zhao, K., Dimitriou, D., Yang, B., Cao, Z., Ma, X., Cheng, R., Li, P. and Tsai, T.-Y. (2024) 'Optimal intersurface stability for unicompartmental femoral component design with two pegs placed on the distal resection surface: 5 mm peg length increment and 10° peg inclination', *Knee Surgery, Sports Traumatology, Arthroscopy*, 32(8), pp. 2087–2096. Available at: https://doi.org/10.1002/ksa.12207.

Surendran, S., Kwak, D.S., Lee, U.Y., Park, S.E., Gopinathan, P., Han, S.H. and Han, C.W. (2007) 'Anthropometry of the medial tibial condyle to design the tibial component for unicondylar knee arthroplasty for the Korean population', *Knee Surgery, Sports Traumatology, Arthroscopy*, 15(4), pp. 436–442. Available at: https://doi.org/10.1007/s00167-006-0188-5.

Szivek, J.A., Thomas, M. and Benjamin, J.B. (1993) 'Technical note. Characterization of a synthetic foam as a model for human cancellous bone', *Journal of Applied Biomaterials*, 4(3), pp. 269–272. Available at: https://doi.org/10.1002/jab.770040309.

Szivek, J.A., Thompson, J.D. and Benjamin, J.B. (1995) 'Characterization of three formulations of a synthetic foam as models for a range of human cancellous bone types', *J Appl Biomater*, 6(2), pp. 125–8. Available at: https://doi.org/10.1002/jab.770060207.

Thatcher, J.C., Zhou, X.M. and Walker, P.S. (1987) 'Inherent laxity in total knee prostheses', *J Arthroplasty*, 2(3), pp. 199–207. Available at: https://doi.org/10.1016/s0883-5403(87)80038-4.

Thompson, D.W. (1961) *On growth and form*. Cambridge, UK: Cambridge University Press.

Thompson, M.S., McCarthy, I.D., Lidgren, L. and Ryd, L. (2003) 'Compressive and shear properties of commercially available polyurethane foams', *J Biomech Eng*, 125(5), pp. 732–4. Available at: https://doi.org/10.1115/1.1614820.

Toal. V., R. (2013) *THE MECHANICS OF MICRODAMAGE AND MICROFRACTURE IN TRABECULAR BONE*. Ph.D. Queensland University of Technology.

Townsend, P.R., Raux, P., Rose, R.M., Miegel, R.E. and Radin, E.L. (1975) 'The distribution and anisotropy of the stiffness of cancellous bone in the human patella', *Journal of Biomechanics*, 8(6), pp. 363–367. Available at: https://doi.org/10.1016/0021-9290(75)90071-8.

Townsend, P.R., Rose, R.M. and Radin, E.L. (1975) 'Buckling studies of single human trabeculae', *Journal of Biomechanics*, 8(3), pp. 199–201. Available at: https://doi.org/10.1016/0021-9290(75)90025-1.

Trisi, P., Berardini, M., Falco, A. and Vulpiani, M.P. (2015) 'Effect of Implant Thread Geometry on Secondary Stability, Bone Density, and Bone-to-Implant Contact: A Biomechanical and Histological Analysis', *Implant Dentistry*, 24(4). Available at: https://doi.org/10.1097/ID.0000000000000269.

Trisi, P., Perfetti, G., Baldoni, E., Berardi, D., Colagiovanni, M. and Scogna, G. (2009) 'Implant micromotion is related to peak insertion torque and bone density', *Clinical Oral Implants Research*, 20(5), pp. 467–471. Available at: https://doi.org/10.1111/j.1600-0501.2008.01679.x.

UK, A.R. and London, I.C. (2014) 'The musculoskeletal calculator'.

Vandamme, K., Naert, I., Geris, L., Sloten, J.V., Puers, R. and Duyck, J. (2007) 'Histodynamics of bone tissue formation around immediately loaded cylindrical implants in the rabbit', *Clinical Oral Implants Research*, 18(4), pp. 471–480. Available at: https://doi.org/10.1111/j.1600-0501.2007.01339.x.

Walker, P.S. and Sathasivam, S. (2000) 'Design forms of total knee replacement', *Proceedings of the Institution of Mechanical Engineers, Part H: Journal of Engineering in Medicine*, 214(1), pp. 101–119. Available at: https://doi.org/10.1243/0954411001535282.

Wazen, R.M., Currey, J.A., Guo, H., Brunski, J.B., Helms, J.A. and Nanci, A. (2013) 'Micromotion-induced strain fields influence early stages of repair at bone–implant interfaces', *Acta Biomaterialia*, 9(5), pp. 6663–6674. Available at: https://doi.org/10.1016/j.actbio.2013.01.014.

Weir, D.J., Moran, C.G. and Pinder, I.M. (1996) 'KINEMATIC CONDYLAR TOTAL KNEE ARTHROPLASTY: 14-YEAR SURVIVORSHIP ANALYSIS OF 208 CONSECUTIVE CASES', *The Journal of Bone & Joint Surgery British Volume*, 78-B(6), pp. 907–911. Available at: https://doi.org/10.1302/0301-620x.78b6.0780907.

Werner, B., Ovesy, M. and Zysset, P.K. (2019) 'An explicit micro-FE approach to investigate the post-yield behaviour of trabecular bone under large deformations', *Int J Numer Method Biomed Eng*, 35(5), p. e3188. Available at: https://doi.org/10.1002/cnm.3188.

Werner, F., Foster, D. and Murray, D.G. (1978) 'The influence of design on the transmission of torque across knee prostheses', *J Bone Joint Surg Am*, 60(3), pp. 342–8.

Williams, J.L. and Lewis, J.L. (1982) 'Properties and an Anisotropic Model of Cancellous Bone From the Proximal Tibial Epiphysis', *Journal of Biomechanical Engineering*, 104(1), pp. 50–56. Available at: https://doi.org/10.1115/1.3138303.

Winter, W., Klein, D. and Karl, M. (2013) 'Micromotion of Dental Implants: Basic Mechanical Considerations', *Journal of Medical Engineering*, 2013, pp. 1–9. Available at: https://doi.org/10.1155/2013/265412.

WOLFF, J. (1869) 'Uber die Bedeutung der Architektur der spongiosen Substanz', *Zentralblatt fur die medizinische Wissenschaft*, 0, pp. 223–234.

Wu, D., Isaksson, P., Ferguson, S.J. and Persson, C. (2018) 'Young's modulus of trabecular bone at the tissue level: A review', *Acta Biomaterialia*, 78, pp. 1–12. Available at: https://doi.org/10.1016/j.actbio.2018.08.001.

Yarahmadi, N., Vega, A. and Jakubowicz, I. (2017) 'Accelerated ageing and degradation characteristics of rigid polyurethane foam', *Polymer Degradation and Stability*, 138, pp. 192–200. Available at: https://doi.org/10.1016/j.polymdegradstab.2017.03.012.

Yoshikawa, R., Hiranaka, T., Okamoto, K., Fujishiro, T., Hida, Y., Kamenaga, T. and Sakai, Y. (2020) 'The Medial Eminence Line for Predicting Tibial Fracture Risk after Unicompartmental Knee Arthroplasty', *Clinics in Orthopedic Surgery*, 12(2), p. 166. Available at: https://doi.org/10.4055/cios19011.

Yudong W., Lihe W., Mingshuai S.U.N., Yiming L.I. and Ruiyong G. a. O. (2022) 'Research progress in risk factors and preventive and treatment measures of periprostheticfracture after unicompartment knee arthroplasty', *Journal of Clinical Medicine in Practice*, 26(14), pp. 144–148. Available at: https://doi.org/10.7619/jcmp.20220210.

Zavatsky, A.B., Oppold, P.T. and Price, A.J. (2004) 'Simultaneous In Vitro Measurement of Patellofemoral Kinematics and Forces', *Journal of Biomechanical Engineering*, 126(3), pp. 351–356. Available at: https://doi.org/10.1115/1.1762896.

Zimmer Biomet (2025a) *Oxford® Cementless Partial Knee | Zimmer Biomet*. Available at: https://www.zimmerbiomet.com/en/products-and-solutions/specialties/knee/oxford-cementless.html (Accessed: 18 August 2025).

Zimmer Biomet (2025b) *Oxford® Partial Knee | Zimmer Biomet*. Available at: https://www.zimmerbiomet.com/en/products-and-solutions/specialties/knee/oxford-partial-knee.html (Accessed: 17 August 2025).

Zimmer Biomet (2025c) *Persona The Personalized Knee | Zimmer Biomet*. Available at: https://www.zimmerbiomet.eu/en/products/persona-the-personalised-knee (Accessed: 27 August 2025).

Zivkovic, I. (2006) *The initial stability of the press-fit acetabular implant: Experimental and finite element study*. PhD. University of Illinois. Available at: https://indigo.uic.edu/articles/thesis/The_initial_stability_of_the_press-fit_acetabular_implant_Experimental_and_finite_element_study_/10853264.

涂意, 马童, 蔡珉巍, 薛华明 and 晓东 (2012) '微膝髁置治合并骨疏松的内间室骨炎', 中国骨疏松志, 6. Available at: https://doi.org/10.3969/j.issn.1006-7108.2012.06.010.

Appendix 1 Concept selection matrix

Six conceptual designs were produced and considered. Selection criteria were: cost, ease of design and manufacture; number of test components; speed; accuracy of motion; maximum load; and robustness. A binary dominance matrix was produced, and evaluation of the desired features was performed in using the conventional 1, 3, and 9 enumerators to enhance the separation of similar scoring concepts. Further, a weighting factor was assigned to each factor. Although in this selection the weighting was equal across all parameters, this weighting would allow greater emphasis to be put on different elements of the design, and so was left in.

Table 1.1: Concept selection matrix

Criteria	Weighting	Steppers (Open Loop)	Steppers (Closed Loop)	Rotating CAMs*	Servo Motor	Pneumatic/ Hydraulic
Cost (Larger rating lower cost)	1	9	3	3	1	1
Ease of design/ manufacture	1	9	3	1	1	1
Number of test components	1	9	9	1	9	9
Speed	1	1	3	3	3	3
Accuracy of Motion	1	1	3	3	3	3
Maximum Load	1	1	3	9	9	9
Robustness	1	1	3	9	3	3

*A fundamentally different physical design concept, based on crankshafts with multiple components, loaded by physical compression onto stiff springs, and glide/roll created by kinematic linkages, all driven by a single large motor transferring it's power by belts.

Table 1.2: Concept selection summary

Summary	Steppers (Open Loop)	Steppers (Closed Loop)	Rotating CAMs	Servo Motor	Pneumatic/ Hydraulic
Score (Bigger is better)	31	27	29	29	29

The winning concept was chosen due to the lowest cost and ease/speed of design and manufacture, with a view to upgrading the system if initial validation was successful.

Appendix 2 → Program code repositories

1. Program code to generate and run the ABAQUS model
    1. https://github.com/davidmcintoshheath/PegFoamInsertionABAQUSSimulation
2. Peg push-in pull-out force processing program
    1. https://github.com/davidmcintoshheath/PushInPullOutExperimentalDataProcessing
3. PU Foam compressive characterisation processing
    1. https://github.com/davidmcintoshheath/FoamMaterialCompressiveDataProcessing
4. Foam C1 coefficient calculation programme
    1. https://github.com/davidmcintoshheath/FoamModulusRatioToDensityRatio
5. Foam C4 coefficient calculation programme
    1. https://github.com/davidmcintoshheath/FoamElasticYieldRatioToDensityRatio
6. Foam C5 coefficient calculation programme
    1. https://github.com/davidmcintoshheath/FoamPlasticYieldRatioToDensityRatio
7. Knee machine error processing programming
    1. https://github.com/davidmcintoshheath/KneeMachineMotionDataProcessingProgram